# Influence of Porosity on the Flame Speed in Gasless Bimetallic Reactive Systems

by

Hesam Akbarnejad

Thesis submitted to the
Faculty of Graduate and Postdoctoral Studies
In partial fulfillment of the requirements
For the M.A.Sc. degree in
Mechanical Engineering

The Ottawa-Carleton Institute for Mechanical and Aerospace Engineering
Faculty of Engineering
University of Ottawa

# Abstract

Self-propagating High-temperature Synthesis (SHS) is the synthesis of solid materials by a reaction wave propagating into the initial reactants, typically two metals, which can alloy exothermically. Typically, experiments are performed with the reactants in powder form, with relatively low density. Recent experiments by Bacciochini *et al.* revealed much larger flame speeds in densified powders near TMD (theoritical maximum density), obtained by the cold spray process. The present thesis investigates why the flame speed increases dramatically with an increase in density of the powders. The investigation rests on the analytical model formulated by Makino by controlling how the variables are affected by changes in density.

Flame speed measurements were performed in mixtures of nickel (Ni) and aluminum (Al) at different initial densities. The density was varied by controlling the cold-pressing of the samples inside metallic channels and tubes. Experiments were also performed in ball-milled powders, in order to permit comparison with the experiments performed by Bacciochini in these mixtures at nearly maximum densities. The measurements revealed that the flame speed increases with the initial density, with a discontinuous transition occurring at approximately 60% theoretical maximum density (TMD). This transition also corresponds to the point where the powders deform plastically during the compaction process, suggesting that the intimate contact between the particles is responsible for the flame speed increase.

The flame speed dependence on powder density is attributed to the changes in the heat conductivity of the pressed powders. At high densities, where the powders have plastically deformed, the continuous structure yields conductivities close to the idealized solid matrix. At these high densities, the conductivity was modeled using the Effective Medium Theory (EMT). Analytical predictions of the flame speed, using available thermo-chemical data for the Al-Ni system were found in good agreement with the present experiments at high densities.

At low densities, since Al-Ni is a mixture of loose powders, the EMT model is no longer applicable. Thus, the thermal conductivity was experimentally measured and then was fitted using the semi-empirical model suggested by Aivazov. Using this data, Makino's model predicts the correct flame speed dependence observed experimentally.

The present thesis has thus established that the dependence of flame speed on density is due mainly to the changes in the structure and thermal conductivity of the powders.

# Acknowledgements

I would like to thank my supervisor, Dr. Matei Radulescu for all his guidance and support during the past two and half years. Also, I would like to thank Defence RD Canada, with Dr. Julian Lee as the technical monitor, for the financial support and Canadian Space Agency for partial funding.

Many others have made invaluable contributions to this work. Many thanks are due to my dear friend, Andrew Stewart, for making a very enjoyable time during our studies together and Nick Sirmas for his help with editing the final manuscript. I would also like to thank Dr. Bacciochini for his help in the lab and Dr. Robitaille for lending me some of his equipment.

Of course, none of this would have been possible without the lifetime, unflagging, and unwavering support of my family. To them I extend the deepest thanks of all.

# Contents

# List of Figures

# List of Tables

# Nomenclature

## Roman Letters

| Symbol | Definition | Units |
|---|---|---|
| $A$ | Reduced surface Damkohler number | |
| $A_{powders}$ | Cross-sectional area of the powders in thermal conductivity measurement | $m^2$ |
| $A_{rod}$ | Cross-sectional area of the lower rod in thermal conductivity measurement | $m^2$ |
| $A_{wall}$ | Cross-sectional area of the wall in thermal conductivity measurement | $m^2$ |
| $B$ | Dummy variable | |
| $C$ | Circumference of the cross-sectional view | m |
| c | Specific heat | J/(kg.K) |
| $D$ | Mass diffusivity | $m^2/2$ |
| $Da$ | Surface Damkohler number | |
| $e$ | Error in flame speed measurement | |
| $E$ | Young's modulus | $kg/(m.s^2)$ |
| $F$ | Force vector per unit mass | N/kg |
| $f$ | Distribution function | |
| $f_{st}$ | Stoichiometric mass ratio | |
| $G$ | Number of particles per unit volume per unit range of radius and time | m/s |
| $H$ | Heat Losses | J |
| $h_f$ | Total enthalpy per unit mass of the fluid | $m^2/s^2$ |
| $h_{in}$ | Enthalpy per unit mass of material flowing from the vicinity of a particle to the fluid | $m^2/s^2$ |
| $h_N$ | Total enthalpy per unit mass of non-metal particles | $m^2/s^2$ |
| $h_N^0$ | Total enthalpy per unit mass of non-metal particles at $T^0$ | $m^2/s^2$ |

## Roman Letters(continued)

| Symbol | Definition | Units |
|---|---|---|
| $h_{powders}$ | Height of the powders in thermal conductivity measurement | m |
| $h_{rod}$ | Height of the lower rod in thermal conductivity measurement | m |
| $h_{wall}$ | Height of the wall in thermal conductivity measurement | m |
| $K$ | Thermal conductivity | W/(m.K) |
| $K_a$ | Thermal conductivity of air | W/(m.K) |
| $K_{Gavg}$ | Geometrical average thermal conductivity | W/(m.K) |
| $K_e$ | Effective thermal conductivity | W/(m.K) |
| $K_m$ | Thermal conductivity of the medium | W/(m.K) |
| $K_p$ | Thermal conductivity of a sphere | W/(m.K) |
| $k_{powders}$ | Thermal conductivity of the powders in thermal conductivity measurement | W/(m.K) |
| $k_{rod}$ | Thermal conductivity of the lower rod in thermal conductivity measurement | W/(m.K) |
| $K_s = K_0$ | Thermal conductivity of solid particles | W/(m.K) |
| $K_{TMD}$ | Thermal conductivity at theoretical maximum density | W/(m.K) |
| $k_{wall}$ | Thermal conductivity of the wall in thermal conductivity measurement | W/(m.K) |
| $L_{flame}$ | A range that the flame can exist | m |
| $l$ | Mean free path of a phonon | m |
| $n$ | Number of N particles | |
| $O$ | Dummy variable | |
| $P$ | Total pressure tensor | kg/(m.s$^2$) |
| $P_{atm}$ | Atmospheric pressure | kg/(m.s$^2$) |
| $p$ | Hydrostatic pressure | kg/(m.s$^2$) |
| $q$ | Heat flux vector | kg/(m$^3$) |
| $q^0$ | Heat of combustion per unit mass of N species | W/kg |
| $R$ | Radius of nickel particles | m/s |

## Roman Letters(continued)

| Symbol | Definition | Units |
|---|---|---|
| $\dot{R}$ | Rate of change of particle size | m/s |
| $R_{powders}$ | Thermal resistance of powders in the thermal conductivity measurement | K/W |
| $R_{rod}$ | Thermal resistance of the lower rod in the thermal conductivity measurement | K/W |
| $R_{wall}$ | Thermal resistance of the wall in the thermal conductivity measurement | K/W |
| $r_{in}$ | Inner radius of the tube | m |
| S | Cross-sectional area of compacted specimen | |
| $\mathbf{T}$ | Viscous stress tensor | kg/(m.s$^2$) |
| $T$ | Temperature | K |
| $T^0$ | Initial temperature | K |
| $T_a$ | Activation temperature for the reaction | K |
| $T_d$ | Activation temperature for the condensed phase mass diffusivity | K |
| $T_m$ | Melting temperature | K |
| t | Time | s |
| $U_M$ | Diffusion velocity | m/s |
| $u = u_0$ | Flame speed | m/s |
| $u_{0,empirical}$ | Flame speed using empirical thermal conductivity | m/s |
| $u_{0,EMT}$ | Flame speed using effective medium theory thermal conductivity | m/s |
| $u_{0,GAvg}$ | Flame speed using geometric average thermal conductivity | m/s |
| $\bar{v}$ | Average element velocity | m/s |
| $v$ | Volume fraction | |
| $v_M$ | Stoichiometric coefficient of metal particles | |
| $v_N$ | Stoichiometric coefficient of non-metal particles | |
| $v_P$ | Stoichiometric coefficient of products | |
| $V$ | Velocity of a particle | m/s |
| $W$ | Atomic mass | g/mol |
| $X$ | Distance along the tube | m |
| $\dot{x}$ | Average phonon velocity | m/s |
| $Y$ | Mass fraction | |
| $Z$ | Mass ratio of fluid | |

## Greek Letters

| Symbol | Definition | Units |
|---|---|---|
| $\alpha$ | Normalized temperature rise | |
| $\beta$ | Spalding transfer number | |
| $\Delta T_{powders}$ | Temperature difference along the powders in thermal conductivity measurement | K |
| $\Delta T_{rod}$ | Temperature difference along the the lower rod in thermal conductivity measurement | K |
| $\gamma$ | Mass ratio of fluid to solid | |
| $\zeta$ | Normalized mass fraction | |
| $\eta$ | The variable which represents a change of particle size | |
| $\theta$ | Normalized temperature | |
| $\kappa$ | Degree of dilution defined as the initial mass fraction of the diluent | |
| $\Lambda_0$ | Mass burning rate eigenvalue | |
| $\mu$ | Mixture ratio defined as the initial molar ratio of N to M divided by stoichiometric molar ratio | |
| $\xi$ | Normalized mass ratio of fluid | |
| $\rho$ | Density | $kg/m^3$ |
| $\rho_{Al} = \rho_M$ | Density of aluminum (metal) | $kg/m^3$ |
| $\rho_{Ni} = \rho_N$ | Density of nickel (non-metal) | $kg/m^3$ |
| $\rho_f$ | Density of fluid | $kg/m^3$ |
| $\rho_s$ | Density of solid | $kg/m^3$ |
| $\rho_{rel}$ | Relative density | $kg/m^3$ |
| $\rho_{TMD}$ | Theoretical maximum density | $kg/m^3$ |
| $\rho_{tot}$ | Total density | $kg/m^3$ |
| $\chi$ | Surface regression rate | $kg/(m.s^2)$ |
| $\phi$ | Porosity | |
| $\tau_{xx}$ | The xx component of the viscous stress tensor T | $kg/(m.s^2)$ |
| $\omega$ | Mass rate of production per unit volume | $kg/(m.s^3)$ |

# Chapter 1

# Introduction

## 1.1 Background

Self-propagating high-temperature synthesis (SHS) is the synthesis of solid products by a combustion wave. The combustion wave is sustained by the exothermic reactions between two or more reactants. They are typically thermites involving the oxidation of a metal by another metal oxide (e.g., Al and $Fe_2O_3$ yielding $Al_2O_3$ and Fe) or intermetallics (e.g., Al and Ni yielding Al-Ni). The reaction between the two reactants takes place in a self-sustaining regime leading to the formation of solid products. The reaction wave proceeds by heat transfer from the products towards the non-reacted mixture. Since the reactions are highly exothermic, the increase in temperature in the non-reacted mixture initiates the reaction. A self-sustained reaction is thus established, which sweeps through the entire material. Figure 1.1 illustrates the propagation of such a self-sustained reaction wave in a titanium-carbon mixture. The luminous part corresponds to the hot products of the reaction.

Original research on the SHS process was initially developed during the 1960s. In 1967, Merzhanov, Skhiro, and Borovinskaya [1] explained the self-sustaining character of reactions in a condensed phase and the principle of a "solid flame". This publication is considered as the first comprehensive paper regarding the SHS process. The first International Journal of Self-Propagating High-Temperature Synthesis was published in the early 1990s [2], approximatively 25 years after the initial discovery of the phenomenon. Since then, more than five hundred SHS products have been produced, including carbides, borides, nitrides, silicides, oxides, hydrides, intermetallics, chalcogenides, and also composite materials from non-metallic ceramics, and hard alloys [3]. In addition, during the past two decades, new advanced materials have been developed, such as composite pow-

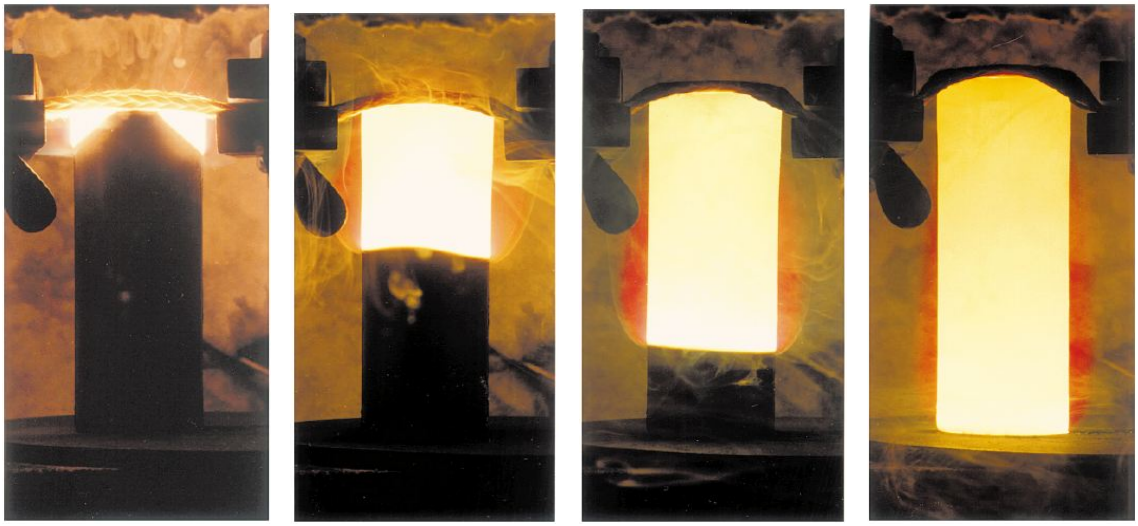

**(a)** $t = 0s$ **(b)** $t = 1s$ **(c)** $t = 2s$ **(d)** $t = 3s$

**Figure 1.1:** SHS process for Ti-C at different times [5]

ders, foam ceramics, ceramics containing no activators for sintering, anisotropic ceramics, oxygen-free single crystals, organic materials, and macroinhomogenous structures (materials with an intentionally organized inhomogeneous structure such as coated materials, composites, multi-layered and functionally-gradient materials, etc.) [4]. Some examples of these materials are shown in Figure 1.2. SHS products may appear in the form of gas or solids (powders, foams, cakes, films, whiskers, fibers, crystals, etc). The macro-structure of the products can be uniform or nonuniform, depending on different parameters such as the type and shape of materials. Also, in some cases, the product macro-structure is intentionally made nonuniform (e.g. multilayer and functionally graded materials).

## 1.2 Problem Identification

The SHS process typically involves porous reactants and products. This is primarily due to the requirement of premixing the reactants in powder form at sufficiently small scale, typically micron to nanometer scale, then cold-pressing the compacts. The relative density of the SHS powders is usually much lower than the theoretical maximum density (TMD). The relative density of the powders used typically varies weakly, typically between 40% to 60% [7, 8].

However, in 2011, Bacciochini *et al.* [9] were able to create an Al-Ni mixture at nearly 100% density ratio using the "Cold Gas Dynamic Spray Process". In the cold spraying

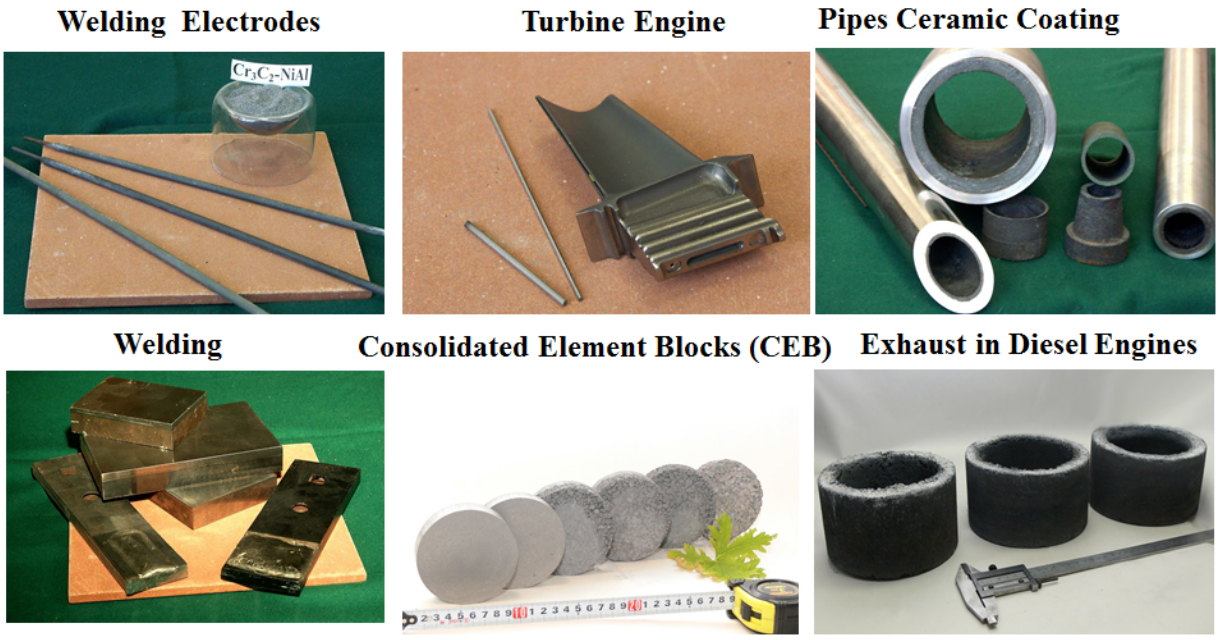


**Figure 1.2:** Example of SHS products [6]

technique, particles are accelerated to high speeds with a relatively low temperature supersonic gas. The powders are merged together via plastic deformation upon impact on a target, resulting in mixtures with porosity levels close to zero. This technique permits one to retain the powder micro-structure and prevents any reactions during the consolidation phase. Further details of the cold spray technique are explained in their publication [9].

The combustion behavior of SHS processes in the reactive composites obtained with the cold spray technique was reported to be very different compared to low density ratio mixtures. Specifically, as shown in Figure 1.3, the flame speeds at close to the theoretical maximum density (shown by black circles) were found higher by approximately an order of magnitude, as compared to the values measured at lower densities (shown by hollow squares), which agreed with previous measurements performed by Naiborodenko *et al.* [8] at high porosity.

This anomalous behavior has also been observed in a study by Mukasyan *et al.* [7]. In their study, Mukasyan considered a system of nickel-clad aluminum particles, compacted at different densities. Their measurements of flame speed are shown in Figure 1.4. These results indicate that the flame speed increases with density. They have also observed a discontinuity in flame speeds at approximatively 68%, where the flame speed suddenly increases several fold. Mukasyan *et al.* argued that the discontinuity is caused by the change in the heat transfer mechanism. At high porosity, they changed the gases in the

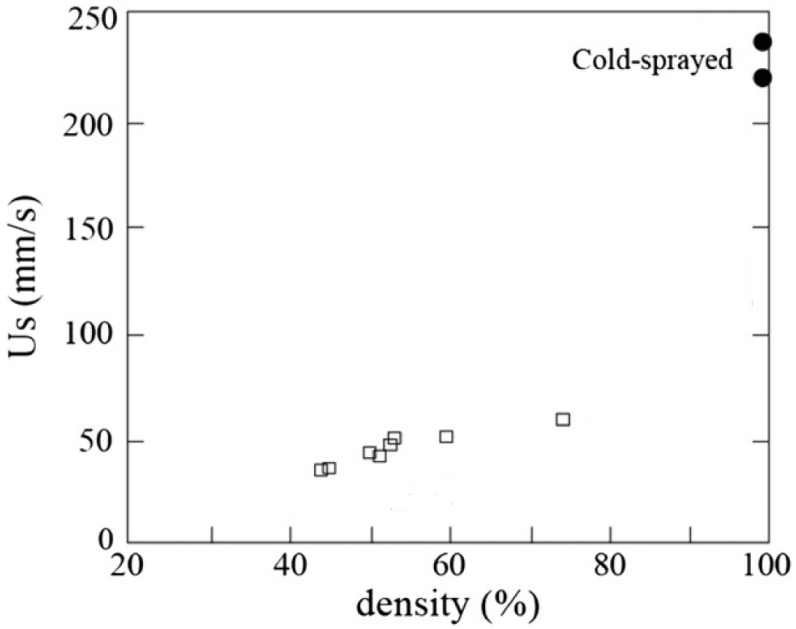


**Figure 1.3:** Flame speed of aluminum-nickel mixture as a function of the density ratio [9]

pores and correlated the flame speed with the heat conductivity of the gas. At low porosity, the interstitial gas was found to have a negligible influence on the results, from which they concluded that the solid phase heat conductivity controlled the flame propagation rate. They argued that the plastic deformation of powders rapidly increases the contact area between the particles, resulting in higher heat conduction in the solid matrix and hence a higher flame speed. Their explanations, however, remained qualitative, as they were not substantiated by measurements of the heat conduction change in their samples nor theoretical models linking the flame speed to the change in conductivity and process parameters.

In the present study, we address the effect played by the powder porosity on the SHS flame speed. We also wish to develop a predictive first principles model for the flame speed than can account for the observed strong variations with density illustrated in Figures 1.3 and 1.4. With the new data now available for high density ratio mixtures [9], model validation can be made much more accurately.

## 1.3 Theoretical Models

In the past, different approaches have been considered in order to model the flame propagation in gasless SHS reactions. We first review the available formalisms in order to

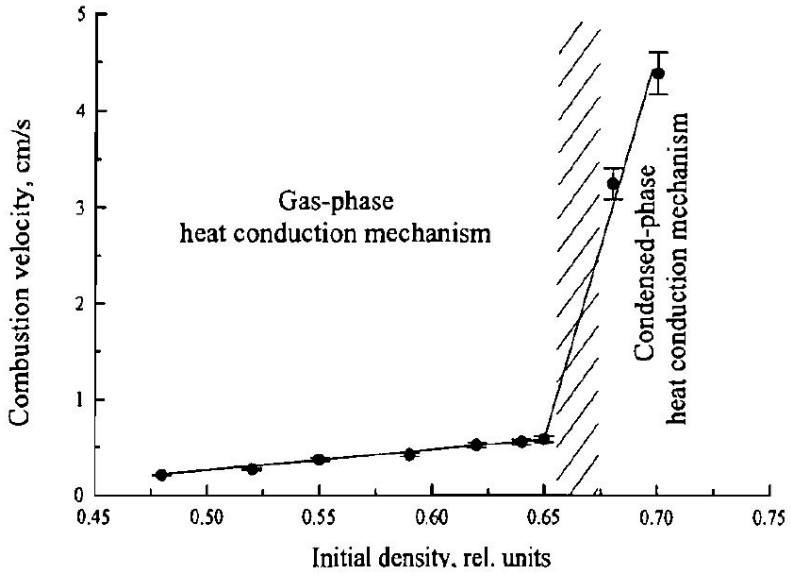


**Figure 1.4:** Mukasyan's results for SHS flames speed as a function of initial sample relative density [7]

identify the one in which the effect of porosity can be addressed.

### Homogeneous models

The conventional approach to model the SHS flame phenomenon was based on the homogeneous assumption, using the laminar flame theory of pre-mixed gaseous systems [1, 10]. For example, Merzhanov suggested in 1972 one of the earliest models based on the homogeneous system, where the combustion is only studied at large scales [1, 11]. In such an approach, the micro-structure effects are neglected in the combustion analysis and thermo-kinetic parameters are selected *ad hoc*. It was originally suggested that heat conduction occurs more rapidly than mass diffusion in SHS processes [12] and as a result, mass transfer by diffusion at the small scales may be neglected. While the size, shape, and the structure of SHS mixtures have been shown to significantly influence the combustion behavior [7, 12, 13, 14], these effects are difficult to account for in homogeneous models. As a result, homogeneous models for SHS mixtures are considered as inaccurate techniques, which cannot account for the porosity effects we wish to investigate in the present thesis.

### Heterogeneous models

In a different approach, some heterogeneous models were suggested for modeling the SHS flame. Contrary to the homogeneous models, heterogeneous models address the microstructure of the non-premixed reactants. One of the early heterogeneous models was suggested by Hardt and Phung in 1973 [14]. Their model provided an estimate for the flame speed for SHS processes by accounting for the heterogeneous effects in a one-dimensional representation. Hardt and Phung represented the complicated structure of pressed powders, as shown in Figure 1.5a, by a one-dimensional sequence of layers, as shown in Figure 1.5b. The alternating layers consisted of each of the reactants. Reactions took place at these interfaces, which formed the model's unit cells. While their results were able to account for the reaction rate dependence on the diffusive-kinetic effects occurring at the constituents interfaces, the one-dimensional simplifying assumption could not easily account for the shape, size, and thermal conductivity of powders in a meaningful way.

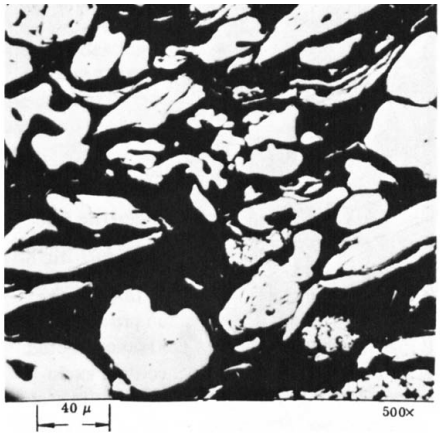


**(a)** Photograph of pressed binary powder mixture in Hardt's model

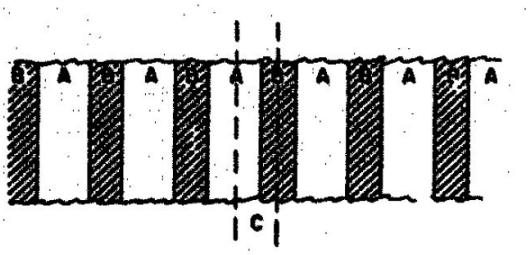


**(b)** Cell Geometry (A and B are the 2 metals and C is the diffusion cell)

**Figure 1.5:** Hardt's microstructure of powders and schematic of the model [14]

In a very different approach, Varma *et. al* [12] developed in 2001 a micro-heterogeneous cell model to describe the local reaction wave propagation in a heterogeneous porous medium. Varma *et al.* suggested that in heterogeneous media, often the characteristic length of heat conduction may be close to the scale of the particle size itself. In such cases, the reaction mixture with irregularly shaped particles must also be considered to model the combustion behavior. Taking this fact into account, Varma *et al.* used a micro-heterogeneous cell model developed by Hwang *et al.* [15] to simulate the combustion propagation in heterogeneous media. In this model, the reactive powder compact medium

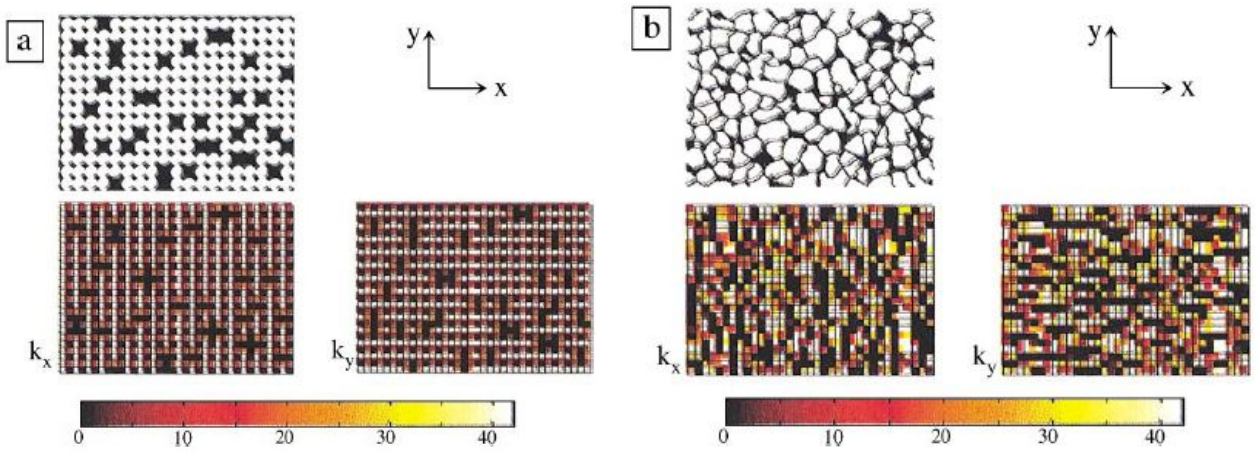


**(a)** Random model structure **(b)** Cross-section of the actual sample

**Figure 1.6:** Varma's map of thermal conductivity of combustion wave [12]

is represented by a discrete matrix of reaction cells, as shown in Figure 1.6. The cells have varying physical and transport properties due to the random organization of the solid and gas phases in the reactive medium. Therefore, instead of analyzing the reaction at macro-scales by coarse-grained averages, a computer model was used to analyze individual cells and predict the emergent macro-scale behavior. Comparison of his model with different experimental results showed satisfactory agreement. The main conclusion of his model is that the nature of wave propagation in heterogeneous media depends on the nature of local heat transfer as well as the kinetics. The absence of analytical closure, however, does not permit one to identify physical mechanisms.

Other micro-scale continuum models have been suggested in order to model the heterogeneous reaction process. Such approaches, initially developed for propellants [16, 17], require the numerical integration of the reactive fluid dynamic problem with the appropriate constitutive behavior, thermal and reaction-diffusion processes occurring at the interfaces between the different phases. These computationally expensive models also require the input of the initial three-dimensional configuration. A random packing of solid spherical particles with different sizes and compositions was found to provide an adequate approximation of the real 3D microstructure of the heterogeneous propellants [16, 17]. Good agreement between the model and experimental data has been achieved by assuming a 3D randomly packed model of the propellant. Nevertheless, the application of this approach to combustion synthesis systems is limited by the lack of knowledge about the real microstructure, mechanisms of heat transfer and interaction between particles in such systems. Similar to Varma's model, such an approach also does not clearly identify

physical mechanisms.

**Makino's heterogeneous model derived from spray combustion**

An analytical macroscopic model for the SHS process was developed by Makino in order to account for the micro-scale processes in a realistic way [5]. According to Makino, the heterogeneous behavior of the SHS process is very similar to the fuel spray combustion flame. The model therefore uses the spray combustion method to model the SHS process.

The reaction zone structure of the flame analyzed by Makino is shown schematically in Figure 1.7, borrowing concepts from the premixed and non-premixed models. The reactants are assumed to have a heterogeneous structure. A characteristic particle size is ascribed to the component with the highest melting point. This component is assumed to remain in the solid phase during most of the flame propagation time scale. This component is analogous to the fuel droplet in a fuel spray, which is consumed by the surrounding oxidizer. The flame consists of three zones. First, the preheating zone corresponds to the region where the mixture is heated by the energy released in the reaction zone. The preheat zone ends when the mixture reaches the melting point of one of the materials, resulting in a mixture of molten metal and solid particles. With one component molten and sufficiently high temperatures, mass transfer can take place with a sensible rate at the perfectly wetted solid particle surfaces. The reactions are typically assumed to be controlled by this mass diffusion process. The evolution of the reaction zone is analogous to the collective behavior of fuel droplets being consumed in spray combustion via mass diffusion. Once the particles are totally consumed, the reaction is assumed complete and the mixture is cooled (crystallization zone) forming new materials.

Using the coarse-grained conservation equations for spray combustion coupled with the regression rate of individual particles, Makino was able to derive an expression for the flame speed in terms of the thermo-kinetic properties of the mixtures and size of powders. The detailed derivation of the model is outlined in Chapter 2. It is remarkable that a good agreement between analytical and experimental results was obtained for different variables (initial temperature, degree of dilution, particle sizes, etc.) and also using different powders, such as Ni-Ti, Al-Ni, Hf-B, Co-Ti, Tr-B. Such agreement is somewhat surprising in view of the experimental results obtained by Bacciochini *et al.* [9], showing the strong effect of density and porosity. The effect of porosity (internal voids) is not directly included in Makino's model. Indirectly, it can be included by specifying how the different processes are affected by porosity, such as the diffusion rates, heat conduction rates and overall densities. This is considered in the present thesis.

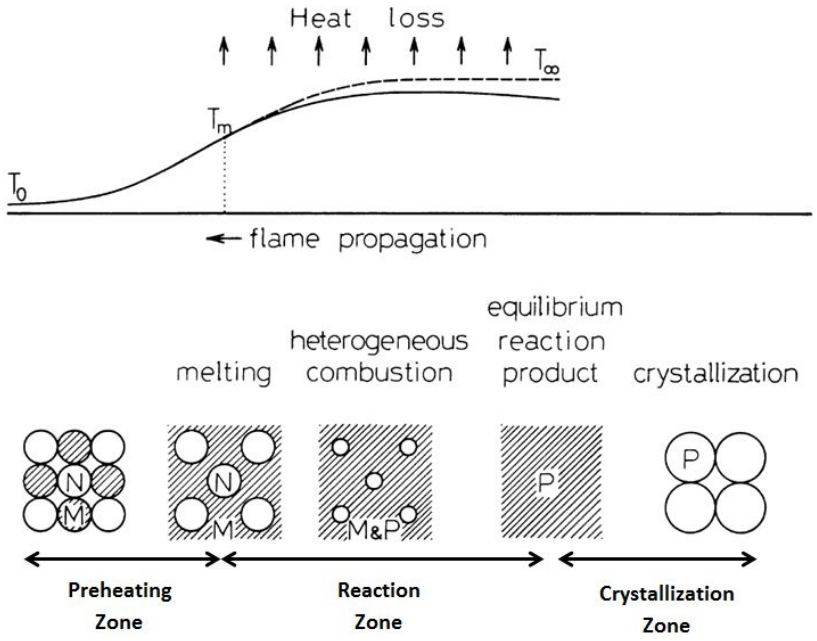


**Figure 1.7:** Schematic flame structure in the heterogeneous flame [5]

### 1.3.1 Thermal conductivity in powder compacts

All macroscopic models for the SHS flame propagation require the thermal conductivity of the powder mixture. The problem of heat conduction in powder compacts, however, poses severe difficulties. A variety of models have now been published to estimate the thermal conductivity of porous materials as a function of the porosity and structure of powders. Some examples of these models are presented in Figure 1.8. Chapter 3 provides a review of these models. Nevertheless, it is of interest to note here that given a certain porosity, the conductivity can vary by more than an order of magnitude depending on whether the powder compact has an internal porosity (e.g., voids as in swiss cheese) or external porosity (e.g., weakly aggregated solids with poor contact in a gaseous medium). While models for the heat conductivity can be incorporated in predictive models for flame propagation, care must be exercised to reflect the appropriate type of porosity in the powder compacts.

## 1.4 Thesis Overview

The present thesis investigates why the flame speed increases with an increase in density of the mixture, and attempts to provide a predictive model. It appears that Makino's model for flame propagation in heterogeneous gasless systems provides the most physical and transparent way to formulate such a model and comparing with experiments. The input

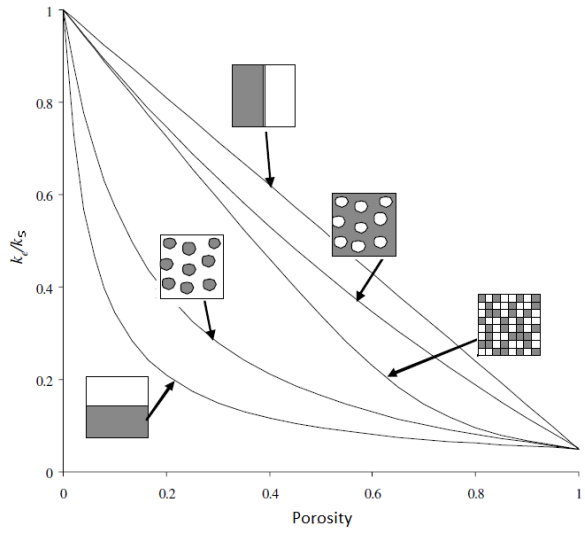


**Figure 1.8:** Thermal conductivity of porous materials as a function of porosity using different models [18]

to the model we investigate in the present study is the thermal conductivity dependence on porosity. We determine this dependence by reviewing analytical models and compare them with our experimental measurements. Makino's model is then tested with experiments of flame speed at different density ratios.

We focus on the gasless system of aluminum-nickel, studied previously by Bacciochini *et al.* [9] at vanishing porosities. Reliable thermal-kinetic data have also been suggested by Makino for this system. This permitted us to make a quantitative comparison with the flame speed data measured in the present experiments and those of Bacciochini *et al.* [9].

The thesis is organized as follows. Makino's model is outlined in Chapter 2. A derivation of the model is provided, in order to familiarize the reader with the notation and assumptions made in its derivation. Since the thermal conductivity is one of parameters in Makino's model, by relating the porosity to the thermal conductivity of the mixture, a relation between flame speed and powder porosity can be achieved. In Chapter 3, different analytical, numerical, and empirical models are discussed to predict the thermal conductivity of powder compacts relevant to the SHS phenomenon in terms of the density of the compact. Also, in the second section of Chapter 3, different procedures for experimentally measuring the thermal conductivity of solid mixtures are reviewed.

The results of the conductivity and flame speed predictions are compared with new experiments in Chapters 4 and 5. Chapter 4 provides the details of the experimental setups and procedures to measure the flame speed and the thermal conductivity in powder

compacts of different densities. Chapter 5 provides the comparison between the models for heat conductivity and flame speed with the present experiments. Lastly, Chapter 6 concludes the thesis with a summary of the state of the art and recommendations for future work.

# Chapter 2

# Makino's Model

As discussed in the Introduction, Makino formulated a closed-form analytical model for predicting the flame speed in SHS processes. According to Makino, the reaction zone structure of the SHS flame is very similar to the fuel spray combustion flame structure [19]. The model thus follows very closely the analytical approach used in spray combustion, as detailed for example, in "Combustion Theory" [19]. The spray combustion model is a hydrodynamic model, which averages over the contribution off all the particles. As such, it assumes the characteristic scales of the flame to be much larger than the particle size. Below we provide an outline of the model formulation and assumptions made. The treatment follows Williams' outline of the spray combustion method, as well as its adaptation to the SHS flame, taken from Makino's review paper [5].

## 2.1 Derivation of the Model

According to Makino, the SHS flame consists of different zones, as shown in Figure 2.1. The first region is the preheating zone where all the particles are in the original shape just before the arrival of the flame. Due to a low temperature and a small area of contact between particles, the reaction effects cannot be noticeable before the combustion wave reaches the particles. However, as the combustion wave approaches, the mixture is heated causing the lower melting point metal ($M$) to melt. As a result, a mixture of liquid (metal $M$) and solid particles (called non-metal $N$) is created. In addition, due to an increase of the contact area and the temperature, the reaction between solid particles (non-metal) and molten metal is greatly enhanced (reaction zone). Therefore, it can be assumed that at the reaction zone, the lower melting metals $M$ are all melted first, so the higher melting point metal particles $N$ float inside the molten metal $M$. At this point, the reaction between $M$

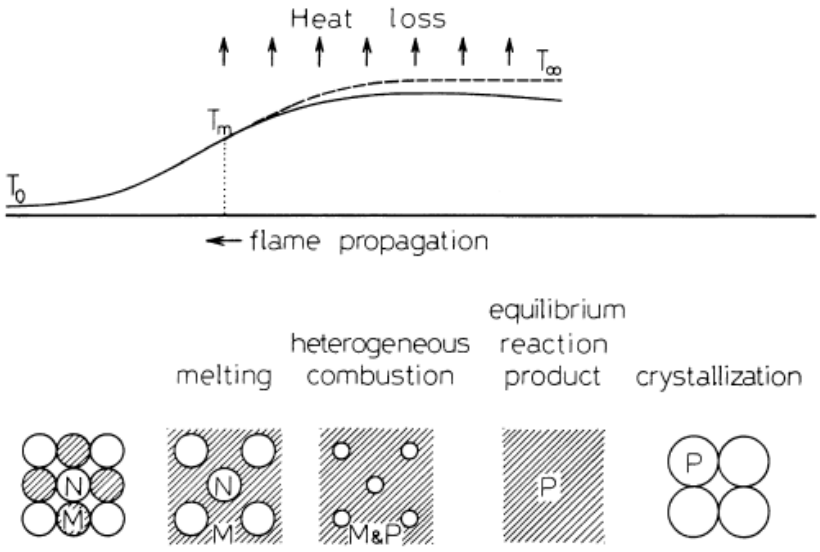


**Figure 2.1:** Schematic flame structure in the heterogeneous flame [5]

and $N$ takes place. After the reaction is completed, the mixture is cooled and crystallized (crystallization zone).

Using this assumption, it is possible to see how the SHS flame can be related to the fuel spray combustion. Matching this model with the fuel spray combustion, $M$ and $N$ particles represent oxygen and the fuel respectively. The general chemical model in this case can be simplified to:

$$v_M M + v_N N \longrightarrow v_P P \tag{2.1}$$

where $v$ is the stoichiometric coefficient of each component and $P$ represents the product.

The derivation of Makino's model follows three main steps. First, the general conservation equations are introduced following the flame frame of reference. Then, the reaction is analyzed between the metal and non-metal particles using the definitions of the surface regression rate. The conservation equations are then simplified using the surface reaction rate equations and some assumptions.

To solve the conservation equations in the spray combustion model, a statistical description is used given by the *distribution function*.

### 2.1.1 Distribution Function

The *distribution function* is the probable number of particles in the radius range $dR$ about $R$, located in the range $dx$ about $x$ with velocities in the range $dv$ about $v$ at time $t$:

$$f\left(R,x,v,t\right)dRdxdv \tag{2.2}$$

Here, $dx$ and $dv$ are the three-dimensional elements of physical space and velocity space respectively. The distribution function is used in the derivations and simplifications of the governing equations.

The equation governing the time rate of change of the distribution function $f$, called *the spray equation* in the spray combustion model, is given as:

$$\underbrace{\frac{\partial f}{\partial t}}_{1} = -\underbrace{\frac{\partial}{\partial R}(\dot{R}f)}_{2} - \underbrace{\nabla_x(vf)}_{3} - \underbrace{\nabla_v(Ff)}_{4} \tag{2.3}$$

- $\dot{R}$ : Rate of change of the particle size $R$
- F: Force per unit mass on this particle
- Term 2: Changes in $f$ resulting from the change of particle size
- $\nabla_x$ and $\nabla_v$: The gradient operators of space and velocity
- Term 3: Motion of the particles into and out of the spatial element $dx$ by virtue of their velocity $v$
- Term 4: Acceleration of the particles in the velocity element $dv$ caused by the force $F$.

The terms $\dot{R}$ and $v$ are then averaged:

$$\bar{\dot{R}} = \frac{1}{G}\int \dot{R}f dv \qquad \bar{v} = \frac{1}{G}\int vf dv \tag{2.4}$$

where the bar represents the average of any function and $G$ is the number of particles per unit volume per unit range of radius:

$$G = \int f dv \tag{2.5}$$

It must be noticed that the spatial and velocity elements are 3D vectors resulting from the gradient functions. The velocity dependence of the distribution function $f$ can be eliminated using the distribution function (2.3) by integrating over velocity space. Following Williams' textbook [19], since $f_i \to 0$ very rapidly as $v \to 0$, the divergence theorem shows that the integral of the last term in Equation (2.3) is zero, so we get:

$$\frac{\partial}{\partial R}(\bar{\dot{R}}G) + \nabla_x.(\bar{v}G) = 0 \tag{2.6}$$

$S(x)$ (the local cross-sectional area) is also assumed to be constant in thr $x$ direction, and therefore, Equation (2.6) can be rewritten in two dimensional format:

$$\frac{\partial}{\partial R}(\bar{\dot{R}}G) + \frac{1}{S}\frac{\partial}{\partial x}(S\bar{v}G) = 0 \tag{2.7}$$

### 2.1.2 Conservation Equations

Restricting the problem to a steady state, one-dimensional, constant-area flow in which all particles travel at the same velocity, the distribution function $f$ is expressed as:

$$f(R, x, v) = G(R, x)\delta(v - \bar{v}) \tag{2.8}$$

where $x$ is the flow direction, $v$ is the velocity of all particles, $\bar{v}$ is the average element velocity, and $\delta$ is the delta function.

Here, the general format of the conservation equations are first introduced and then simplified. Some non-dimensionalized variables, used for the derivations of the governing equations, are introduced here [20, 21]:

$$\tilde{r} = \frac{r}{R}, \quad \tilde{Y}_M = \frac{Y_M}{f_{st}}, \quad f_{st} = \frac{v_m W_M}{v_N W_N}, \quad \tilde{\rho} = \frac{\rho_M}{\rho_{M,e}}, \quad \tilde{D} = \frac{D}{D_e} \tag{2.9}$$

where $r$ is the radial coordinate, $\tilde{Y}_M$ the stoichiometrically weighted mass fraction, $f_{st}$ the stoichiometric mass ratio, $W$ the molecular weight, $D$ the mass diffusivity, and the subscripts $s$ and $e$ respectively represent the particle surface and the outer edge of the boundary layer.

#### Continuity

In subliming, particles add:

$$\int\int \rho_N 4\pi R^2 \dot{R} f dR dv \tag{2.10}$$

grams per unit volume per second to the gas. Consequently, the overall steady state continuity equation for fluid is [19]:

$$\nabla_x.(\rho_f u) = -\int\int \rho_N 4\pi R^2 \dot{R} f dR dv \tag{2.11}$$

where $u$ is heterogeneous burning velocity and $\rho_f$ is the fluid density defined as the mass of fluid per unit volume of physical space. $\rho_f$ is not necessary the same as liquid density $\rho_M$ and in fact, the fluid and liquid densities are related by the following expression:

$$\rho_f = \rho_M \left(1 - 4/3\pi R^3 f dR dv\right) \tag{2.12}$$

Simplifying Equation (2.11) into one dimensional steady state flow and integrating over $v$, we get:

$$\frac{d}{dx}(\rho_f u) = -\int_0^\infty \rho_N 4\pi R^2 \dot{R} G dR \tag{2.13}$$

Recalling the distribution function in Equation (2.3), it can be shown that:

$$\frac{d}{dx}(\rho_s \bar{v}) = -\int_0^\infty \rho_N 4\pi R^2 \dot{R} G dR \tag{2.14}$$

where $\rho_s$ is the mass of solid per unit spatial volume:

$$\rho_s = \rho_N \int_0^\infty (4/3)\pi R^3 G dR \tag{2.15}$$

Since the right hand sides of Equations (2.13) and (2.14) are identical, the overall continuity is simplified to:

$$\rho_f u + \rho_s \bar{v} = m = \text{constant} \tag{2.16}$$

$m$ is the total mass flow rate or mass burning rate per unit area.

In the Makino's model, the liquid medium and the solid particles are reasonably assumed to be in the mechanical equilibrium. In other words, all particles in the combustion wave are reasonably assumed to travel at the same velocity as the fluid:

$$\bar{v} = u \tag{2.17}$$

So the continuity equation can be further simplified to:

$$\rho_t u = m = \text{constant} \tag{2.18}$$

where $\rho_t \equiv \rho_f + \rho_S$ is the total density.

**Species conservation**

When chemical reactions occur at the particle surface and species M are consumed in the surface reaction according to $v_N M + v_N N \longrightarrow v_P P$ , the species conservation equation for component M is given as:

$$\frac{\partial f Y_M}{\partial t} + \nabla_x . [\rho_f (u + U_M) Y_M] = \omega + \left(\frac{v_M W_M}{v_N W_N}\right) \int_0^\infty \int_0^\infty \rho_N 4\pi R^2 \dot{R} f dR dv \tag{2.19}$$

where $U_M$, $Y_M$ and $\omega$ are the diffusion velocity, the mass fraction of species $M$ in the fluid (molten materials), and the mass rate of production of species $M$ by homogeneous

chemical reactions in the fluid respectively. Using the same procedure as for the continuity equation, the species conservation Equation (2.19) can be simplified to:

$$\frac{d}{dx}\left(\rho_f(u+U_M)Y_M\right) = \left(\frac{v_M W_M}{v_N W_N}\right)\frac{d}{dx}(\rho_s \bar{v}) \tag{2.20}$$

Using Fick's law, the species conservation can be further simplified. Fick's law relates the diffusive flux to the mass concentration by using the mass diffusivity $D$:

$$U_M Y_M = -D(\nabla_x Y_M) \tag{2.21}$$

Therefore, Equation (2.20) can be further simplified to:

$$\rho_f D\frac{dY_M}{dx} - (\rho_f u Y_M - \rho_s \bar{v} f_{st}) = \text{constant} \tag{2.22}$$

**Momentum conservation**

In the spray combustion method, the momentum conservation equation is given as [19]:

$$\begin{aligned}\rho_f\frac{\partial u}{\partial t} + \rho_f u\nabla_x.(u) &= -\nabla_x.P + \rho_f\sum_{k=1}^{N} Y_k f_k \\ -\int\int \rho_N\frac{4}{3}\pi R^3 F f dR dv &- \int\int \rho_N 4\pi R^2\dot{R}(v-u)f dR dv\end{aligned} \tag{2.23}$$

where $Y_k$ is the mass fraction of each N particle and $P$ is the total pressure tensor related to the hydrostatic pressure $p$ and the viscous stress tensor T, where $E$ is the unit tensor:

$$P = pE + \mathrm{T} \tag{2.24}$$

The second term in the RHS of Equation (2.23) represents the external body force where $f_k$ is the external body force per unit mass acting on species $k$ in the fluid. The third term in the RHS of Equation (2.23) represents the average force $F$ per unit volume exerted on the particles by the surrounding fluid. The last term accounts for the momentum carried to the fluid by the material from the particles.

Using the distribution function given by Equation (2.3) in the $x$ direction, multiplying it by $\rho_l(4/3)\pi r^3 v$, and integrating it over $v$ and $r$ (after a few integrations by parts), we get:

$$\frac{d}{dx}\left[\bar{v}^2\int_0^\infty \rho_f(4/3)\pi r^3 G dr - \bar{v}\int_0^\infty \rho_f(4/3)\pi r^3 R G dr - \int_0^\infty \rho_f(4/3)\pi r^3 F G dr\right] = 0 \tag{2.25}$$

Using Equations (2.14) and (2.15), this expression may be written in the form:

$$\rho_s \bar{v} \frac{d\bar{v}}{dx} = \int_0^\infty \rho_f (4/3)\pi r^3 FG dr \tag{2.26}$$

By neglecting body forces $f_k$, we can show that:

$$\frac{d}{dx}\left[\rho_f u^2 + \rho_s \bar{v}^2\right] = \frac{dp}{dx} - \frac{d\tau_{xx}}{dx} \tag{2.27}$$

$\tau_{xx}$ is the $xx$ component of the viscous stress tensor T. The equation above may also be written in integrated form:

$$\rho_f u^2 + \rho_s \bar{v}^2 + p + \tau_{xx} = \text{constant} \tag{2.28}$$

For chemical reactions at low mach numbers, such as in most SHS reactions, the pressure gradient is low and the viscous tensor is negligible and therefore, the momentum conservation is not particularly useful in determining the burning velocity.

**Energy conservation**

The energy conservation equation is given as:

$$\begin{aligned}
&\left[\rho_f \left(h_f + \frac{u^2}{2}\right)\right] \frac{\partial p}{\partial t} + \nabla_x . \left[\rho_f u \left(h_f + \frac{u^2}{2}\right)\right] = \\
&= -\nabla_x . q - \nabla_x . (T . u) + \frac{\partial p}{\partial t} + \rho_f \sum_{k=1}^{N} Y_k (u + U_k) . f_k \\
&- \int\int \rho_N \frac{4}{3}\pi R^3 (F . v) f dR dv - \int\int \rho_N 4\pi R^2 \dot{R} \left(h_{in} + \frac{u^2}{2}\right) f dR dv
\end{aligned} \tag{2.29}$$

where $h_f$ is the total enthalpy per unit mass of the fluid, $q$ is the heat flux vector, and $h_{in}$ is the total enthalpy per unit mass of material flowing from particles to the fluid. The last two terms in Equation (2.29) account for the work done on the fluid by the particles and the energy added to the fluid by the material from the surface.

Applying similar assumptions used for the momentum equation and by using the distribution function, the energy equation can be simplified to:

$$\frac{d}{dx}\left(\rho_f u (h_f + u^2/2) + \rho_s \bar{v}(h_f + \bar{v}^2/2)\right) = -\frac{q_x}{dx} - \frac{d}{dx}(\tau_{xx} u) \tag{2.30}$$

which yields:

$$\rho_f u (h_f + u^2/2) + \rho_s \bar{v}(h_f + \bar{v}^2/2) + q_x + \tau_{xx} u = \text{constant} \tag{2.31}$$

To close the system and solve for the conservation equations, the rate at which particles are consumed is needed.

### 2.1.3 Surface Regression Rate

For a single, spherical solid particle of radius $R$ in a fluid, the rate of change of its mass ($M_{Ni}$) caused by the surface reaction is expressed as:

$$M_{Ni} = \rho_N \frac{4}{3}\pi R^3 \qquad \text{so} \qquad \dot{M}_{Ni} = -\frac{d}{dt}\left(\rho_N \frac{4}{3}\pi R^3\right) = \rho_N 4\pi \dot{R} R^2 \tag{2.32}$$

By defining the surface regression rate $\tilde{\chi}$:

$$\tilde{\chi} \equiv -\frac{\dot{M}_{Ni}}{4\pi\rho_M D R} \tag{2.33}$$

we get:

$$-R\dot{R} = \frac{\rho_M D}{\rho_N}\tilde{\chi} \tag{2.34}$$

Here $\tilde{\chi}$ coincides with the definition of the non-dimensional combustion rate, used in solid combustion:

$$\dot{R} = -\frac{\chi}{R}, \qquad \chi = -\frac{\rho_M D}{\rho_N}\tilde{\chi} \tag{2.35}$$

The surface regression rate $\tilde{\chi}$ measures how fast the $N$ solid particles react with the medium $M$. According to Makino and Law [20], an implicit form of $\tilde{\chi}$ can be found:

$$\bar{\chi} = A\frac{\tilde{Y}_{M,e} - \beta}{1+\beta} \tag{2.36}$$

with

$$A = Da_s exp\left(-\frac{T_{a,s}}{T_s}\right) \qquad \beta = exp(\tilde{\chi}) - 1 \tag{2.37}$$

where $A$, $Da_s$, and $\beta$ respectively are the reduced surface Damkohler number, the surface Damkohler number ($= BR/D$), and the Spalding transfer number. Makino [21] provides further approximation of Equation (2.36), with an accuracy of 2%

$$\tilde{\chi} \equiv ln(1+\beta) \approx ln\left(1 + \frac{A}{1+A}Y_{M,e}\right) \tag{2.38}$$

The reduced surface Damkohler number $A$ is a function of the reaction rate over the diffusion rate. As will be explained later in this chapter, the diffusion rate is assumed to be much smaller than the reaction rate for SHS reactions and therefore, $A$ can be assumed to be very large. Hence, the surface regression rate $\tilde{\chi}$ can be assumed to be a function of the stoichiometrically weighted mass fraction $Y_{M,e}$.

### 2.1.4 Change of Variables and Simplification of The Governing Equations

From Equation (2.33), Equation (2.7) can be written as:

$$-\bar{\chi}\frac{\partial\psi}{\partial R}+\bar{v}R\frac{\partial\psi}{\partial x}=0 \tag{2.39}$$

where:

$$\psi\equiv\frac{S\bar{v}G}{R} \tag{2.40}$$

Using transformation to the new independent variables:

$$s^2=R^2-2\int_{-\infty}^{x}\left(\frac{\bar{\chi}}{\bar{v}}\right)dx \qquad \eta^2=R^2+2\int_{-\infty}^{x}\left(\frac{\bar{\chi}}{\bar{v}}\right)dx \tag{2.41}$$

we get:

$$\frac{\partial\psi}{\partial s}=0 \qquad G=\left(\frac{S_0\bar{v}_0}{s\bar{v}}\right)\left(\frac{R}{\eta}\right)G_0(\eta) \tag{2.42}$$

$G$ determines the size distribution $G(R,x)$ at any position $x$ in terms of the distribution $G_0(\eta)$ at the unburned state ($x\to-\infty$).

Introducing the mass fraction of fluid as:

$$Z\equiv\frac{\rho_f}{\rho_f+\rho_s} \tag{2.43}$$

Equation (2.15) becomes:

$$\frac{d(1-z)}{dx}=-\frac{1}{m}\int_0^\infty\rho_N 4\pi R^2\dot{R}GdR \tag{2.44}$$

Following Williams' textbook [19] and using Equations (2.35) and (2.42), Equation (2.44) can be written as:

$$\frac{d(1-z)}{dx}=-\frac{4\pi\rho_N n_0 R_0}{m}\left(\frac{u_0}{u}\chi\right)\left(\frac{1-Z}{1-Z_0}\right)^{1/3} \tag{2.45}$$

Similarly, the species equation (2.22) for the $M$ species is given as:

$$\left(\frac{\rho_f D}{m}\right)\frac{d\tilde{Y}_M}{dx}=\left(\tilde{Y}_M+1\right)Z-\left(\tilde{Y}_{M,0}+1\right)Z_0 \tag{2.46}$$

where $\tilde{Y}_M$ is the stoichiometrically weighted mass fraction ($=Y_M/f_{st}$) and the constant of integration is evaluated at the unburned state ($x\to-\infty$). Also, the Arrhenius mass diffusivity is defined as:

$$D=D_0 exp(-T_d/T) \tag{2.47}$$

For the momentum conservation, the constant pressure assumption is used, which is an accurate assumption since the velocity is low and the velocity gradient is small. The energy conservation equation (2.31) under adiabatic conditions becomes:

$$Zh_f + (1-Z)h_N + \frac{q_x}{m} = Z_0 h_{f,0} + (1-Z_0)h_{N,0} \tag{2.48}$$

Since the flame speed is low ($u^2/2 \ll h_f$ and $u^2/2 \ll h_N$), the kinetic energy can be neglected. The enthalpy of the fluid and particles are respectively given as:

$$h_f = \sum_{k=1}^{N} Y_k h_k; \quad h_k = h_k^0 + c(T - T_0), \quad k = M, P \tag{2.49}$$

$$h_N = h_N^0 + c_N(T - T_0), \tag{2.50}$$

Equation (2.48) states that the internal energy at the unburned state is equal to the internal energy at the burned state plus the energy released, which is the basic definition of the energy equation.

It must also be noticed that we are assuming that the specific heat and the thermal conductivity of the mixture to be constant, which these are not very accurate assumptions for systems with high variation of temperature.

As for the $x$ component of the heat flux vector, when there is no radiation heat transfer, we get:

$$q_x = -K\frac{dT}{dx} + \sum_{k=1}^{N} Y_k h_k \rho_f U_k \tag{2.51}$$

By the use of species conservation equations for metals, products, and the relation between the heat of combustion and enthalpies as:

$$(Y_{M,0} + f_{st})Z_0 - (Y_M + f_{st})Z = \frac{\rho_f Y_M U_M}{m} \tag{2.52}$$

$$\left[Y_{P,0} - (1 - f_{st})\right] Z_0 - \left[Y_P - (1 - f_{st})\right] Z = \frac{\rho_f Y_P U_P}{m} \tag{2.53}$$

$$\begin{aligned} &f_{st}h_M + (1 + f_{st})h_P - h_N = -q^0 + (c - c_N)(T - T^0) \\ &= \frac{v_p W_p h_p - v_M W_M h_M - v_N W_N h_N}{v_N W_N} \end{aligned} \tag{2.54}$$

Equation (2.48) reduces to:

$$\frac{K/c}{m}\frac{d\tilde{T}}{dx} = (\tilde{T} - \tilde{T}_0) - (Z - Z_0) \tag{2.55}$$

$\tilde{T}$ is the non-dimensional temperature ($= \frac{cT}{q^0}$) and $q^0$ is the heat of combustion per unit mass of $N$ species. Energy of phase change is neglected here since it is usually much smaller than the heat of combustion. Other assumptions used here are that the thermal conductivity across the combustion wave is constant, and the specific heats are equal ($c = c_N$).

### 2.1.5 Flame Propagation in an Adiabatic Condition

This section follows the results of papers published by Makino and Law [5, 20, 22]. Here, we only discuss Makino's model for the steady state, adiabatic, one-dimensional, planar, heterogeneous flame propagation in an infinite domain of a compacted medium, originally consisting of a mixture of particles of nonmetal $N$, metal $M$, and product $P$. Using these assumptions, the flame propagation can be derived by solving the governing equations using the boundary conditions at the unburned and burned states.

Using the energy equation (2.55) at the completely reacted state, we can define the condition at the burned state:

$$\tilde{T}_\infty = Z_\infty - Z_0 + \tilde{T}_0 \tag{2.56}$$

From the species equation (2.46), another condition at the burned state is found to be:

$$\tilde{Y}_{M,\infty} = \left(\tilde{Y}_{M,0} + 1\right) \frac{Z_0}{Z_\infty} - 1 \tag{2.57}$$

where $T_0$ is the temperature of the unburned medium, just before the arrival of the flame front of the combustion wave. It must be noted that the effect of $T_0$ , which determines $T_\infty$ through Equation (2.56), is significant because $T_\infty$ exponentially influences the reaction rate and mass diffusivity (Equation (2.47))in the condensed phase.

It is also useful to define new parameters, such as the mixture ratio $\mu$ (the initial molar ratio of nonmetal, $N$, to metal, $M$, divided by the corresponding stoichiometric molar ratio) and the initial mass fraction of the diluent $\kappa$ [20]:

$$\mu = \frac{f_{st}}{Y_{M,0}} \frac{1 - Z_0}{Z_0}, \qquad \kappa = (1 - Y_{M,0}) Z_0 \tag{2.58}$$

For a unity mixture ratio $\mu$ (i.e., an stoichiometric situation where all metal and non-metal particles are reacted) at the burned state, where there is only fluid, we get $Z_\infty = 1$. This simplifies Equations (2.56) and (2.57) to:

$$\tilde{T}_\infty = 1 - Z_0 + \tilde{T}_0 \tag{2.59}$$

$$\tilde{Y}_{M,\infty} = \left(\tilde{Y}_{M,0} + 1\right) Z_0 - 1 \tag{2.60}$$

### 2.1.6 Burning Velocity

It is more convenient to define non-dimensional variables and derive the conservation equations based on these variables:

$$\theta = \frac{\tilde{T} - \tilde{T}_0}{\tilde{T}_\infty - \tilde{T}_0}, \quad \zeta = \frac{\tilde{Y}_M - \tilde{Y}_{M,0}}{\tilde{Y}_{M,\infty} - \tilde{Y}_{M,0}}, \quad \xi = \frac{\tilde{Z} - \tilde{Z}_0}{\tilde{Z}_\infty - \tilde{Z}_0} \tag{2.61}$$

In order to solve the species and energy equations, some boundary conditions must be known. Different assumptions are used in Makino's model for setting the boundary conditions. Makino assumed that before the arrival of the combustion wave, the effects of the reaction cannot be remarkable due to the low temperature and small area of contact between particles. By melting the $M$ particles, the temperature and contact surface are increased and then the reaction initiates. The boundary conditions with this assumption become:

$$\text{unburned} \qquad \xi = 0, \quad \theta = \theta_m, \quad \zeta = 0 \tag{2.62}$$

$$\text{burned :} \qquad \xi = 1, \quad \theta = 1, \quad \zeta = 1 \tag{2.63}$$

As mentioned earlier, momentum equation is not used for solving the burning velocity for low Mach number reactions. Therefore, using the non-dimensional variables in the energy equation (2.55) and the species equation (2.46), we can get:

$$\frac{d\theta}{d\xi} = \frac{\Lambda_0(\rho_{t,0}/\rho_t)}{(1-\xi)^{1/3}\tilde{\chi}} exp\left(\frac{\tilde{T}_d}{\tilde{T}}\right)\frac{\theta - \xi}{1 - Z_0} \tag{2.64}$$

and

$$\frac{d\zeta}{d\xi} = \frac{Le_0\Lambda_0(\rho_{t,0}/\rho_t)^2}{[Z_0 + (1-Z_0)\xi]\,(1-\xi)^{1/3}\tilde{\chi}} exp\left(\frac{2\tilde{T}_d}{\tilde{T}}\right)\left[\left(\zeta - \frac{Z_\infty}{Z_\infty - Z_0}\right)\xi + \frac{Z_0\zeta}{1-Z_0}\right] \tag{2.65}$$

Here, the Lewis number $Le_0$ defines a ratio between the thermal diffusivity and the mass diffusivity:

$$Le_0 = \frac{(K/c)}{(\rho_t D)_0} \tag{2.66}$$

and $\Lambda_0$ is the mass burning rate eigenvalue:

$$\Lambda_0 = \frac{(Z_\infty - Z_0)^2 m_a^2}{4\pi(\rho_M D_0)(K/c)n_0 R_0} \tag{2.67}$$

where $m_a$ is the total mass burning rate in the adiabatic condition. The problem here is reduced to solving the mass burning rate $m_a$ for two first-order ordinary differential

equations (2.64) and (2.65) for under-stoichiometric mixture ratios. It is suggested that the surface Damkohler number $A$ and the surface regression rate $\tilde{\chi}$ depend on the particle radius $R$ because of the existence of the surface reaction and so the particle radius varies as $R = R_o(1-\xi)^{1/3}$ [5]. Once the specific value of $\Lambda$ is obtained by a numerical calculation, the burning velocity is then calculated by rewriting $\Lambda$ in Equation (2.67):

$$u_0 = \left(\frac{1 - Z_0}{Z_\infty - Z_0}\right)\left(\frac{D_0\sqrt{3\Lambda Le_0}}{R_0}\right)\sqrt{\frac{\rho_M/\rho_N}{1 - Z_0}} \tag{2.68}$$

which for unity mixture ratio $\mu = 1$, it is simplified to:

$$u_0 = \frac{D_0\sqrt{3\Lambda Le_0}}{R_0}\sqrt{\frac{\rho_M/\rho_N}{1 - Z_0}} \tag{2.69}$$

where $u_0$ in experiments is simply the velocity of the flame.

### 2.1.7 Numerical Approach for Deriving Mass Burning Rate Eigenvalue $\Lambda$

According to Makino, for most SHS processes, the diffusion-controlled reaction prevails and the Lewis number $Le_0$ is very large in the consumption zone [5]. In other words, due to low heat transfer, the diffusion rate is much lower than the reaction rate and therefore, the mass burning rate is mainly dependent to the diffusion rate. Using this argument, we can assume a very large Lewis number for Equation (2.38) and we get:

$$\tilde{\chi} \approx ln(1 + \tilde{Y}_M) \tag{2.70}$$

Since the rate of diffusion is very slow compared to thermometric conductivity and reaction rate, the last part of Equation (2.65) can be neglected, so we get:

$$\zeta \approx \frac{\xi}{Z_0 + (1 - Z_0)\xi} \tag{2.71}$$

Flame speeds obtained with these two assumptions are are found to be practically indistinguishable from numerical results [22]. Using Equations (2.70) and (2.71), Equation (2.64) is expressed in integral form as:

$$\int_{\theta_m}^{1} exp\left(-\frac{\tilde{T}_d}{\tilde{T}}\right) = (1 + \gamma)\Lambda_0 \times \int_0^1 \frac{\theta - \xi}{(1 - \xi)^{1/3} ln\left(1 + \frac{(\phi - \xi)}{(\xi + \gamma)}\right)} d\xi \tag{2.72}$$

where $\phi = 1/\mu$ and $\gamma = Z_0/(1 - Z_0) = (\mu\kappa + f)/[\mu(1 - \kappa)]$. The integral of the LHS of Equation (2.72) is evaluated by performing an asymptotic expansion for large values of $\beta = \frac{\tilde{T}_d(\tilde{T}_\infty - \tilde{T}_0)}{\tilde{T}_\infty^2}$ up to the second term in the expansion.

For integrating the RHS of Equation (2.72), Makino attempted to express $\theta$ with $(1-\xi)$ and $(1 - \xi^{1/3})$ [22]. Therefore, by comparing the numerical results, the following relation is found:

$$(1 - \theta) = \frac{(1 - \theta_m)}{2}(1 - \xi) \tag{2.73}$$

Equation (2.73) represents the temperature profile at high temperatures. The details for the derivations of the LHS and RHS can be found in Makino's paper [22], for which the mass burning rate eigenvalue was shown to be:

$$\Lambda_o \approx \frac{\mu^2(1 - \kappa)^2 exp(-\beta/\alpha)}{(\mu + f_{st})\left[(1 + f_{st}) - \kappa(1 + \theta_m)\right]\beta(1 + \theta_m)} \tag{2.74}$$

Replacing $\Lambda_o$ in Equation 2.75 by Equation 2.74, an explicit equation for the flame speed can be obtained:

$$u_0 = \frac{D_0\sqrt{3\left(\frac{\mu^2(1-\kappa)^2 exp(-\beta/\alpha)}{(\mu+f_{st})[(1+f_{st})-\kappa(1+\theta_m)]\beta(1+\theta_m)}\right)\frac{(K/c)}{(\rho_t D)_0}}}{R_0}\sqrt{\frac{\rho_M/\rho_N}{1 - Z_0}} \tag{2.75}$$

This equation relates the flame speed to the initial conditions and different properties of the metal and non metal mixtures. Later in Chapter 5, the parameters in this equation will be discussed to obtain a relation between the flame speed and the mixture porosity.

# Chapter 3

# Thermal conductivity in powder compacts: Review

The present chapter provides a review of the models used to predict the thermal conductivity in powder compacts. Closed form analytical models and numerical methods are reviewed. The last section of the present Chapter is a review of experimental methods used to measure the conductivity in powder compacts.

## 3.1 Theoretical Models for Predicting the Thermal Conductivity of Porous Materials

In this section, different models for estimating thermal heat conductivity in porous materials are described. Before looking into these models, we must first make the distinction between the different types of porous materials. There are two categories of porous materials, illustrated in Figure 3.1, defined as:

- **Internal porosity materials:** Materials in which air, for instance, is dispersed within a continuous condensed phase (i.e. solid or liquid) such as foams and sponges (Figure 3.1a).
- **External porosity materials:** Particulate-type materials in which air, for instance, is within a continuous phase such as powders (Figure 3.1b).

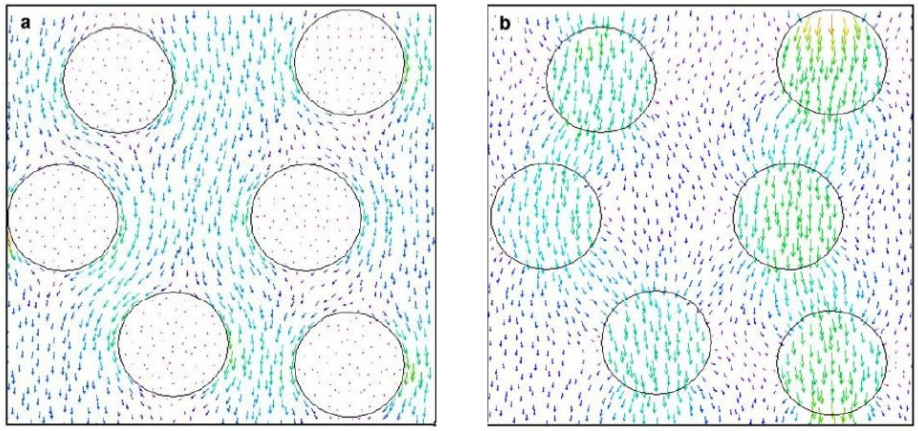


**(a)** Internal porosity materials $k_{cont} \gg k_{disp}$ **(b)** External porosity materials $k_{disp} \gg k_{cont}$

**Figure 3.1:** Porosity comparison [18]

### 3.1.1 Series and Parallel Models

The series and parallel models for heterogeneous materials are shown schematically in Figure 3.2. They consist in representing the material as a layered system, either aligned perpendicularly to the heat flow (series model) or parallel to the heat flow (parallel model). These two models are also referred to as the Wiener bounds [23]. They serve as the lower and upper bounds for the effective conductivity of porous materials when conduction is the only mechanism of heat transfer involved. The derivations of these two models follow a simple thermal resistance method, as shown in Figure 3.3, resulting in effective conductivities that take the form [23]:

$$K_{e,series} = \frac{1}{(1 - v_2)/K_1 + v_2/K_2} \tag{3.1}$$

$$K_{e,parallel} = (1 - v_2) K_1 + v_2 K_2 \tag{3.2}$$

where $v$ is the volume fraction, $K$ is the thermal conductivity, and $K_e$ is the total effective conductivity. The subscripts 1 and 2 refer to either of the two materials.

Both series and parallel models are not accurate in predicting the thermal conductivity of porous mixtures, but they serve as a good approximation for the extreme cases. It is suggested that the highest and lowest possible effective thermal conductivity of porous materials lie between these two models [23], i.e.,

$$K_{e,series} < K_e < K_{e,parallel} \tag{3.3}$$

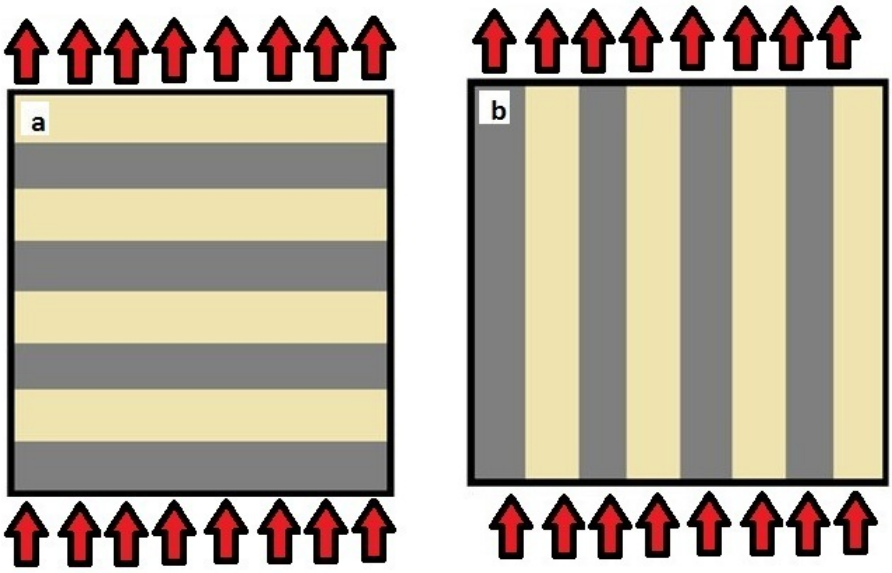


**(a)** Series model **(b)** Parallel model

**Figure 3.2:** Series and parallel thermal conductivity models

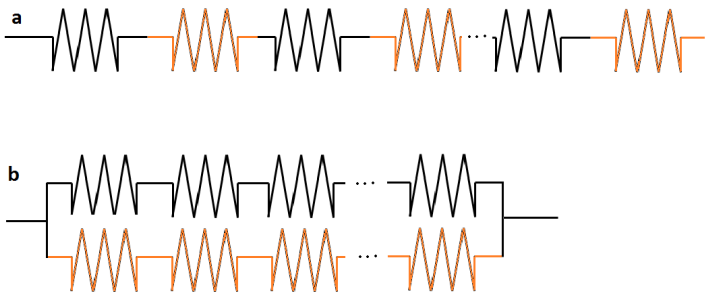


**Figure 3.3:** Thermal resistance of a) Series model and b) Parallel model

### 3.1.2 Maxwell's model

The Maxwell model is one of the most popular techniques for predicting the heat conductivity of multiphase mixtures [24]. This model assumes a system as shown in Figure 3.1. A uniform medium $m$ with conductivity $K_m$ has spherical inclusions of material $s$, having a different conductivity $K_s$. For sufficiently dilute inclusions, the effect of one inclusion on others is negligible, and one can analyze a single such spherical inclusion, as shown Figure 3.4. For such an arrangement, the energy equation can be expressed in spherical coordinates. Under steady-state conditions, and ignoring heat convection and heat generation, this energy equation reduces to the Laplace equation. In spherical polar coordinates, it

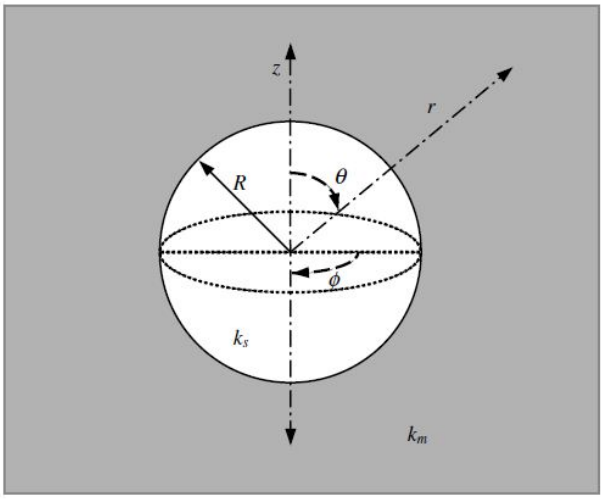


**Figure 3.4:** Single sphere of conductivity $k_s$ contained within a continuous medium of conductivity $k_m$ [18]

takes the form [24]:

$$\frac{1}{r^2}\frac{\partial}{\partial r}\left(r^2\frac{\partial T}{\partial r}\right)+\frac{1}{r^2\sin\theta}\frac{\partial}{\partial\theta}\left(\sin\theta\frac{\partial T}{\partial\theta}\right)+\frac{1}{r^2\sin^2\theta}\frac{\partial^2 T}{\partial\phi^2}=0 \tag{3.4}$$

Taking the center of the sphere as the origin, and assuming symmetry about the z-axis such that $T$ is independent of $\phi$, a general solution of the Laplace equation is found to be:

$$T=A+\frac{B}{r}+Cr\cos\theta+\frac{D}{r^2}\cos\theta \tag{3.5}$$

where $A$, $B$, $C$, and $D$ are constants, which are determined with the following boundary conditions. The temperature is finite at $r=0$, i.e.,

$$\text{at}\quad r=0,\quad T_s\neq\infty \tag{3.6}$$

At the surface of the sphere, the heat conduction from the outside medium is the heat conduction into the sphere material, i.e.,

$$\text{at}\quad r=R,\quad K_s\frac{\partial T_s}{\partial r}=K_m\frac{\partial T_m}{\partial r} \tag{3.7}$$

Furthermore, at the surface of the sphere, the temperatures and temperature gradients tangential to the sphere surface are equal, i.e.,

$$\text{at}\quad r=R,\quad T_s=T_m\quad\text{and}\quad\frac{\partial T_s}{\partial\theta}=\frac{\partial T_m}{\partial\theta} \tag{3.8}$$

Far away from the sphere, the temperature profile is:

$$\text{at} \quad r \gg R, \quad T_m = bz = br\cos\theta \tag{3.9}$$

where $b$, which has units of degree per length, is the magnitude of the temperature gradient in the continuous medium.

Using these boundary conditions, it is possible to solve for the constants $A$, $B$, $C$, and $D$ in Equation 3.5 and therefore, derive an explicit equation for the temperature profile inside the sphere as well as in the medium. These take the form:

$$T_s = b\frac{3K_m}{K_s + K_m} r\cos\theta \tag{3.10}$$

$$T_m = br\cos\theta - bR^3\frac{K_s - K_m}{K_s + 2K_m}\frac{\cos\theta}{r^2} \tag{3.11}$$

Next, we consider a situation where $n$ small spheres of radius $R_2$ and conductivity $K_2$ are contained within a single larger sphere $R_1$ and conductivity $K_1$. In such a case, we can assume that the local distortions to the temperature distributions around the smaller spheres do not affect their neighbours:

$$T_m = br\cos\theta - bnR_2^3\frac{K_2 - K_1}{K_2 + 2K_1}\frac{\cos\theta}{r^2} \tag{3.12}$$

which can be rewritten as

$$T_m = br\cos\theta - bv_2R_1^3\frac{K_2 - K_1}{K_2 + 2K_1}\frac{\cos\theta}{r^2} \tag{3.13}$$

where

$$v_2 = \frac{nR_2^2}{R_1^3} \tag{3.14}$$

Now, if the large sphere was filled with a material having an effective conductivity $K_e$, Equation 3.13 becomes:

$$T_s = br\cos\theta - bR_1^3\frac{K_e - K_1}{K_e + 2K_1}\frac{\cos\theta}{r^2} \tag{3.15}$$

In order for Equations 3.13 and 3.15 to produce the same result, we require:

$$\frac{K_e - K_1}{K_e + 2K_1} = v_2\frac{K_2 - K_1}{K_2 + 2K_1} \tag{3.16}$$

Equation 3.16 can be rewritten in explicit form for $K_e$:

$$K_e = \frac{2v_2\frac{K_2 - K_1}{K_2 + 2K_1}K_1 + K_1}{1 - v_2\frac{K_2 - K_1}{K_2 + 2K_1}} \tag{3.17}$$

This equation satisfies both types of porous materials (external and internal) simply by switching the subscripts 1 with 2.

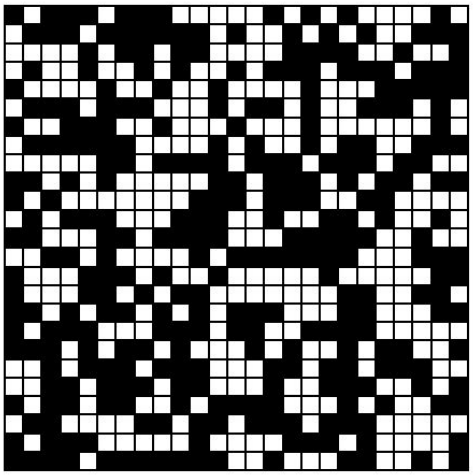

**Figure 3.5:** Schematic diagram of a material made up of a random dispersion of two components [18]

### 3.1.3 Effective Medium Theory (EMT)

The structure shown in Figure 3.5 represents a heterogeneous material where the two components are distributed randomly, regardless of the phases being continuous or dispersed. Both components can form a continuous heat conduction pathway and therefore, this structure is "unbiased" towards its components. The effective conductivity of this type of structure is modeled well by the Effective Medium Theory (EMT) [18]. This theory is also derived from the solution of the Laplace equation applied to a single sphere of radius $R$ and conductivity $K_s$ surrounded by a continuous medium of conductivity $K_m$ (shown in Figure 3.4), and subjected to a steady-state temperature gradient in the direction of the z-axis.

The difference between the Maxwell and EMT models is based on the different assumptions used in the models in the derivations involving multiple components [25]. Based on Landauer's model [26, 27], the effect of individual particles on the temperature profile can be averaged. Similar to Maxwell, the temperature distribution within the material can be approximated by a material having a uniform temperature distribution and thermal conductivity $K_e$ [26]. The difference of the EMT model is caused by assuming the net effect from the second term on the RHS of equation 3.11 to be zero. This gives the following expression,

$$\int_V \left( \frac{K_i - K_e}{K_i + 2K_e} \right) p(K_i) dK = 0 \tag{3.18}$$

where $p(K_i)d_K$ is the probability of a component at an arbitrary location with a thermal

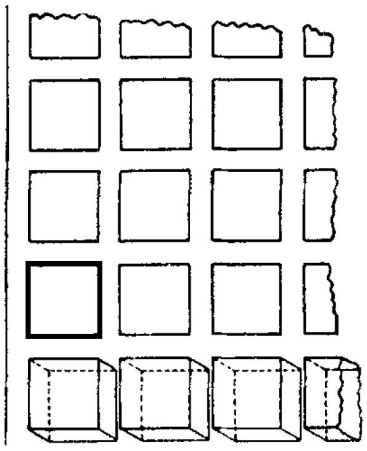

**Figure 3.6:** Russel's first type of porous model [28]

conductivity of $K_i$.

It can be shown that this probability is proportional to the volume fraction $v_i$ occupied by the component. Thus for $n$ components, we get:

$$\sum_{n}^{i=1} \left( \frac{K_i - K_e}{K_i + 2K_e} \right) v_i = 0 \tag{3.19}$$

Solving this equation for a mixture with two components, we get an implicit equation for the effective conductivity:

$$(1 - v_2) \frac{K_1 - K_e}{K_1 + 2K_e} + v_2 \frac{K_2 - K_e}{K_2 + 2K_e} = 0 \tag{3.20}$$

which can also be rewritten in an explicit form for $K_e$:

$$K_e = \frac{1}{4}[(3v_2 - 1)K_2 + [3(1 - v_2) - 1] K_1 + \sqrt{[(3v_2 - 1) K_2 + (3 (1 - v_2) - 1) K_1]^2 + 8K_1K_2}] \tag{3.21}$$

This model satisfies both external and internal porosity materials.

### 3.1.4 Russell Method

In 1934, Russel [28] suggested a model for calculating the thermal conductivity of porous materials by proposing two different scenarios.

The first scenario in this method considers a brick with cubic shape pockets, as shown in Figure 3.6. Assuming that the isothermal surfaces are planes, by the laws of conductors,

in series and in parallel, the conductivity of the brick can be expressed as [28]:

$$\frac{K_e}{K_s} = \frac{(1-v)^{2/3} + \frac{K_s}{K_a}(1-(1-v)^{2/3})}{(1-v)^{2/3} - (1-v) + \frac{K_s}{K_a}(1-(1-v)^{2/3} + (1-v))} \tag{3.22}$$

where $v$ is the volume fraction of the solid and $K_e$, $K_s$, and $K_a$ are the conductivities of the brick (effective conductivity), of the solid, and of air, respectively.

The second scenario considers the case of a brick in which the pores are placed between granules. Therefore, it is assumed that the granules are solid cubes which are all the same size, and separated by layers of air of similar thickness. The structure is thus the reverse of the first case and the bricks only touch in a limited number of points. The conductivity equation for such a scenario is the same as the first scenario while replacing $v$ by $(1-v)$ and interchanging $K_s$ and $K_a$ [28].

$$\frac{K_e}{K_a} = \frac{v^{2/3} + \frac{K_a}{K_s}(1-v^{2/3})}{v^{2/3} - v + \frac{K_a}{K_s}(1-v^{2/3} + (1-v))} \tag{3.23}$$

This model is also applicable to both external and internal porosity materials.

### 3.1.5 Empirical Approach

Aside from analytical techniques, an empirical approach has also been suggested by Aivazov and Domashnev [29], where they used the model suggested by Odelevskii. Odelevskii derived an expression for the thermal conductivity as a function of inclusion concentration for a matrix system with cubic inclusions whose centers form a cubic lattice [29]:

$$K = K_0 \left(1 + \frac{v_1}{\frac{1-v_1}{3} + \frac{K_0}{K_1 - K_0}}\right) \tag{3.24}$$

where the subscripts 0 and 1 refer to the medium and the inclusions. Aivazov and Domashnev showed that this equation for spherical and cylindrical inclusions can be simplified to:

$$\begin{aligned} &\text{Spherical :} \qquad K = K_0 \frac{1-v_1}{1+0.5v_1^2} \\ &\text{Cylindrical :} \qquad K = K_0 \frac{1-v_1}{1+1v_1^2} \end{aligned} \tag{3.25}$$

They suggested that depending on the shape of the powders, this equation can be generalized to an empirical approximation:

$$K = K_0 \frac{1-v_1}{1+nv_1^2} \tag{3.26}$$

where $n$ is the empirical constant determined experimentally. It is suggested that this equation is more accurate for external porosity materials.

In most analytical approaches for calculating the thermal conductivity of porous materials, the shapes are assigned to be fixed (such as sphere, cube or cylindrical powders). However, for true porous materials, the shapes of powders are non-uniform and this can increase the error of the model. The main advantage of this empirical approach is that the user can input the effect of powder shapes into the model by assigning $n$, thus reducing the error of the approximation caused by the ranges in size and structures of powders.

### 3.1.6 Iwan Sumirat Model

Sumirat [30] estimated the thermal conductivity of porous materials from the definition of the kinetic theory of phonons in solids. Based on this theory, the thermal conductivity of an insulating solid can be expressed as [30]:

$$K = \frac{1}{3} c \dot{x} l \tag{3.27}$$

where $c$ is the heat capacity per unit volume, $\dot{x}$ is the average phonon velocity, and $l$ is the mean free path of a phonon between scatterings.

Understanding the dependence of $c$, $\dot{x}$, and $l$ on porosity and based on Equation 3.27, a relation between porosity and conductivity can be obtained. According to Sumirat, $c$ in porous materials is directly proportional to porosity $\phi$, i.e.,

$$c = c_0(1 - \phi) \tag{3.28}$$

where $c_0$ is the heat capacity at $\phi = 0$.

Since the phonon velocity in insulating solids is mostly determined by short-range interactions, it can be assumed that the velocity $\dot{x}$ is independent of porosity, i.e.,

$$\dot{x} = \dot{x}_0 \tag{3.29}$$

In a different approach, Sumirat derived an equation for the mean free path of a phonon based on the mean free path of a phonon at $\phi = 0$ ($l_0$) and the mean free path of phonon-pore scattering $l_p$:

$$l = l_0 \left(1 + \frac{l_0}{l_p}\right) \tag{3.30}$$

In order to find the phonon mean path $l$ in porous materials, a simple model for a nanoporous material is used in which isolated spherical or cubic pores are distributed

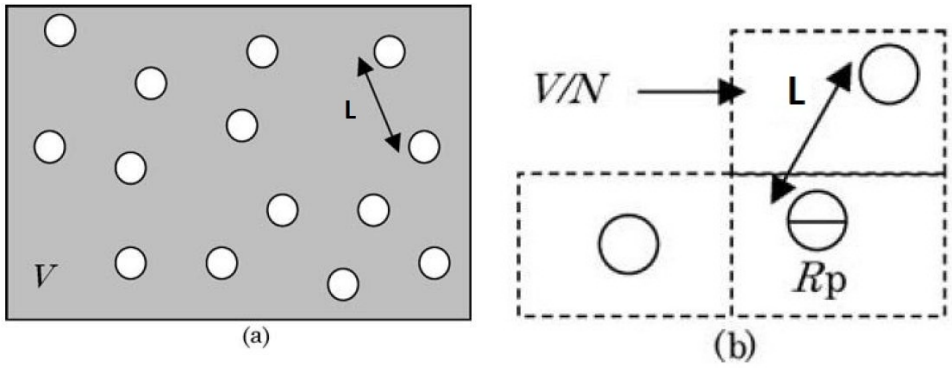


**(a)** A porous material of volume $V$ with the mean distance $D$ between adjacent pores

**(b)** The volume per pore, $V/N$ for a material with $N$ pores of pore size $R_p$

**Figure 3.7:** Schematic view of Sumirat model [30]

randomly as shown in Figure 3.7 ($V$ and $N$ are the volume and the number of pores in the material). The volume of one pore $v_p$ can thus be approximated by the pore size $R_p$:

$$v_p \approx R_p^3 \tag{3.31}$$

By assuming that the mean free path of phonon-pore scattering $l_p$ is almost equal to the mean distance between adjacent pores $l_p \cong L$, equation 3.30 can be rewritten as:

$$l = l_0 \left( \frac{l_0}{1 + \frac{l_0}{R_p}\phi^{1/3}} \right) \tag{3.32}$$

Substituting equations 3.28 and 3.32 into equation 3.27 [30]:

$$\frac{K_e}{K_0} = \frac{1-\phi}{1 + \frac{l_0}{R_p}\phi^{1/3}} \tag{3.33}$$

This model is suggested to be more accurate for powders with nano-scale structures.

### 3.1.7 Kwon's Model

In 2008, Kwon [31] suggested a model for predicting the thermal conductivity of spherical materials. His theory is based on the contact area between the powders which are created by the force applied to the powders and neglecting the conductivity of air.

Based on the Hertz contact theory [32], the contact resistance can be calculated using the contact modulus defining the elastic properties of spheres 1 and 2, as shown in Figure 3.8:

$$\frac{1}{E_0} = \frac{1-v_1^2}{E_1} + \frac{1-v_2^2}{E_2} \qquad \frac{1}{r_0} = \frac{1}{r_1} + \frac{1}{r_2} \tag{3.34}$$

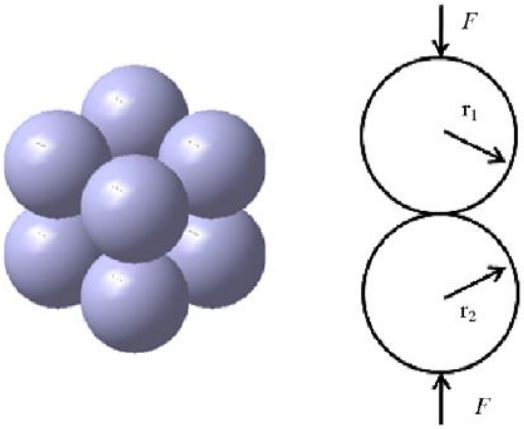


**Figure 3.8:** Simple cubic model for packed sphere [31]

where $E$ is Young's modulus. The true radius of contact circle is defined as:

$$r_c = \left(\frac{3Fr_0}{4E_0}\right)^{1/3} \tag{3.35}$$

where $F$ is the external force loaded on the sphere. Using simple heat transfer analysis along two spheres, it can be shown that:

$$q = 4r_c \left(\frac{1}{K_{p,1}} + \frac{1}{K_{p,2}}\right)^{-1} (T_1 - T_2) \tag{3.36}$$

where $K_p$ is the thermal conductivity of the sphere and $T$ is the temperature of the sphere. Based on equation 3.36 and assuming an identical material for all powders, the thermal conductivity along two spheres can be found [31]:

$$K_e = K_s \left(\frac{3(1-v^2)P_{atm}}{E}\right)^{1/3} \tag{3.37}$$

A similar procedure is used to estimate the thermal conductivity for hexagonal close packed models shown in Figure 3.9:

$$K_e = K_s \left(\frac{96(1-v^2)P_{atm}}{E}\right)^{1/3} \tag{3.38}$$

Using the size and the total mass of the powders, the effective conductivity of the mixture can be estimated.

This model is highly dependent on the size, the shape, and alignments of powders. In most cases, there is no particular shape or alignment for a powder mixture and therefore, this method can lose accuracy. This model is only suggested for large spheres which the macro-structure of the mixture can be easily observed.

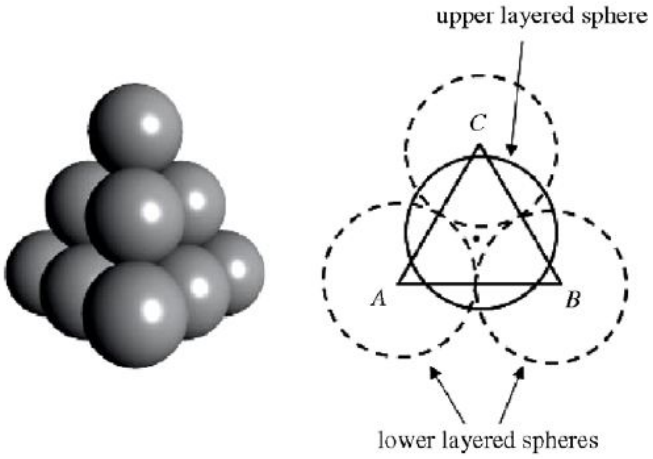


**Figure 3.9:** Hexagonal closed packed model [31]

### 3.1.8 Numerical approaches

While analytical models are restricted to pre-determined geometries, numerical simulations of heat conduction in irregularly shaped powder compacts are now possible, provided the geometry is specified.

One example of this numerical approach is by Carson *et al.* [33]. He used a finite element method, simulating steady-state thermal conductivity by performing measurements on theoretical materials with varying structures. Two-dimensional finite element simulations were used to examine the relative influences of selected porosity-related variables on the effective thermal conductivity.

The results of their work indicated that the effects of contact between pores or particles and the effect of porous structure on the thermal conductivity are more significant than the size or shape of individual pores or particles. More importantly, their results verified that external porosity materials should be considered separately to internal porosity materials when predicting the effective thermal conductivity.

Additionally, his model showed that it is unrealistic to expect a model which is only a function of the thermal conductivity and volume fraction to provide accurate predictions for all porous materials, since the effective thermal conductivity is dependent on the shapes, alignments, and sizes of porous materials.

When the geometry of the porous materials is not known, a numerical method can serve as a quick guide to test the influence of various assumptions made in the analytical models above. Such an implementation can be found in Appendix A, where the finite element code ANSYS was used to model heat conduction in heterogeneous materials.

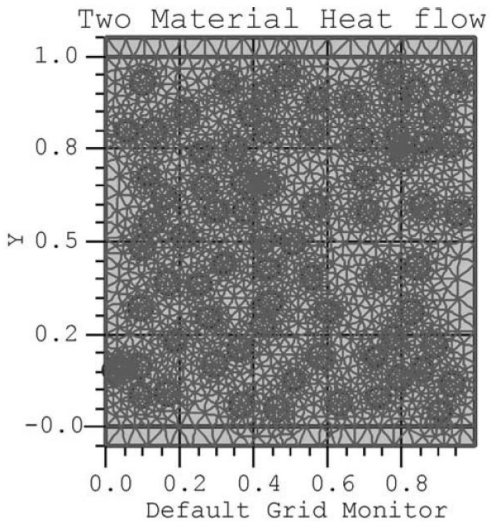


**Figure 3.10:** Example of the finite element grids used by J.K. Carson in numerical simulations [33]

The numerical simulations given in Appendix A showed that the results are very sensitive to the shape and the structure of the porous materials. Therefore, exact values are not reliable for these models unless the structure of the porous material is known with a high degree of certainty.

### 3.1.9 Comparisons of Models

To summarize the information in this section, it is important to first clarify what type of porous materials each model can be used for, as shown in Table 3.1.

It is well established that the effective conductivity of powders depends on a variety of parameters such as the type of porosity, relative density, conductivity of medium and solids, contact area between solid particles, roughness, and sizes of particles [34]. Therefore, it is important to choose models that match with the mixtures used in the experiments.

The Sumirat and Kwon models have size restrictions; the Sumirat model can only be applied for nano-size structures and Kwon's model is mostly used for larger spheres (>0.01 cm).

Most numerical approaches are time consuming while they predict very similar results to analytical models for simple geometries. For complex geometries, they are sensitive to the fine details, hence require this information. When this information is not known, analytical models should be preferred instead.

**Table 3.1:** Thermal conductivity model of porous mixtures

| Models | External Porosity | Internal Porosity |
|---|---|---|
| 1- Series | ✓ | |
| 2- Parallel | | ✓ |
| 3- Maxwell | | ✓ |
| 4- Effective Medium Theory | ✓ | ✓ |
| 5- Empirical Approach | ✓ | |
| 6- Russel | ✓ | ✓ |
| 7- Sumirat | ✓ | |
| 8- Kwon | ✓ | |
| 9- Numerical Approach | ✓ | |

Figure 3.11 presents the thermal conductivity of a porous material mixture where the conductivity of the medium and pores are chosen arbitrarily. To see the difference between different methods, the Y axis is plotted in a log scale. Each color presents a mixture with a certain porous structure. $K_{TMD}$ in this graph is defined as the thermal conductivity at the theoretical maximum density.

Series and Parallel models are generally used to obtain the boundaries for the effective conductivity of the mixtures $K_e$ and therefore they are not accurate for estimating the exact values of $K_e$.

Maxwell theory is an accurate technique for determining the thermal conductivity of internal porosity mixtures. However, this model neglects the heat conductivity between spheres. As a result, this model is proven to be inaccurate for the external porosity mixtures.

Effective medium theory (EMT), an improved model of the Maxwell theory, has improved accuracy compared to Maxwell, particularly for external porosity materials . However, this model is unbiased towards internal and external porosity materials, so it is comparatively not a very accurate model for external porosity mixtures compared to models derived specifically for external porosity materials. As a result, this model can be used for materials which are a mixture of internal and external porosity materials.

Russel's model, on the other hand, covers both types of porous materials. The main source of errors in Russel's model is caused by using cubic particles for external porosity mixtures or cubic holes for internal porosity materials. This assumption creates uncer-

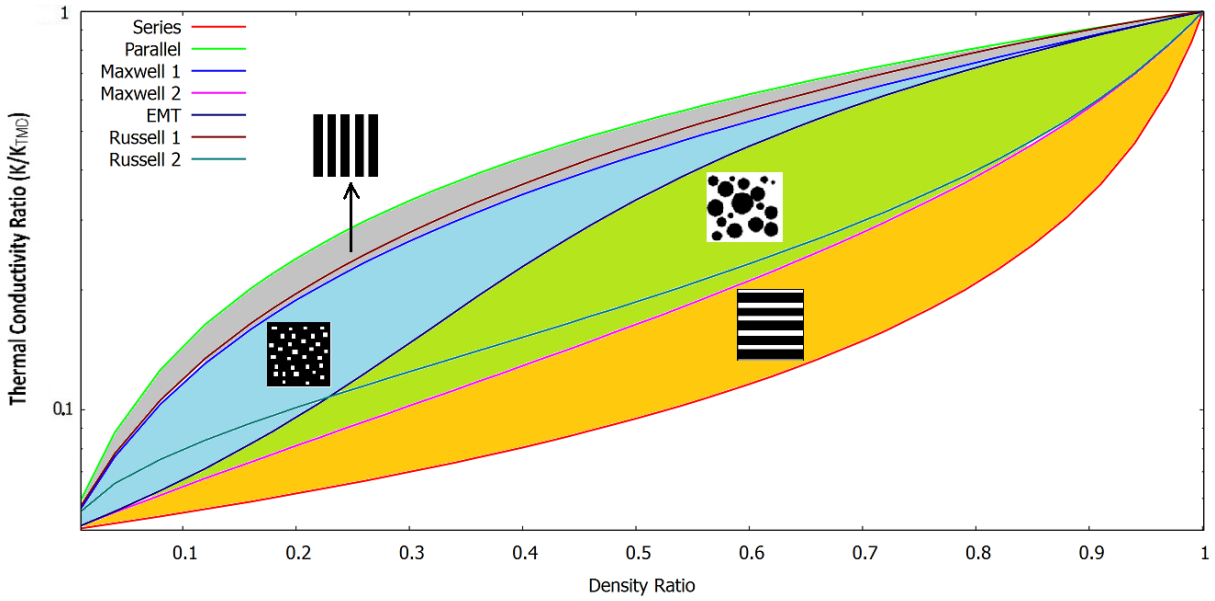


**Figure 3.11:** Our comparison of different methods for estimating the thermal conductivity of porous materials (log scale)

tainties for matching this model with powders, since the powders consist of spherical or other non-cubic shapes.

The empirical approach suggested by Aivazov and Domashnev is an accurate technique for estimating thermal conductivity of external porous mixtures, such as powders, since the errors caused by the sizes, shapes, and the alignments of powders can be reduced by introducing the empirical constant in the equation. The main difficulty of this model is caused by having to experimentally measure the thermal conductivity of the powders at different density ratios.

As a result, in order to use the empirical approach, we need to review different experimental methods for determining thermal conductivity of powders. By experimentally measuring the thermal conductivity of powders we can set the empirical constant $n$, and also verify the accuracy of different analytical models using our experimental results.

There exist other models for predicting the thermal conductivity of porous materials, but their usage is restricted by specific types of materials and shapes. As a result, these models were not discussed in this section. For example, Kuriger [35] predicted a model for the thermal conductivity of porous materials composed of thermoplastic composites. Also, Wang [36] derived a model for predicting the effective thermal conductivity of random open-cell porous foams.

Therefore, the accepted methods for different porosity materials, EMT and Maxwell

models, are suitable for investigating internal porosity materials and the empirical technique suggested by Aivazov is an acceptable method for investigating external porosity materials.

## 3.2 Experimental Methods for Measuring the Thermal Conductivity of Porous Materials

In this section, different experimental methods for measuring the thermal conductivity of porous mixtures are reviewed. Unlike analytical methods, most experimental methods for estimating the thermal conductivity are unbiased towards the type of porous materials. Moreover, in some cases, the techniques used in the experiments are identical, or very similar, to procedures used for non-porous materials.

### 3.2.1 Steady State, Divided Bar Technique

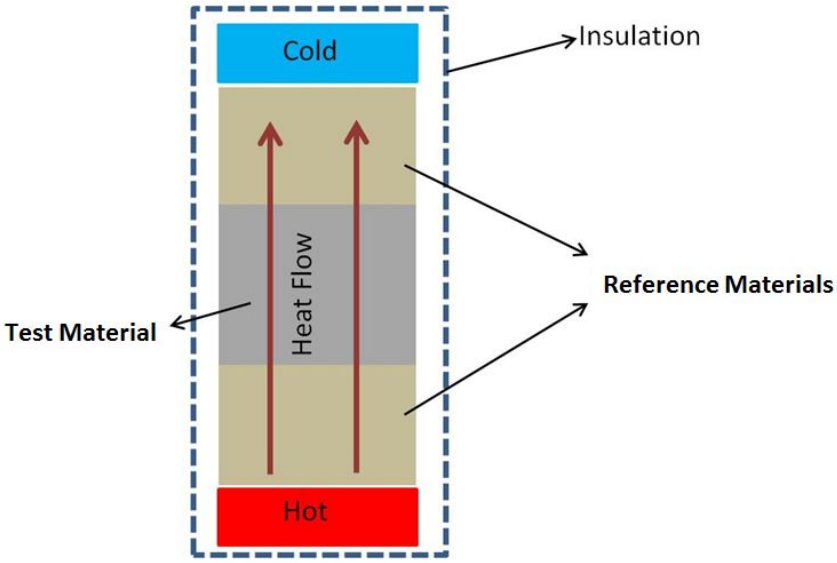


**Figure 3.12:** Schematic of divided bar technique model

In the *divided bar technique*, as shown in Figure 3.12, a test specimen is sandwiched under a load between two reference materials. Each reference material is in contact with the flat plate of a heating/cooling unit with the whole setup being insulated. A temperature gradient is established along the stack allowing for the thermal conductivity to be

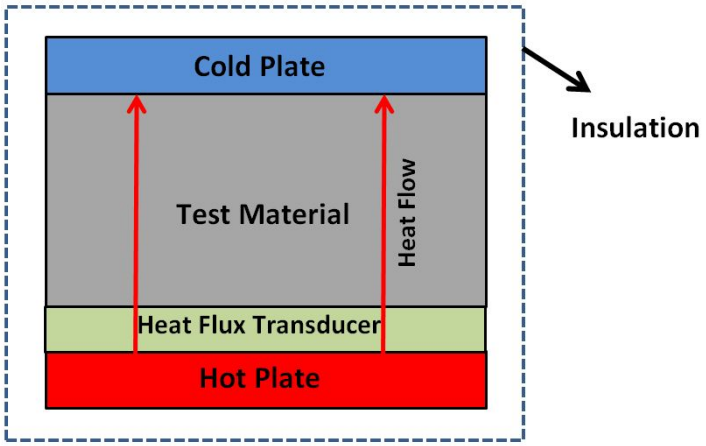


**Figure 3.13:** Schematic of heat flux transducer

estimated by measuring the temperature differences across the reference and test specimens. The heat flux can be estimated by measuring the temperature along the reference solids, since they have known thermal conductivities. Using the estimated heat flux and measuring the temperature gradient along the test specimen, the thermal conductivity of the test specimen can be estimated.

The divided bar technique is a relatively simple concept, versatile, flexible and highly adaptable. It can be used over a high range of temperatures (100 K to 1300 K) of homogeneous, heterogeneous, composite solids, etc. [37].

### 3.2.2 Heat Flux Transducer

The *heat flux transducer method* is very similar to the divided bar technique. The test specimen is sandwiched and pressed under a load, each in contact with a flat plate of a heating and cooling unit, while insulating the whole setup.

The main difference between this method and the divided bar model is due to different techniques used to measure the heat flux. In the divided bar technique, the heat flux is estimated by measuring the temperature gradient along a reference material, while in the heat flux transducer technique, heat flux is measured directly by using a thin heat flux transducer, as shown in Figure 3.13.

The error of this technique is reported to be around 5% and different calibrations are needed during the test [37].

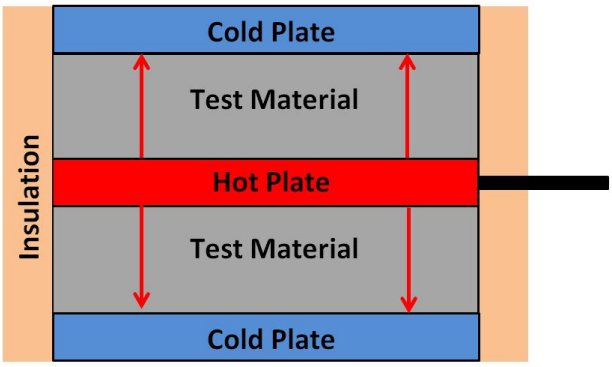


**Figure 3.14:** Schematic of hot plate method

### 3.2.3 Hot Plate Method

The *hot plate method* shown in Figure 3.14 consists of uniformly wound heaters in the center of a cylindrical cup or bowl, which is only isolated from the ends. The walls of the cylindrical tube are kept at a constant cold temperature in order to create steady state heat transfer conditions.

A number of temperature sensors are placed on all surfaces at appropriate positions from hot to cold sides and also along the heater. The DC power through the hot plate is measured and since the hot plate is fully buried inside the specimen, it can be assumed that all the DC power measured is transferred through the specimen. Based on the temperature and power read-outs, it is possible to calculate the thermal conductivity of the test specimen.

Heat flux measurement errors in this method are lower compared to the divided bar technique and heat flux transducer [37]. However, in some cases, it can be difficult to maintain a constant temperature along the heater. In addition, there is no load applied to press the specimen to the hot and cold plates and therefore, the results are subjected to errors related to the contact surface thermal conductivities.

### 3.2.4 Transient Method Using Thermal Probe

The *transient method* is one of the common techniques for measuring the thermal conductivity of porous materials. The method is based on the idea that the rate of heat transfer from a source is a function of the thermal properties of the medium.

The point contact transient technique and the hot-wire method have been used to measure the thermal conductivity, thermal diffusivity, and specific heat of solids and fluids for decades [38]. Recently, new modifications of the method, such as the *hot strip technique*,

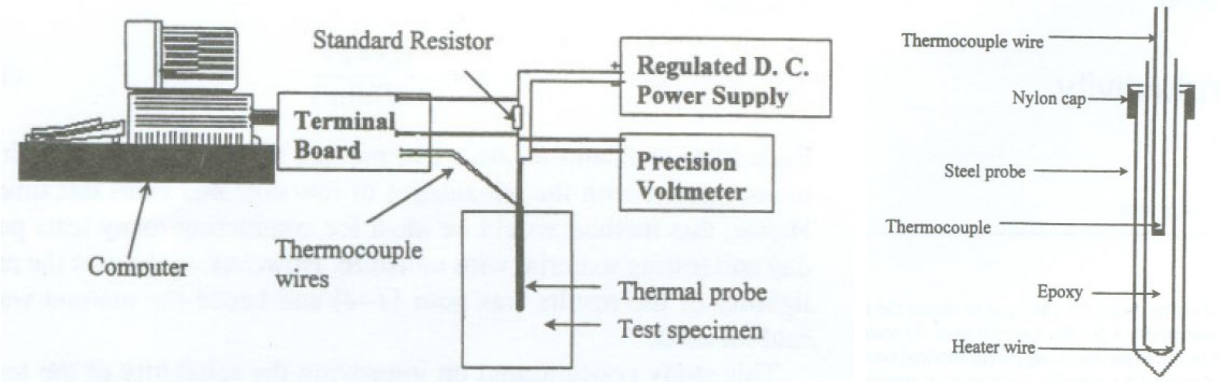


**(a)** Electrical circuit and data acquisition system **(b)** Thermal probe

**Figure 3.15:** Manohar thermal probe design and result [38]

have been developed. Work done by Manohar *et al.* [38] is a good example of the hot strip method.

Manohar *et al.* used a thermal probe consisting of an electrical heater and a thermocouple. The probe was inserted into an isothermal material and powered. Heater wire was looped and inserted into the full length of the tube to form the heating element shown in Figure 3.15. A thermocouple was inserted midway along the length of the tube to measure the temperature as a function of time. The time-temperature data from the probe were analyzed to obtain the mean apparent thermal conductivity $K$.

There are other similar techniques used for the thermal conductivity measurement of powders. One example of these techniques is the method used by Swift in 1966 [39]. Swift also used the transient method idea but with a more complicated experimental setup. The main advantages of the thermal probe method used by Manohar *et al.* compared to techniques used by others are the low cost and short test time. Therefore, this method is ideal for conducting many tests per day. However, the reliability of the results can be poor. The main uncertainty of his method raises from placement of the thermal probe. Powders can become denser closer to thermal probe when placing the probe inside the powders. Therefore, since the results are based on the powders near the thermal probe, the error for this technique can be significant.

### 3.2.5 Laser Flash Method

The *laser flash method* is a frequently used technique for measuring the thermal diffusivity or conductivity of different materials. The method is based on measuring the temperature rise on the back face of a thin disc sample caused by a short or long energy pulse.

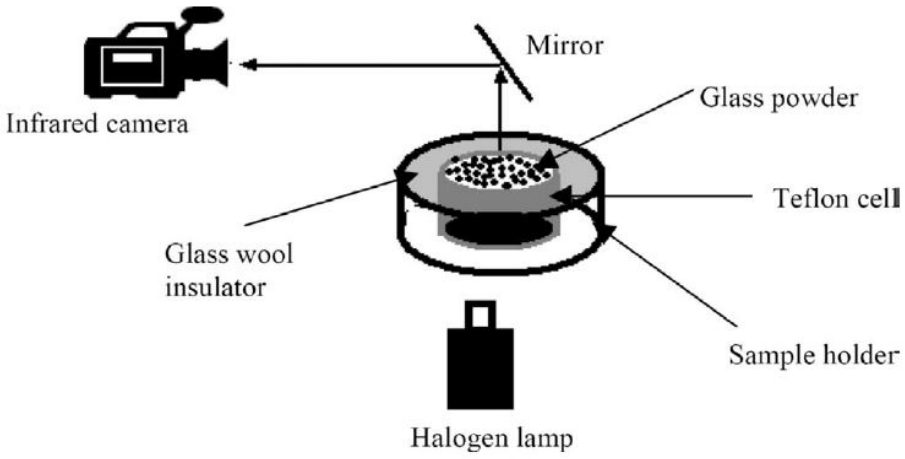


**Figure 3.16:** Schematic of the square wave heating method [40]

An example of this technique was shown by Albouchi *et al.* in 2005 [40]. Following Albouchi's method, it is possible to use an optimal experimental design of a photothermal radiometry method using a square wave heating excitation, to determine the effective thermal conductivity of powders. This type of experimental setup is shown in Figure 3.16. This setup includes a heat source, a sample, an infrared camera, and a data acquisition system. The sample is composed of a Teflon cell which is filled with a glass powder. The test specimen is placed horizontally and is heated below by a halogen lamp, which provides a uniform heat flux. A mirror reflects the flux emitted by the surface of the test specimen towards an infrared camera. This infrared camera is connected to an acquisition system to calculate the thermal conductivity based on the inputs. Some parameters in this experiment such as emissivity of the powder and the standard constants of the camera must be known for calculating the thermal conductivity of the powders.

Although the laser flash method is suggested to be an accurate model, it is mostly used for particular samples with certain dimensions.

### 3.2.6 Photothermal Methods

*Photothermal methods* are based on the generation of thermal waves. The thermal conductivity can be estimated from temperature oscillations (which are periodic in space and time) and the time dependency of the resulting thermal waves. Different techniques used for the photothermal method include:

- Photoacoustic method: A microphone in the closed gas volume is placed in front of the specimen to detect the pressure oscillations which are induced by the temperature

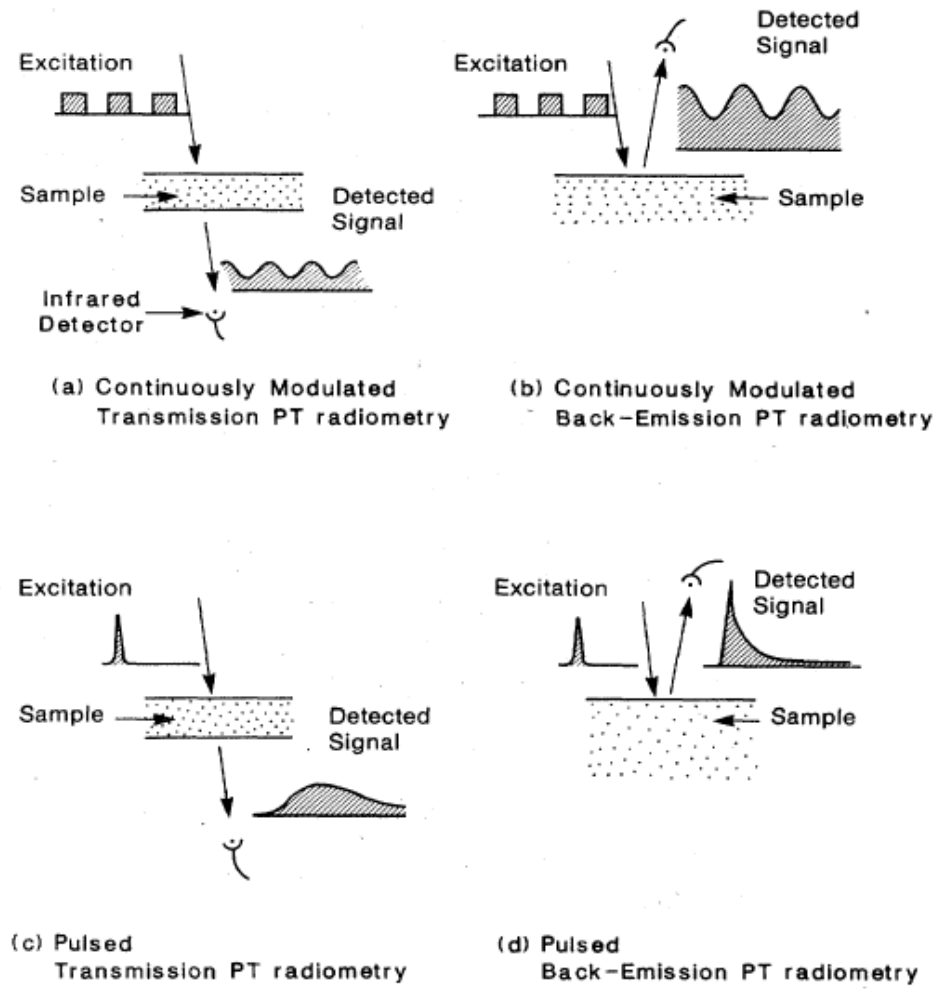


**Figure 3.17:** Variations of the photothermal radiometry techniques [41]

oscillations on the surface.

- Thermo-elastic effect: The thermally induced sound wave is captured by a piezoelectric transducer; the temperature dependence of the optical reflection are detected by a probe laser that is directed onto the surface.
- Laser beam deflection: Laser beam deflection uses a second laser beam that is periodically deflected in the temperature gradient above the surface by the interaction with the temperature oscillations.
- Photothermal radiometry: This method is based on measuring the infrared radiation emitted by the thermal waves. There are different techniques in photothermal radiometry which are well explained by Tam [41] (see Figure 3.17)

Photothermal techniques are common methods for thermal conductivity measurements of different materials. More reviews of different procedures for the photoacoustic method with details of the experimental setup can be found in publications by Tam [41], Rohde [42], and Fernelius [43].

The main disadvantage of this technique is the high cost of the experimental setup. Moreover, photothermal methods usually take the conductivity of the surface of specimen. This can increase the error when using materials with uneven density distributions, such as powders.

### 3.2.7 Comparisons of Experimental Methods

The experimental methods explained above are the general techniques for measuring the thermal conductivity of any materials regardless of the type and shape of the specimens. In most cases, we need to apply some changes to the procedure in order to use powders as our testing material.

One of the main criteria for choosing a suitable experimental method is to verify if we can use powders as our testing material. Also, the capability of powder compaction inside the experimental setup is another important factor to consider for choice of methods. Simplicity and low cost are also other criteria considered here. All the experimental methods explained in this section measure the thermal conductivity of materials with a reasonable range of error. Therefore, the precision of the method is not the main concern when choosing a suitable technique.

#### Divided bar method

The steady state divided bar technique is a very simple and inexpensive method for measuring the thermal conductivity of solid materials. With some adjustments, this method can be used for powder mixtures. Also, using this technique, it is possible to vary the compaction ratio of powders.

#### Heat flux transducer method

The heat flux transducer method is also a simple and inexpensive method. However, using a transducer can create size limitations. Moreover, it is uncertain if powder compaction is possible in the heat flux transducer method since pressing the powders can deform or damage the transducer.

### Hot plate method

It is hard to control a constant temperature along the heater for the hot plate method and different adjustments needs to be made to correct these errors. These adjustments increase the complexity of the method.

### Transient method

By using a thermal probe in the transient method, powders become denser closer to the thermal probe when placing the thermal probe inside the powders. Since the recorded data in this model are based on the powders closer to the thermal probe, the results may be inaccurate for calculating the average thermal conductivity of powders.

### Laser flash method

The laser flash method is not a desirable method for our problem since it is very hard to change the density ratio of the powders in this setup.

### Photothermal methods

Finally, photothermal methods are reported to be accurate tests for the thermal conductivity measurements. Also, these methods are capable of using powders and varying the density. Photothermal methods, however, are relatively expensive. In addition, these methods usually take the conductivity of the surface of specimen, while other experimental methods, such as the divided bar technique and the hot plate method, measure the average thermal conductivity of the powders.

In conclusion, based on the criteria mentioned earlier, the divided bar technique is a suitable, simple, and inexpensive method for measuring the average thermal conductivity of powders.

# Chapter 4

# Experimental setup

In this chapter, the experimental setup is provided for conducting heat conductivity and flame speed measurements in the powder compacts. The results are provided in Chapter 5. Chapter 4 is organized as follows: The description of the raw powders and the milling technique for refining the powder is presented in section 4.1. The thermal conductivity measurements are presented in section 4.2. Finally, the technique to measure the flame speed in the powder compacts is given in section 4.3.

## 4.1 Powder Types and Production Methods

Two different structures of Al-Ni powders are used in this thesis: *Normal aluminum nickel powders* and *ball milled aluminum nickel powders*, which are discussed in Sections 4.1.1 and 4.1.2, respectively.

### 4.1.1 Normal (Non-milled) Al-Ni Powders

The raw materials used in the experiments were high purity (99.9%) spherical powders purchased from Atlantic Engineer Equipment (NJ, USA). The particles had micron-size distributions with average diameters of $d_{Al}$ =4.2 $\mu$m and $d_{Ni}$ =6.8 $\mu$m. The microstructure of samples was observed by using scanning electron microscopy (EVO MA-10, Carl Zeiss NTS GmbH, Germany), equipped with a backscattered electron (BSE) detector and an energy dispersive spectrometer (EDS) probe (INCA-x-act, Oxford Instrument, UK). The microstructures of the aluminum and nickel powders, using the SEM technique, are shown in Figure 4.1.

Table 4.1 summarizes the main chemical and mechanical properties of these two pow-

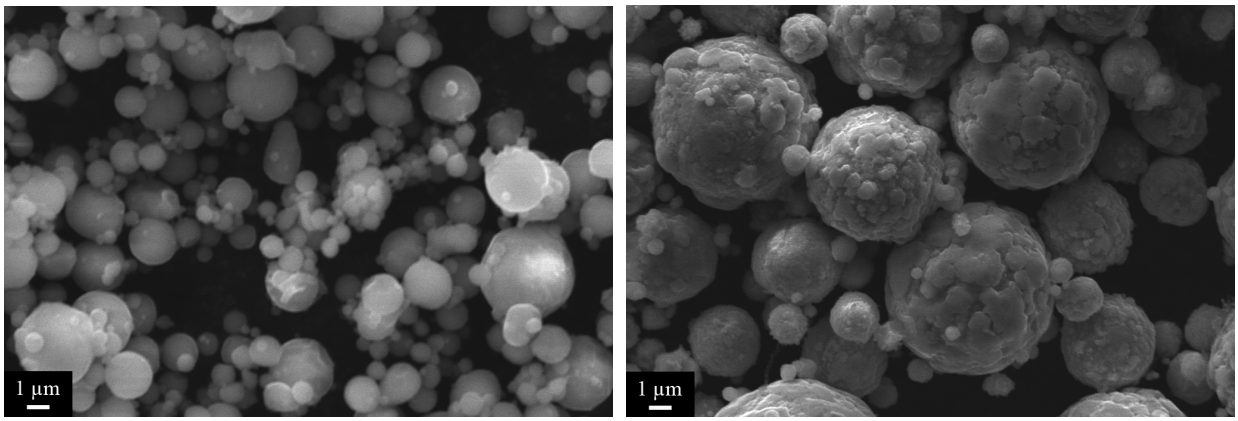


**(a)** Aluminum Powders **(b)** Nickel Powders

**Figure 4.1:** Microscopic photographs of the nickel and aluminum powders [9]

**Table 4.1:** Aluminum and nickel properties

| Property | Aluminum | Nickel |
|---|---|---|
| 1- Atomic number | 13 | 28 |
| 2- Atomic mass $W$ | 26.98 g/mol | 58.71 g/mol |
| 3- Density | 2700 kg/m$^3$ | 8900 kg/m$^3$ |
| 4- Melting point | 660.4 $^o$C | 1453 $^o$C |
| 5- Young's modulus | 70 GPa | 200 GPa |
| 6- Poisson ratio | 0.35 | 0.31 |
| 7- Thermal Conductivity | 237 W/(m·K) | 91 W/(m·K) |

ders used in the experiments.

The powder composition used in the present study is a 1:1 atomic ratio of nickel and aluminum. This same composition was used by Bacciochini *et al.* at high densities [9], which are the results we wish to compare with. Referring to the phase diagram for Ni-Al shown in Figure 4.2, a 50% atomic ratio of nickel with aluminum results in the highest possible melting temperature, corresponding to a 1:1 Al-Ni molar ratio.

An accurate control of the composition of the powders was achieved with a digital scale accurate to 0.001 grams. According to the atomic masses of aluminum and nickel from Table 4.1, in order to create 100 grams of a 1:1 Ni-Al molar ratio mixture, approximately 31.6 grams of aluminum and 68.4 grams of nickel powders were mixed together.

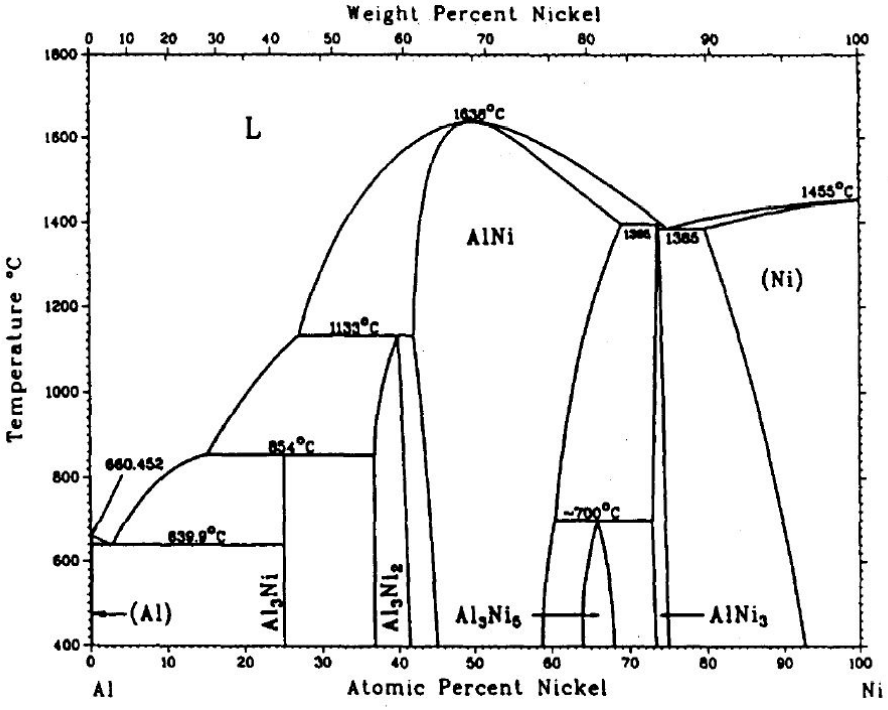


**Figure 4.2:** Ni-Al phase diagram [44]

### 4.1.2 Ball-Milled Al-Ni Powders

Milled powders of Ni and Al were also used in the present study in order to compare with the results of Bacciochini *et al.* [9]. Arrested Reactive Milling (ARM) is a form of mechanical alloying in which two or more reactive powders are milled using a ball mill machine. Nanocomposite powders can be formed through the ARM process [45]. Typically the milled powders are metals with one powder that is harder than the other. The harder powder breaks up and gets embedded inside a matrix of the softer powder. Further information on the ball milling technique can be found in Dreizin's review article [45].

The ball milling technique used follows the procedure used by Bacciochini *et al.* [9]. Ball milled powders used in our experiments were produced by mixing normal aluminum and nickel powders with a 1:1 molar ratio. A planetary milling machine (Fritsch Pulverisette 7) was used to refine the structure of inter-metallic mixtures in an inert argon atmosphere and without any milling agent. The milling was performed using two cylindrical bowls containing 10 mm diameter hardened steel balls with a ball-to-powder mass ratio of 20:1, so each basket can hold up to 10 grams of powders (30 balls in each basket). hardened steel balls were chosen to make sure that the balls would not break and be mixed

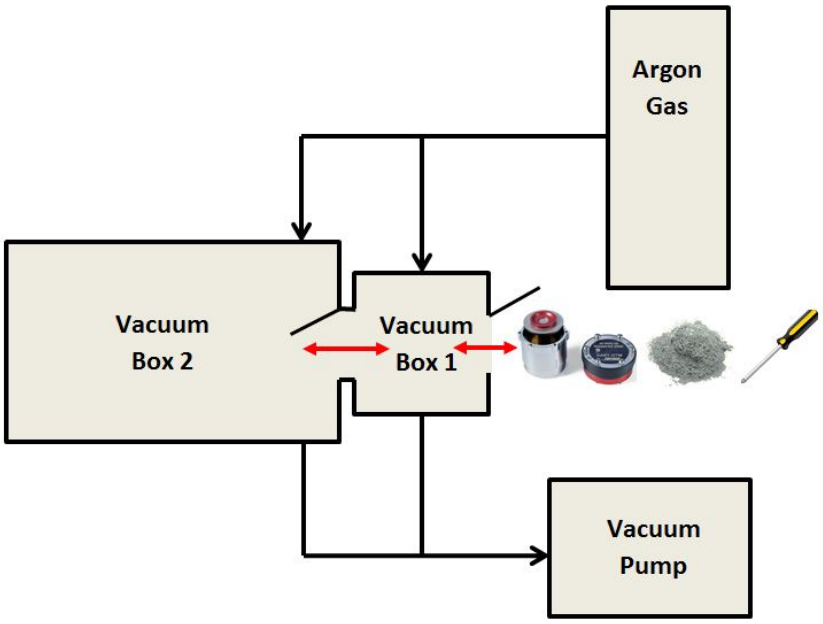


**Figure 4.3:** Schematic of vacuuming the bowls for milling machine

with the powders.

The bowls were loaded in an inert argon atmosphere inside of a glove box in order to avoid powder oxidation during milling. Following the schematic in Figure 4.3, the bowls and powders were placed in box 1 and both box 1 and 2 were closed, evacuated, and filled with argon gas. Then, the gate between two boxes was opened and bowls and other equipment were placed inside box 2. In some cases, the second box was evacuated and filled with argon gas multiple times in order to create an environment with less than 4% oxygen (measured using an oxygen sensor). After reaching the desired oxygen percentage, the bowl caps were fastened tightly enough to prevent any leak of air.

Next, bowls were placed in the milling machine for 52 minutes. The metal plate containing the bowls rotates planetary with milling speed of 600 rpm and the rotation direction was reversed every two minutes to prevent overheating and limit material adhesion to the bowl walls. The given time to the machine was set from the records of gas pressure and temperature to get the powder microstructure appropriate for SHS process, while preventing any reaction during the milling process.

Finally, powders were emptied from the bowls. In most cases, about 20% to 30% of powders were stuck on the balls and inner walls of the bowls, therefore, approximately 8 grams (or less) of milled-powders could be produced from each bowl.

After powders were removed, the bowls and the balls were cleaned using ethanol. Ethanol was poured inside the bowls with the balls. Then the bowls were placed in the

**(a)** Machined caps **(b)** Machined semi-caps

**Figure 4.4:** Machined caps and semi-caps for replacing original caps in the milling machine

milling machine for about 26 minutes (milling speed of 600 rpm) to ensure all the powders were washed off from the baskets, caps, and the balls. Finally, the bowls and balls were washed with water and dried after.

The original bowl caps contained different sensors, which were not particularly useful for our milling process, and repeating the milling process constantly could damage these caps and sensors. In order to avoid these damages, two new caps were machined with similar sizes and weight to replace the original caps (Figure 4.4a). Also, there was a semi-cap behind each main cap, which was in direct contact with the bowls and powders. These semi-caps cracked during the tests and new semi-caps with similar sizes and weight were machined and replaced.

The total time for each trial is estimated to be around 140 minutes, which includes filling the bowls, running the machine, removing the milled powders, and washing the bowls.

The scanning electron micrographs of the milled powders are shown in Figure 4.5. It is noticeable that the ball milled powders are larger compared to normal powders (Figure 4.5a). However, the ball-milled powder is a composite of aluminum and nickel nano-scale lamellas (Figure 4.5b). The characteristic dimension of the largest lamellas was approximately half a micron.

## 4.2 Thermal Conductivity Measurement

The conductivity of powders was measured using the *steady state divided bar technique* outlined in the previous chapter with the assumption that thermal conductivity of the experiment is independent of the temperature. The schematic of Figure 4.6 illustrates the

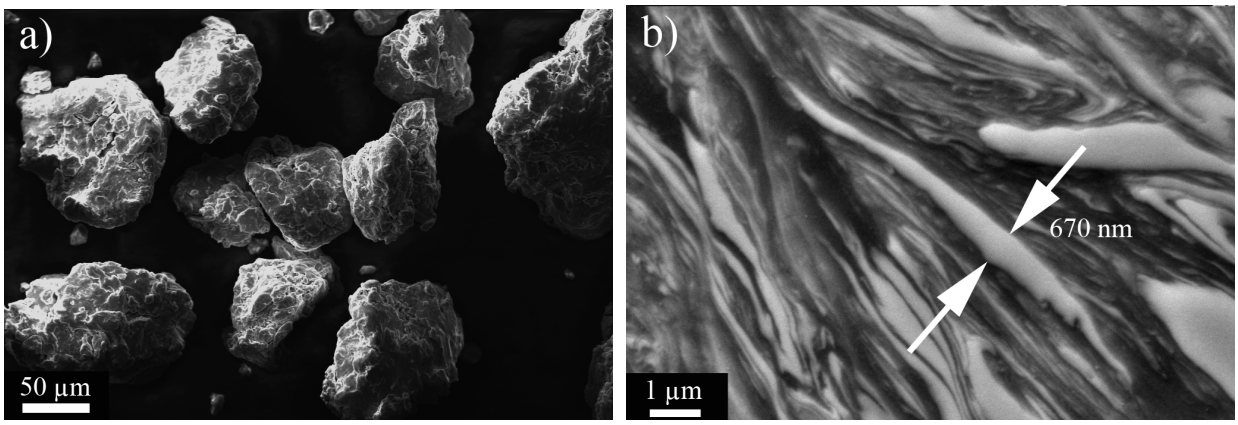


**(a)** View of milled powders in micro-scale **(b)** Zoom in view of one milled powder particle

**Figure 4.5:** Scanning electron micrograph of the structure of the Al-Ni ball-milled powders; lighter lamelar strand is the deformed Nickel [9]

technique. Powders were placed in between two carbon steel 1018 cylindrical rods, with 1.5 inch diameter (38 mm), purchased from Mcmaster-Carr. A temperature gradient was created by using four rectangular "Ultra-Thin Polyimide Heat Films" (25.4 mm by 25.4 mm) on one side and ice cubes on the opposite side creating 70 ·K to 90 ·K temperate gradient. The variation of the thermal conductivity of the rods and the samples is reasonably assumed to be negligible for this temperature range. The system was insulated using multiple layers of fiberglass (4 cm thickness total) to ensure all the heat was transferred through the rods. The insulation was verified to be adequate since the outer surface temperature of the insulators was almost at the room temperature meaning that the heat transfer through the insulator is negligible.

The main difficulty of the design was to keep the powders in place while compacting the powders inside the rods. Based on these requirements, a thin cylindrical wall was designed to hold the powders. The detail of the design is shown in Figure 4.8. A 1 mm thick wall was attached to the top of the lower cylindrical steel rod. The higher steel rod contained a compactor section which fitted inside the wall. The compactor section was designed to compact the powders to different density ratios.

Five adhesive-backed type K thermocouple probes, purchased from McMaster-Carr, were attached on the outer surface of the rods to constantly capture the temperature along the rods and the thin wall. The thermocouples were glued at the top and bottom of higher rod, lower rod, and outer surface of the wall.

By measuring the temperature gradient along the cylinder and knowing the conductivity of carbon steel 1018, we could approximate the heat flux passing through the cylinder.

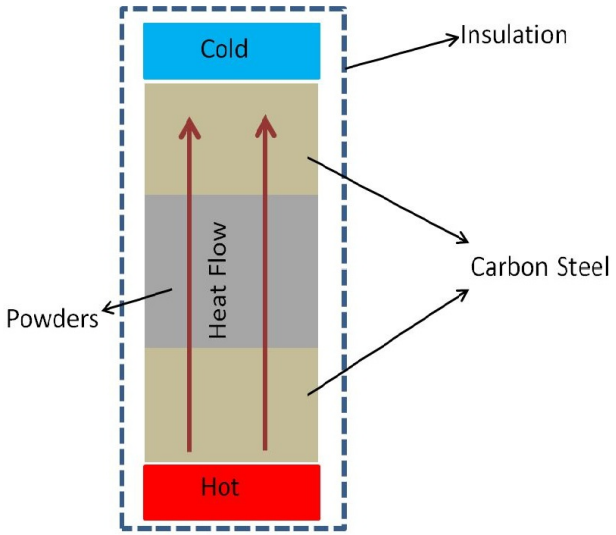


**Figure 4.6:** Divided bar heat conductivity measurement

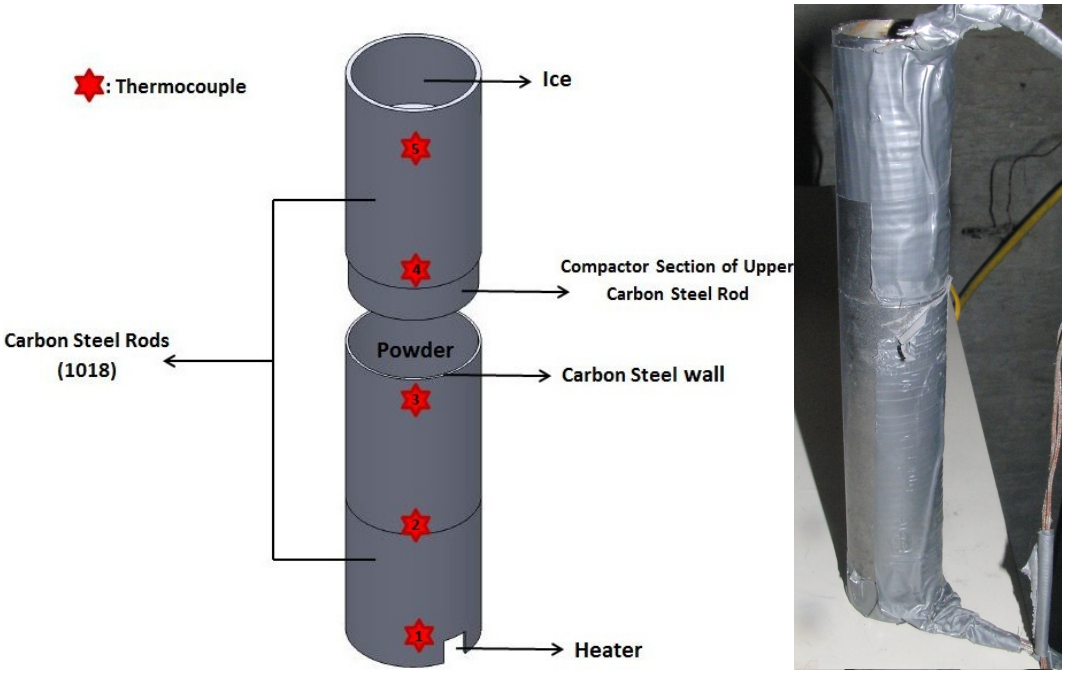


**Figure 4.7:** Carbon steel rod used for the steady state divided bar technique

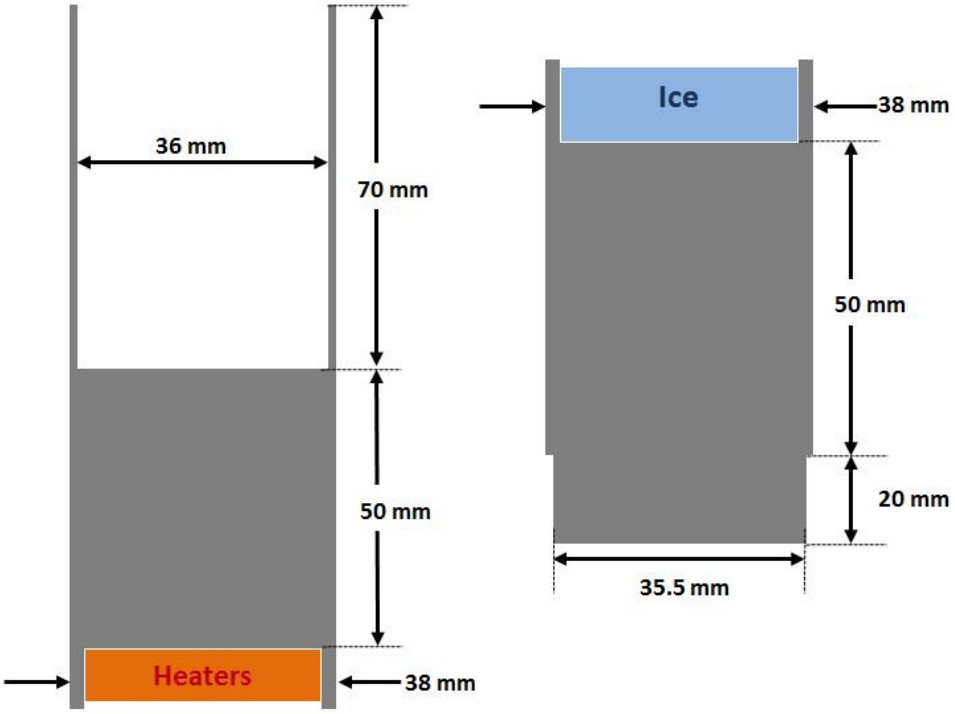


**(a)** Lower rod **(b)** Upper rod

**Figure 4.8:** Dimensions of the rods in the divided bar experiment

Using the approximated heat flux and by measuring the temperature gradient along the powders, the conductivity of powders could then be estimated.

However, using the steel wall can increase the complexity of the heat transfer analysis. Since the walls are very thin compared to the diameter of the rods, the first assumption was to neglect the transfer of heat between the wall and the powders. As a result, the model can be simplified to a one dimensional heat transfer model shown in Figure 4.9. To verify this assumption, the experiment was modeled in the finite element thermal analysis package provided by ANSYS.

### Numerical ANSYS model

In order to verify the one dimensional assumption, a numerical model was created using ANSYS with an identical situation as our experimental setup. A three dimensional model was used in ANSYS, and therefore the heat transfer between the walls and powders were also considered. Comparing the numerical results from ANSYS with the 1-D analytical model shown in Figure 4.9, it was possible to validate the assumption used in our experiments.

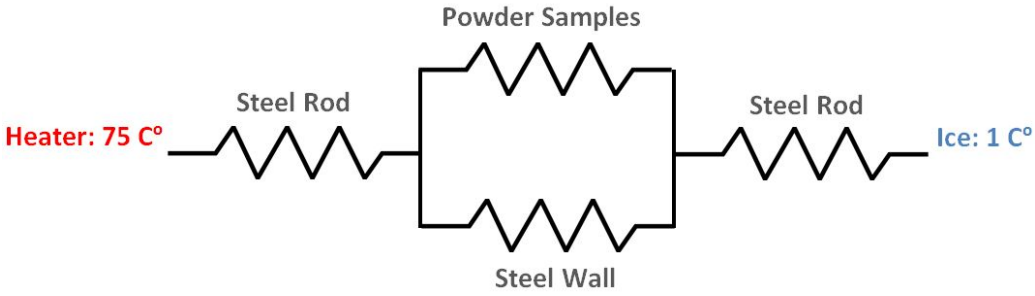


**Figure 4.9:** 1-D assumption for calculating the thermal conductivity of powders in the divided bar technique

The *3-D solid heat transfer method* was used for the ANSYS model. Following the experimental setup, 4 parts were created, shown in Figure 4.10. Bottom, top, and thin walls were from the same material (thermal conductivity of 100 W/(m·K)). A cylindrical block, which represents the powders, had a lower thermal conductivity of 5 W/(m·K). The inner cylinder (powder) was attached to the thin wall and the other two rods. All the dimensions were identical to the experiment in order to have a similar scenario as our experimental setup.

The *triangle meshing model* was used through automatic mesh sizing, with smaller meshes in the middle, as shown in Figure 4.12, in order to capture a more accurate heat transfer between the wall and the powders.

The boundary conditions were almost identical to the experimental setup (no heat losses). The temperatures of the bottom surface of the lower cylinder and the top surface of the higher cylinder (90 $^o$C and 0 $^o$C respectively) were other inputs to the model. The analysis was set to the steady state condition and the results were plotted.

Using the calculated heat flux from ANSYS and the temperature gradient along the middle cylinder (powders), we then used the 1-D analytical heat transfer model to estimate the thermal conductivity of powders $K_{1D}$. Finally by comparing this thermal conductivity with the input thermal conductivity of powders in ANSYS (5 W/(m·K)) $K_{3D}$, we could verify the acceptance of the 1-D model using the error definition:

$$e = \frac{K_{3D} - K_{1D}}{K_{3D}} \tag{4.1}$$

Doing so, it was shown that the 1-D model had an error of 4.5% for measuring the thermal conductivity, which is acceptable for our purposes. Therefore, the 1-D model was validated for modeling the thermal conductivity of Al-Ni powders with our experimental setup.

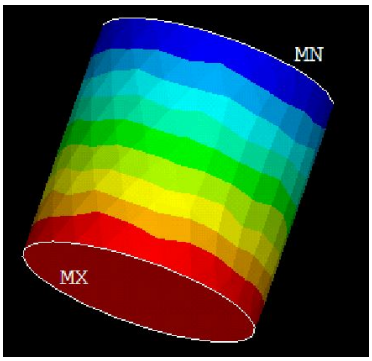


**(a)** Top cylinder

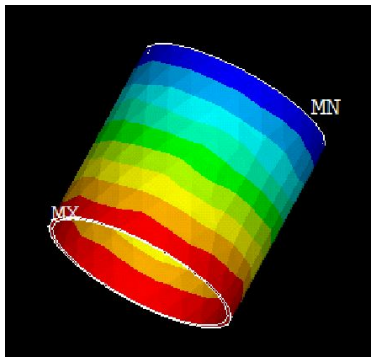


**(b)** Thin walls

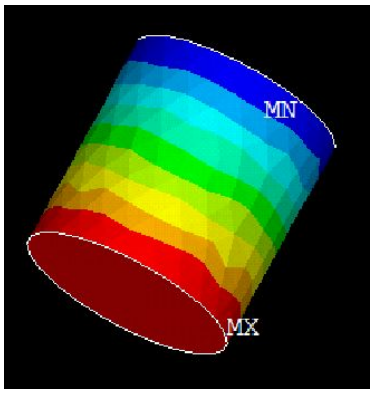


**(c)** Cylindrical powders

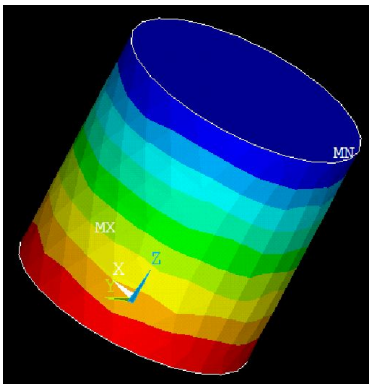


**(d)** Bottom cylinder

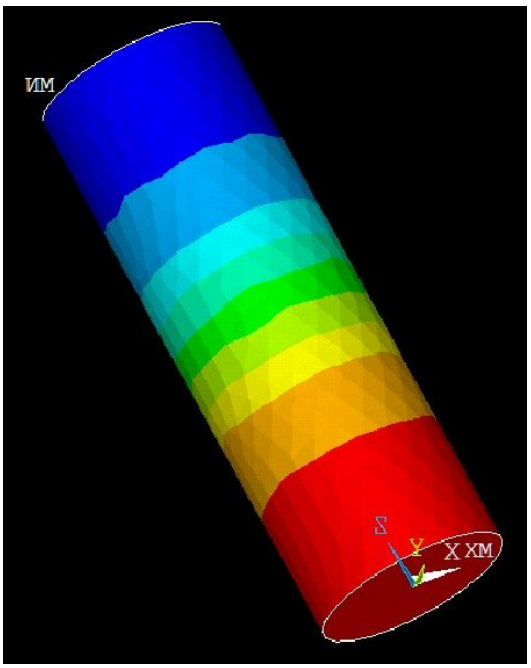


**(e)** Complete view of the model

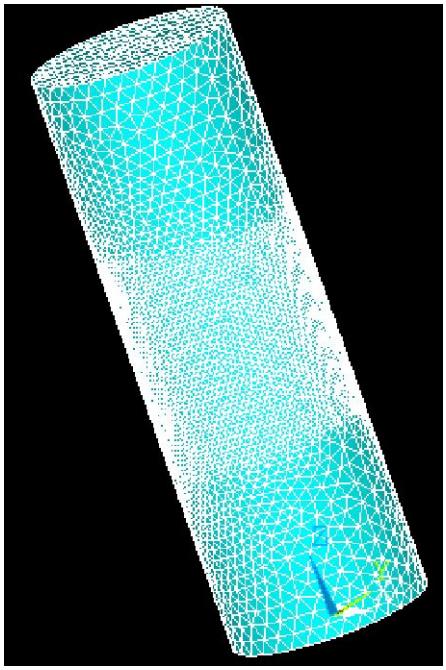

**(f)** Mesh sizes

**Figure 4.10:** Ansys model, parts, and meshing

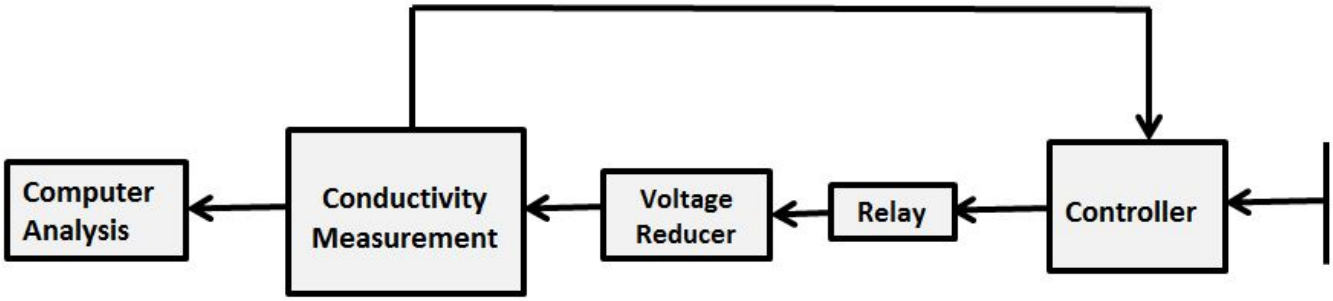


**Figure 4.11:** Conductivity setup

### Controlling the temperature

Another difficulty in the experimental setup was for temperature control along the top and bottom surfaces. A mixture of ice and water was used as the cold side, so the temperature is always set to the melting temperature of the ice. The temperature of the heaters at the bottom, however, could vary depending on the materials attached to the heaters. In order to control the temperature of the heaters, a temperature controller, shown in Figure 4.12e, was used. A "T type" thermocouple was attached to the heaters and the signals from the thermocouple were sent to the controller. Depending on the temperature of the heaters, the controller could allow or stop the current to pass to a voltage reducer. The voltage reducer, shown in Figure 4.12c, was used to reduce the 110 V to 28 V, which is the maximum allowable voltage for the heaters. Figure 4.11 illustrates the experimental setup of the conductivity measurement.

### Steady state condition

It was also important to verify the steady state condition in this experiment. To do so, the temperature read-out from each thermocouple was measured every second, allowing for the fluctuations to be analysed (discussed in Chapter 5). The steady state region was set to the point where the temperature variation was less than 0.3 $^{o}$C over 10 minutes for all thermocouples. In most cases, the steady state region appeared 60 to 100 minutes after starting the experiment. The total time for each trial was roughly estimated to take 120 minutes, which included compacting the powders, and running the test.

**(a)** Computer analysis using Labview

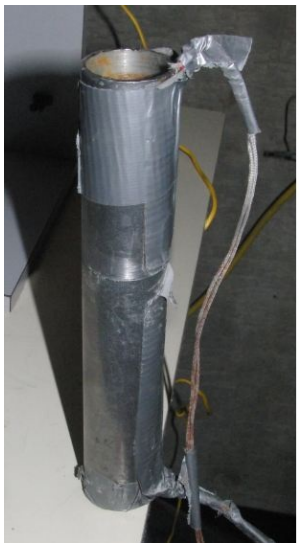

**(b)** Cylinders and Thermocouples


**(c)** Voltage reducer


**(d)** Relay


**(e)** Controller

**Figure 4.12:** Different parts of the thermal conductivity test

### Temperature Readout

An example of the readout of the various thermocouples used in the experiments is shown in Figure 4.13. The sudden jumps and high fluctuations of the lowest temperature (close to

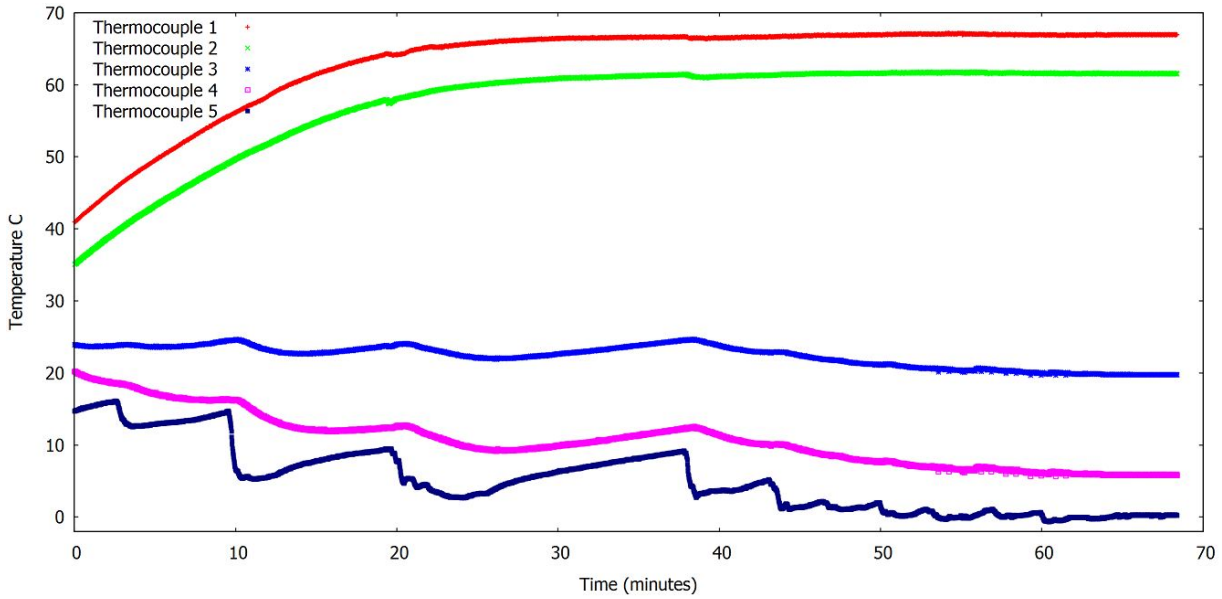


**Figure 4.13:** Temperature readout of thermocouples as a function of time (from initial condition up to the steady state region)

the ice bath) were caused by replacing the water (from the melted ice) with new ice cubes. This variation disappears as we get closer to the steady state region. For this trial, it is clear that after about 65 minutes, the temperature stays constant for all thermocouples (with less than 0.3 $^{o}$C variance over 10 minutes), meaning that the steady state condition was achieved. Depending on the type and the compaction ratio of the mixture, the time required for reaching the steady state condition varied from 60 to 90 minutes.

Knowing the temperature difference and the thermal conductivity of carbon steel rod, the heat flux passing through the powders could be calculated using a simple heat transfer analysis. The heat flux ($q$) passing through the bottom rod is:

$$q = \frac{\Delta T_{rod}}{R_{rod}} \qquad R_{rod} = \frac{h_{rod}}{K_{rod} A_{rod}} \qquad A_{rod} = A_{powders} + A_{wall} \tag{4.2}$$

By assuming a fully insulated system, $q$ is equal to the heat flux passing through the second level (powders and the steel wall):

$$q = \frac{\Delta T_{powders}}{R_{eq}} \qquad R_{eq} = \frac{R_{wall} R_{powders}}{R_{wall} + R_{powders}} \qquad R_{powders} = \frac{h_{powders}}{K_{powders} A_{rod}} \tag{4.3}$$

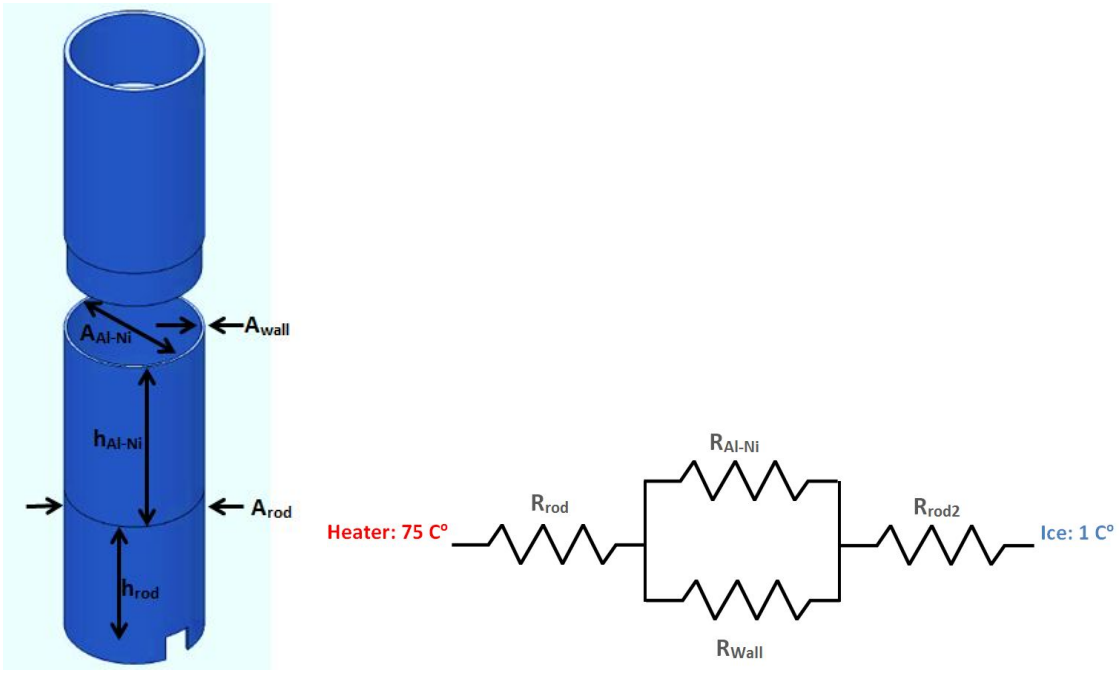


**(a)** Areas and heights **(b)** Thermal Resistant

**Figure 4.14:** Heat transfer model for the thermal conductivity measurement

where $R$, $A$, $h$, $\Delta T$, and $K$ are the thermal resistance, area, height, temperature gradient, and thermal conductivity of each section. The subscripts $rod$, $wall$, and $powders$ represent the information about the carbon-steel rod, side carbon-steel wall, and Al-Ni powders respectively. Therefore, the thermal conductivity of powders $K_{powders}$ is:

$$K_{powders} = \frac{h_{powders}}{A_{powders}} \left( \frac{\Delta T_{rod} K_{rod} A_{rod}}{h_{rod} \Delta T_{powders}} - \frac{A_{wall} K_{rod}}{h_{powders}} \right) \tag{4.4}$$

Equation 4.4 illustrates a simple case when the temperature gradient of the powders and the rods are known. The thermal conductivity circuit used for calculating the results follows the same idea, as shown in Figure 4.14b, with more details to gather precise results.

## 4.3 Flame Speed Measurement

The main part of the experiments in this thesis are focused on the flame speed measurements. Rectangular channels and metal tubes were used to measure the flame speed. The procedures are explained in this section.

### 4.3.1 Rectangular Channel Experiment

As shown in Figure 4.15, rectangular steel channels contain male and female sides. Powders were placed in the female part and using the male part, the powders were compacted. Different techniques were used to vary the force applied to the powders. By hand pressing the powders, using a hammer, or with a press, we could vary the density ratio from 35% to 60%. In order to compact the powders to higher density ratios, we had to deform the powders. Al-Ni mixtures were pressed and deformed using a hydraulic press. This permitted us to reach densities of 83% TMD.

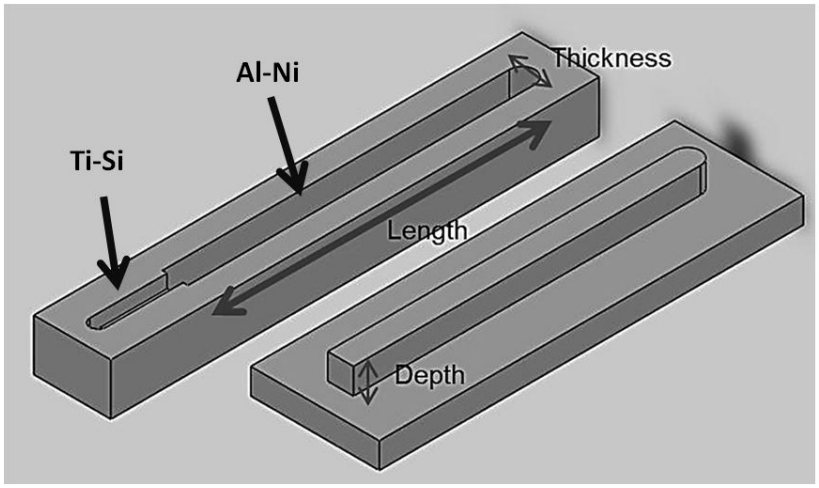


**Figure 4.15:** Channel (thickness=0.5cm)

A mixture of Titanium and Silicon powders (Ti-Si) with an atomic ratio of 5:3 was used to ignite the Al-Ni powders. Ti-Si is an SHS material with lower ignition energy and its reaction releases enough energy to ignite Al-Ni powders. The Ti-Si powders were placed near the end of the channel, and were ignited with a small butane torch. As can be seen in Figure 4.15, the channel was designed narrower at the start of the channel for placing the Ti-Si powders, so it is possible to distinguish the Ti-Si from Al-Ni powders in the recordings.

Powders were packed in the channel and the channel was then placed under a high speed camera (Casio EX-F1 capable of recording videos at 1200fps). The camera was set to $f/10.8$ with a shutter speed of 1/40000 s and was placed approximately 1.5 m above the sample. The focal length of the lens of the camera was such that the channel filled the frame in order to maximize the resolution. Figure 4.16 shows the camera setup over a sample during an experiment.

The sequential frames of the high speed videos were then extracted using “Quick Time


**Figure 4.16:** Camera setup for filming the reaction of powders

Player". The image analysis was performed using "Paint Shop Pro 8", from which we extracted the distances traveled by the flame at different time intervals. A linear regression of the time and distance traveled by the flame provided us the average flame speed.

In some experiments, the channel was covered by a glass plate, in order to eliminate the possibility of incandescent powders randomly jumping ahead of the reaction zone and thus influencing the flame speed measurements.

### Heat loss effects

Since the adiabatic flame speed predicted by Makino's model needs to be verified with the experimental results, it is important to rule out possible heat loss effects that would invalidate such a comparison. Based on a simple heat loss analysis, the heat transfer from powders to the walls is proportional to the ratio of surface area exposed to losses over the total volume of powders. From these simple arguments, one would expect that the losses would become negligible in sufficiently large cross-section channels. Channels with different cross sectional areas were hence used with the dimensions shown in Table 4.2.

**Table 4.2:** Channel sizes

| Thickness (cm) | Depth (cm) | Length (cm) |
|---|---|---|
| 0.1 | 0.2 | 8 |
| 0.25 | 0.25 | 7 |
| 0.5 | 0.5 | 7 |
| 0.75 | 0.75 | 7 |
| 1 | 1 | 7 |

**Measurement errors**

The main error in the flame speed measurement arises from determining the exact location of the flame. As shown in Figure 4.17, the flame is often not planar. The image spatial resolution also gives rise to an uncertainty. However, the non-planarity of the flame was found more important than the spatial resolution of the image. The resulting flame speed error was hence estimated from a quantitative estimate of the flame location uncertainty and the typical length used to obtain the speed. Figure 4.18 shows the method we used to estimate the errors in the flame speed measurements. The approximated flame speed is:

$$u = \frac{(X_2 \pm \frac{L_{flame}}{2}) - (X_1 \pm \frac{L_{flame}}{2})}{t} = \frac{(X_2 - X_1) \pm L_{flame}}{t} = \frac{\Delta X \pm L_{flame}}{t} \tag{4.5}$$

where $X_1$ and $X_2$ are the two measured positions of the flame and $L_{flame}$ is the confidence interval for the position of the flame (length of the red block in Figure 4.18. Therefore, for the error $e$, we get:

$$e = \frac{u_{actual} - u_{approx}}{u_{actual}} = \frac{\left(\frac{\Delta X \pm L_{flame}}{t}\right) - \left(\frac{\Delta X}{t}\right)}{\frac{\Delta X}{t}} = \frac{\pm L_{flame}}{\Delta X} \tag{4.6}$$

From the experiments, the confidence interval for locating the flame $L_{flame}$ is approximately 3 mm, while the distance traveled by the flame between the first and last frames analyzed is typically 6 cm. This yields a flame speed uncertainty of approximately 5%.

### 4.3.2 Tube Experiments

A secondary method for measuring the flame speed as a function of density ratio was to use tubes instead of metal channels. The main advantage for replacing channels with metal

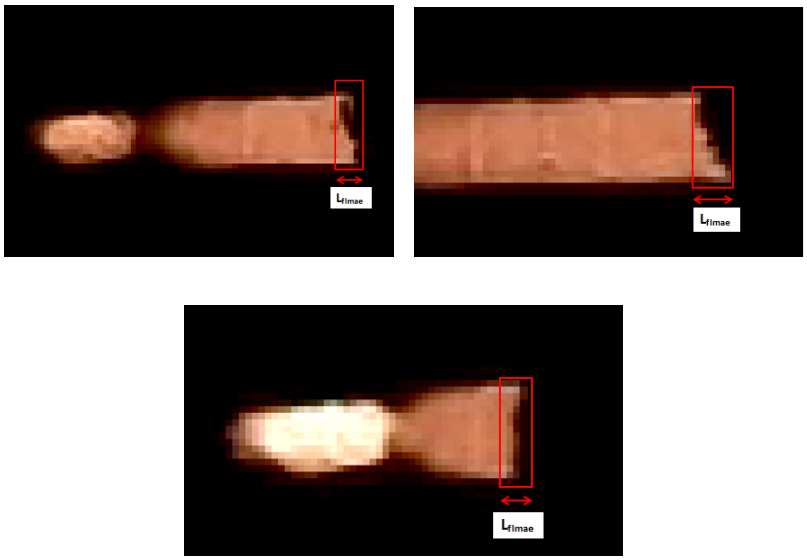


**Figure 4.17:** Front flame in channels and the error range for determining the exact position of the flame

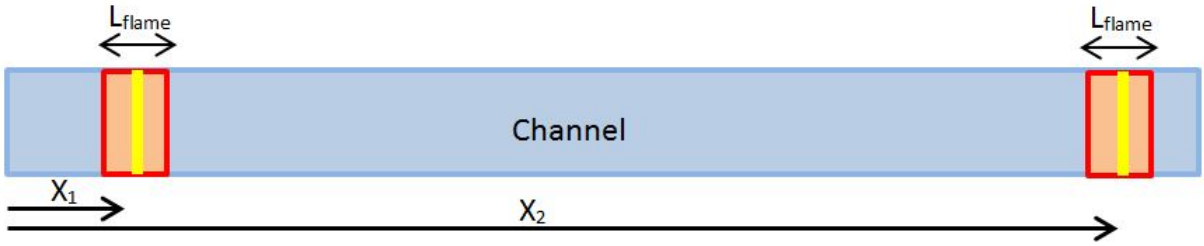


**Figure 4.18:** Schematic of the flame speed error calculation

tubes is to create a more even density distribution for the compressed powders. Metal channels have rectangular cross-sections and this created an uneven pressure distribution and consequently, an uneven density ratio in each cross section was created. Moreover, compacting the powders only from the top of channels created a higher density ratio closer to the bottom of the channel.

The tubes were 304 stainless steel welded and drawn tubing purchased from McMaster-Carr. Similar to the channels, tubes with different diameters (2.67 mm, 3.45 mm, 4.25 mm, and 5.05 mm) were used in order to study the heat loss effects. All tubes were purchased with the same wall thickness size (1 mm) and were cut into the same length (6" or 15.25 mm). After smoothing the sides, the bottom of the tubes was closed using duct tape.

Also, different rods with diameters slightly smaller than the inner diameters of the

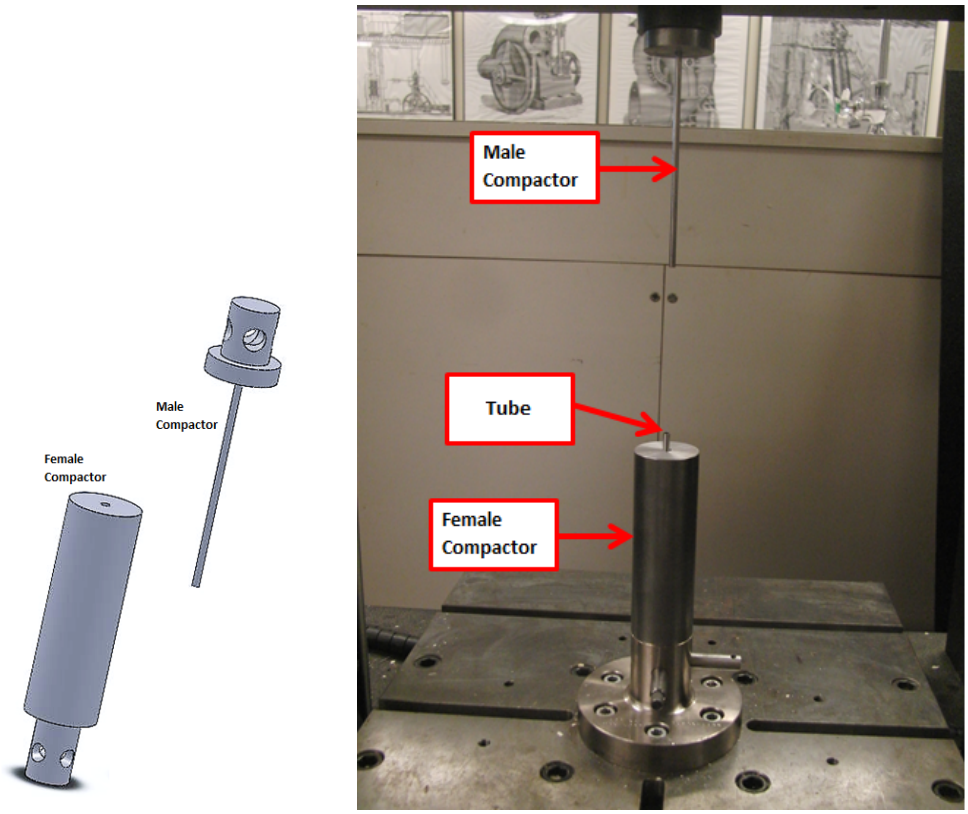


**Figure 4.19:** Tube compactor and Instron Machine

tubes were purchased to compact the powders inside the tubes. Al-Ni powders were poured in the tube and after filling the tube for about 3 mm, the powders were compacted using the rod. This procedure was continued until the tube was approximately 95% full. The top 5% of the tube (5 mm to 7 mm) was filled with Ti-Si powders to start the ignition.

Using the Instron machine, the mixture was compacted to higher densities. The compactor, shown in Figure 4.19, consists of female and male parts to apply compaction to powders. Both sides were connected to the Instron machine. The tube containing powders was placed inside the female part. The male part, which has a diameter slightly smaller than inner diameter of the tube, pressed the powders inside the tube. After applying the first compaction, the tube was removed from the compactor and more powders were added and another compaction was applied. This procedure continued until the tube was 95% full with powders. The compaction was applied at different levels in order to create an even density distribution over the length of the cylinder.

Two different procedures were used for measuring the flame speed inside the tube. The initial assumption was that the light of the flame is not very visible from outside of the tube and recording the combustion for finding the flame speed would not be accurate.

**Figure 4.20:** Filled tube and the holder before ignition

Therefore, the first technique to measure the flame speed was using thermocouples placed on the outer surface of the tube.

Adhesive-backed type K thermocouple probes from McMaster-Carr were purchased for this purpose. Three thermocouples were placed along each tube at equal spacing. Signals from the thermocouples were processed with the "Labview" program. A simple circuit in Labview was designed to capture temperature of all thermocouples as a function of time. During the reaction, the highest temperature corresponded to the flame. Therefore, by taking the time difference at the highest temperature points between thermocouples, the flame speed could be calculated.

However, after the first test, the adhesive, plastics, and wires attached to the thermocouples burnt. Using the surface thermocouples was shown to be unsatisfactory and the results were not reliable since thermocouples were loosened and slightly moved during the experiment.

However, it was observed that the flame is visible and clear enough from outer surface of the tubes, and therefore, we could the flame could be recorded. As a result, a similar technique, which was used in the channel experiments for recording the flame, was also performed for the tube experiments.

Due to the thickness of the tubes, there exists a delay between the moment that the flame is arisen at a given location and the time the light is emitted from outer surface of the tube. However, this delay is the same at all the locations along the tube length, hence it does not effect the calculation of the flame speed.

The tube was placed vertically on a holder, shown in Figure 4.20, and the powders were ignited. The flame speed was recorded using the high speed camera, as described

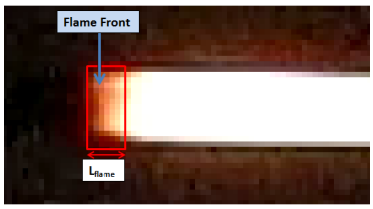


**Figure 4.21:** The flame seen from outer surface of the tube and the error range for determining the exact position of the flame

above.

#### Measurement errors

Similar to rectangular channels, the uncertainty in locating the flame in each frame leads to systematic uncertainties in the flame speed. Using the same error measurement model as in for channels, the error is estimated to be less than 2%. The error is lower than in the channel experiments because the tube length is approximately two times longer than the channel length.

### 4.3.3 Safety Concerns

For preparing the powders, Ultrasoft Cartridge Respirators purchased from McMaster (with P100 Filter) were used to prevent inhaling the powders. Combustion of SHS materials also creates a very high temperature and a bright flame. Therefore, it was required to use gloves and protective fire-proof clothing to prevent any eventual skin burning, as well as welding goggles for eye protection.

# Chapter 5

# Results and Analysis

This chapter is divided into two sections. The first section summarizes the results obtained for the flame speeds and heat conductivities. In the second section, the flame speed measurements are compared with predictions made using Makino's model.

## 5.1 Results of the flame speed and conductivities measurements

The results presented in this section are categorized into three sub-sections. The results of the flame speed measurements performed in channels are given in Section 5.1.1. The flame speeds obtained in tubes are given in Section 5.1.2. Section 5.1.3 provides the results of the thermal conductivity measurements and comparison with models.

### 5.1.1 Flame Speed in Channels

The flame propagation of milled and non-milled powders are shown in Figure 5.1. Figure 5.1a shows a stable flame propagation in non-milled Al-Ni powders. In vivid contrast, the ball-milled system shown in Figure 5.1b exhibits localized bursts of the powders, partially ejecting them out of the channel. The ejection can also be seen in Figure 5.2, which shows the milled powders after the reaction. The reason for such behavior is still not clear [46].

Compacted powders over approximately a 60% density ratio, which corresponds to the onset of severe plastic deformation during the compaction, also exhibited more stable flames. This is consistent with limited mobility of the powders due to a stronger contact between the deformed powders.

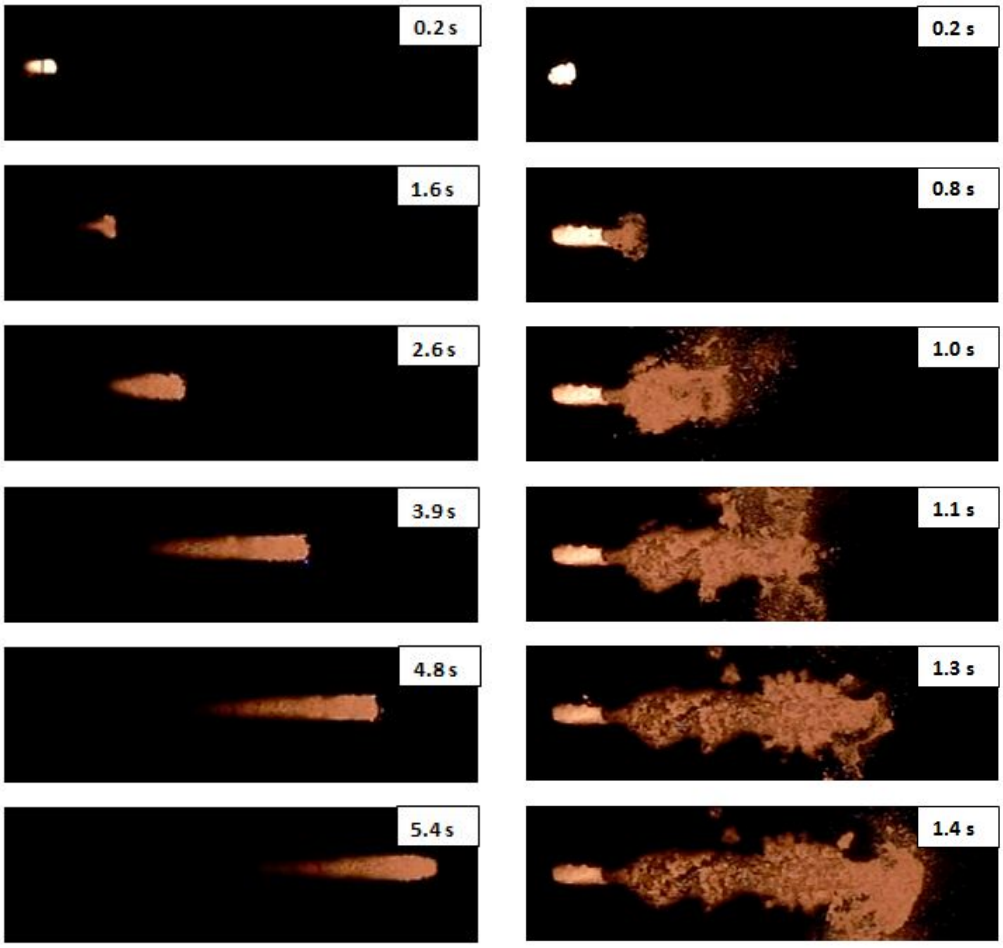


**(a)** Non-milled powders **(b)** Ball milled powders

**Figure 5.1:** Sequential frames illustrating the flame propagation in Al-Ni system in the 0.75 cm channel

It was also important to verify the steady state condition of the flame. Figure 5.3 shows an example of the flame speed variations along the channel among six different trials. It is unclear whether the flame speed is lower or higher at both ends of the channel. However, the flame speeds are more constant about 0.02 m after the initial ignition and 0.01 m before the end of channel. As a result, instead of considering the whole channel length, the average flame speed was taken between 0.02 m to 0.06 m of the channel length.

Figure 5.4 shows the flame speed measurements in the non-milled powders for different channel sizes. Each color shows results for a specific channel size (channel width). The flame in the smallest channel of 0.1 cm did not propagate. The flame rapidly extinguished shortly after the ignition, potentially due to high heat losses. However, the flame speeds

**Figure 5.2:** Burnt Al-Ni milled powders after the reaction

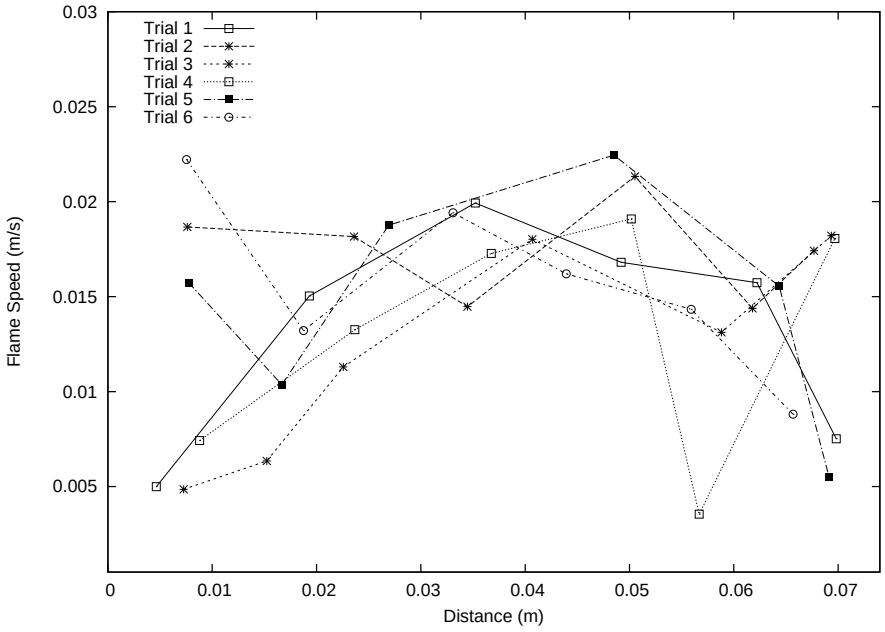


**Figure 5.3:** Non-milled Al-Ni flame speed along the channel length (for 0.5cm channel width)

for the other channel dimensions were found independent of their size. Therefore, it can be concluded that the flame speed is weakly affected by heat losses, except near the limit.

The results shown in Figure 5.4 also show that the flame speed increases at compactions higher than approximately ($\rho_{rel} > 0.60$ to 0.65). This critical density correlated very well with the onset of strong plastic deformation of the powders. Above this limit, the cold pressing of the powders required a much stronger compaction force and severe plastic deformation.

The flame speed measurements conducted in the ball-milled powders are shown in Figure 5.5 for the different channel sizes. For milled powders, the flame speed appears to be independent of the channel sizes for a width of 0.5 cm and higher. The channel that was 0.25 cm wide had a slightly lower flame speed compared to 0.5, 0.75, and 1 cm channels, and the flame speed for a 0.1 cm channel is significantly lower compared to other

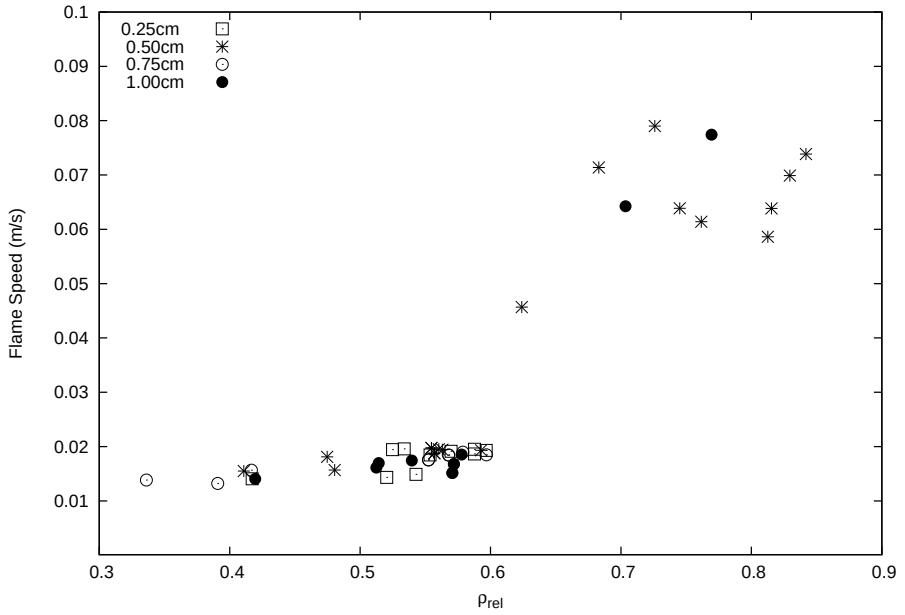


**Figure 5.4:** Average Al-Ni (non-milled) flame speed for different channel sizes and different compaction ratio

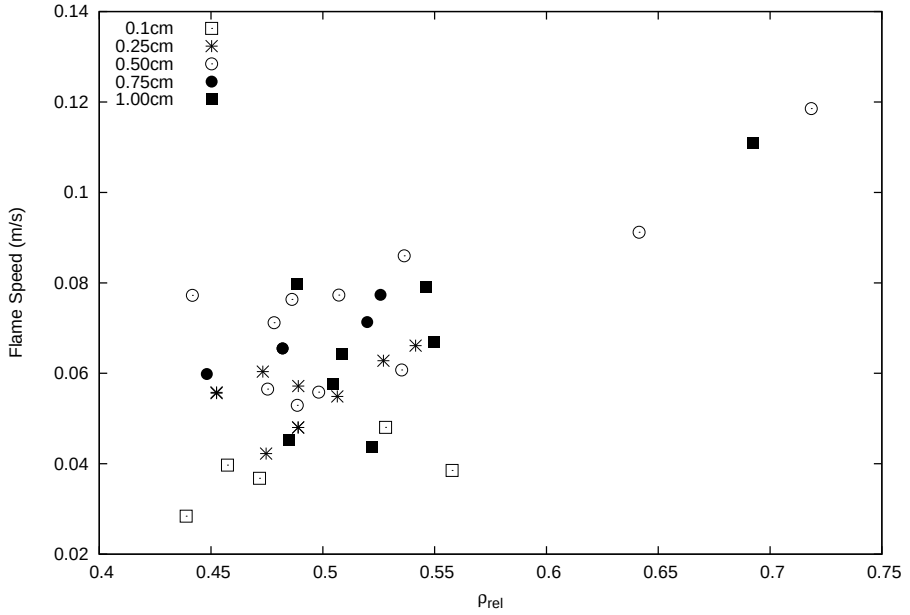


**Figure 5.5:** Average Al-Ni (ball-milled) flame speed for different channel sizes and different compaction ratio

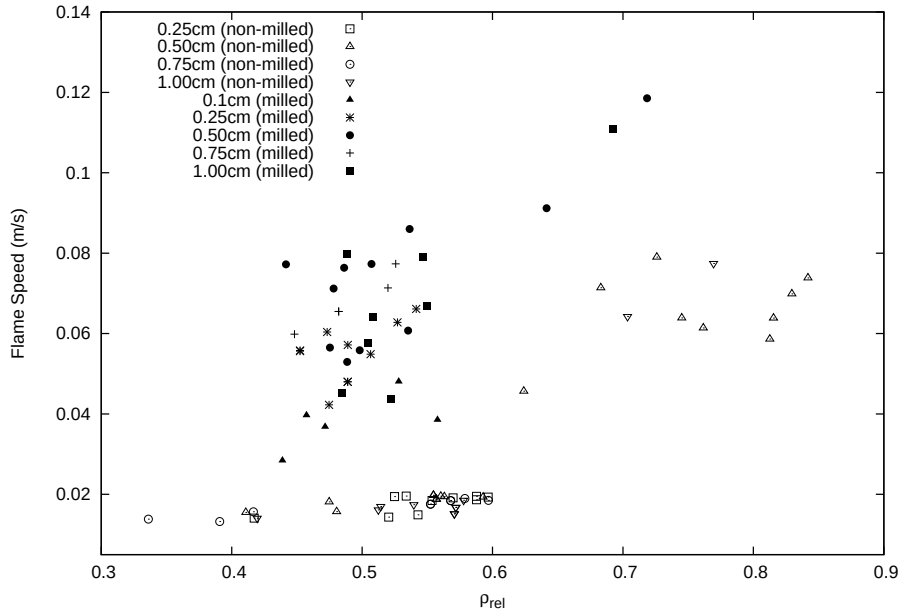


**Figure 5.6:** Comparison of non-milled and milled Al-Ni flame speed

channels. As a result, the heat loss effects are negligible for channel sizes of 0.5 cm or larger.

Figure 5.6 shows the comparison of the flame speeds measured in the non-milled and milled powders. The flame speed was generally found larger in the ball-milled system by approximately a factor of 3. Also apparent from Figure 5.6 is the much larger scatter in the ball-milled mixtures. Whether this reflects a genuine instability is not clear. These fluctuations may also correlate with the random bursts observed in the video. Experiments were performed with a glass cover to reduce the jump of incandescent particles ahead of the flame and the same statistical fluctuations were observed.

### Comparison with previous measurements

There are several studies focused on measuring the flame speed of Al-Ni mixtures. Some experimental results from literature are presented here for comparison purposes.

Bacciochini *et al.* measured the flame speed in a near TMD mixture of milled Ni-Al powders. The high compactions were obtained using the Cold Gas Dynamic Spray (CGDS) method [9]. The micro-structure of the deposited milled powders using the low temperature technique (T=300 $^{o}$C) is reported to be very similar to the original milled powders before cold spraying (shown in Figure 5.7). However, using the high temperature cold spraying technique (T=600 $^{o}$C), some powders were ignited during spraying, causing

a lower flame speed. The flame speed variation for normal and cold spray powders is shown in Figure 5.8. As explained in the Introduction, the flame speed for the cold spray powders is larger than the values obtained at low compaction.

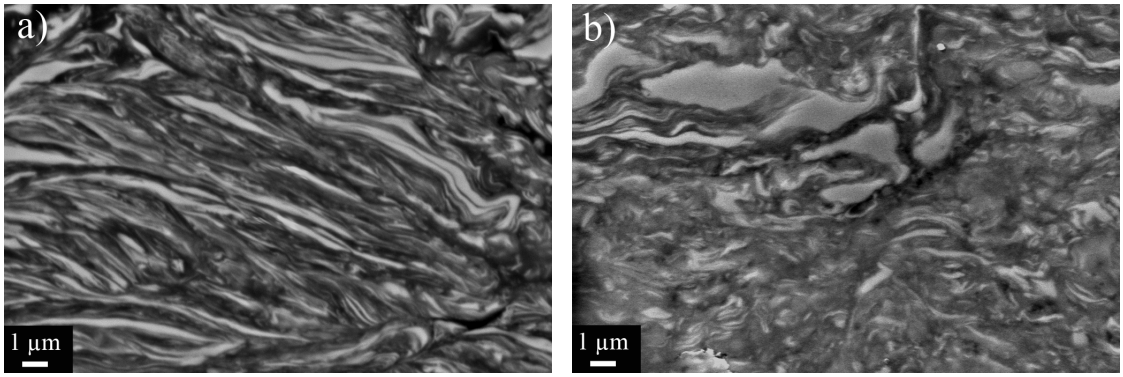


**(a)** T=300 $^{o}$C **(b)** T=600 $^{o}$C

**Figure 5.7:** Microstructure details of CGDS deposits manufactured [9]

Bacciochini *et al.* also reported data at low compactions [9]. These were obtained earlier by Barrett [47] with a similar procedure to that explained in Section 4.3.1. The results of his experiments along with our experimental results are presented in Figure 5.9.

For the non-milled Al-Ni powders, the flame velocities measured by Barrett and those obtained in the present study agree very well. However, the results reported by Barrett for ball-milled mixtures are somewhat lower than ours, as can be seen from Figure 5.9. This discrepancy may be due to differences in the milling technique used by Barrett. Inspection of the micrographs reported by Barrett, as shown in Figure 5.10, shows larger lamellar structures than in the present study. In view of Makino's model described in Chapter 2, a smaller characteristic size of the constituents means faster particle regression rates and faster flame speeds. This may explain why his flame speeds were lower than ours. This discrepancy however does not affect Bacciochini's results using the spray technique, since they used the same ball milling technique as ours.

### 5.1.2 Flame Speed in Tubes

Flame speed measurements have also been conducted in tubes, as described in the previous Chapter. Figure 5.11 shows, for example, a sequence of frames taken from an experiment using Al-Ni powders in a 5 mm inner diameter tube. The images show how the flame location can be deduced from the intense thermal radiation of the confining tube.

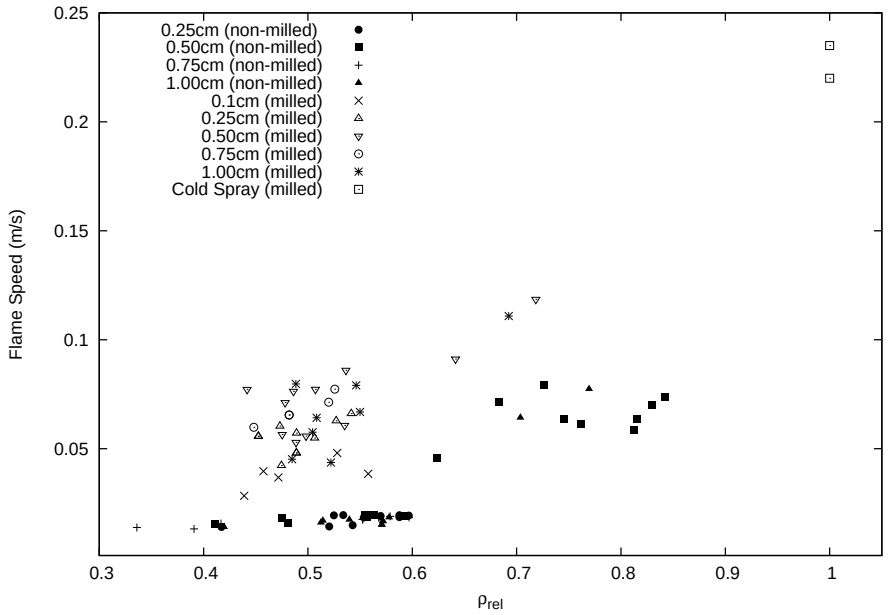


**Figure 5.8:** Ball-milled, cold-sprayed ball milled, and non-milled Al-Ni flame speed comparisons for different channel sizes

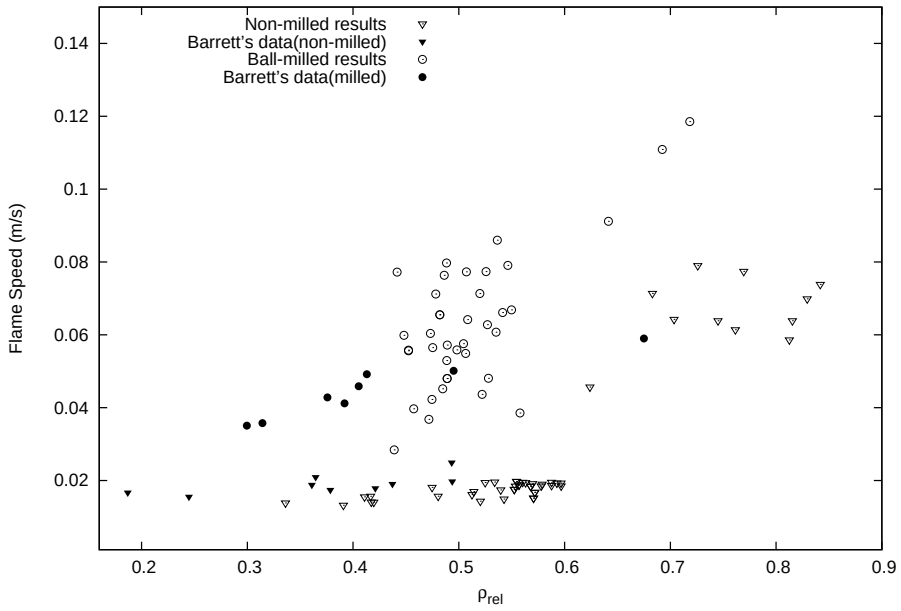


**Figure 5.9:** Comparison of experimental flame speed with Barrett's results

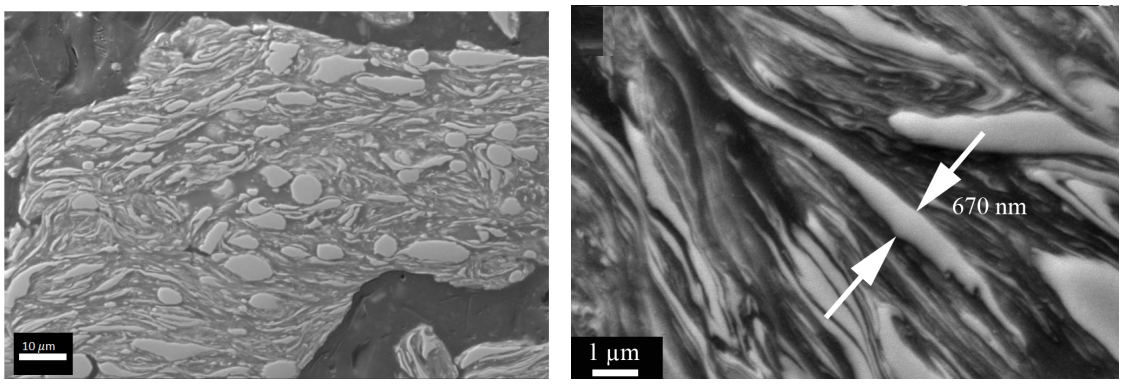


**(a)** Al-Ni milled powders used in Barrett's experiments[47]

**(b)** Al-Ni milled powders used in our experiments

**Figure 5.10:** Comparison of SEM image of Al-Ni milled powder prior to combustion

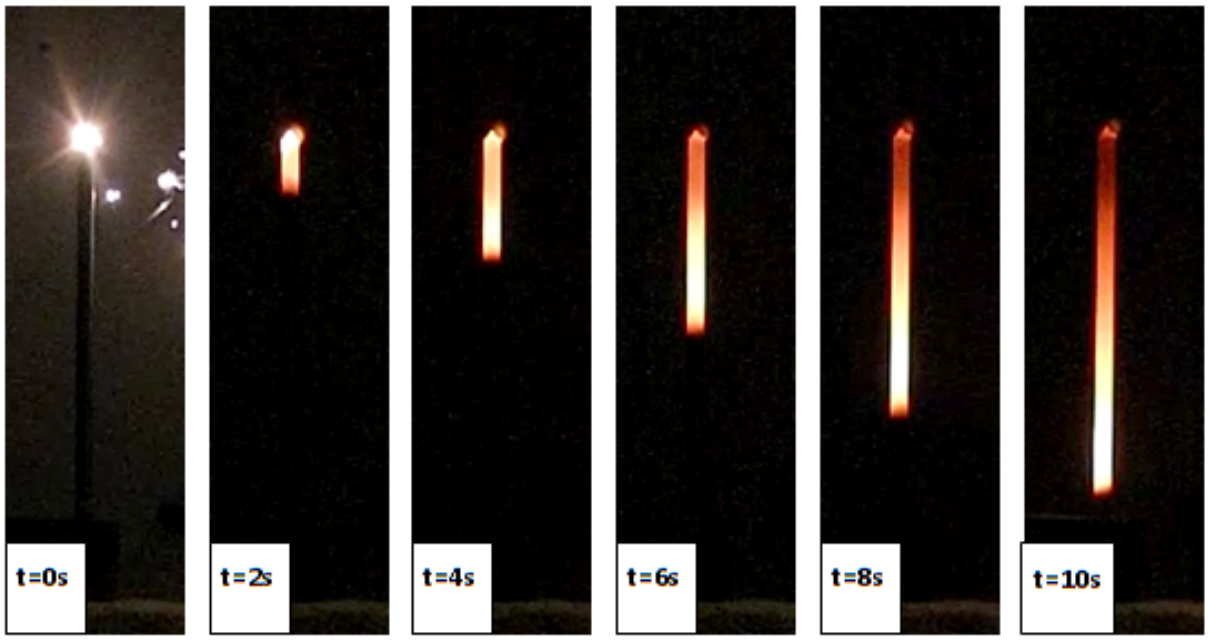


**Figure 5.11:** Sequential frames illustrating the flame propagation in non-milled Al-Ni system in the stainless steel tube ($d_{in,tube}$=5 mm, $\rho_{rel} = 32.3\%$)

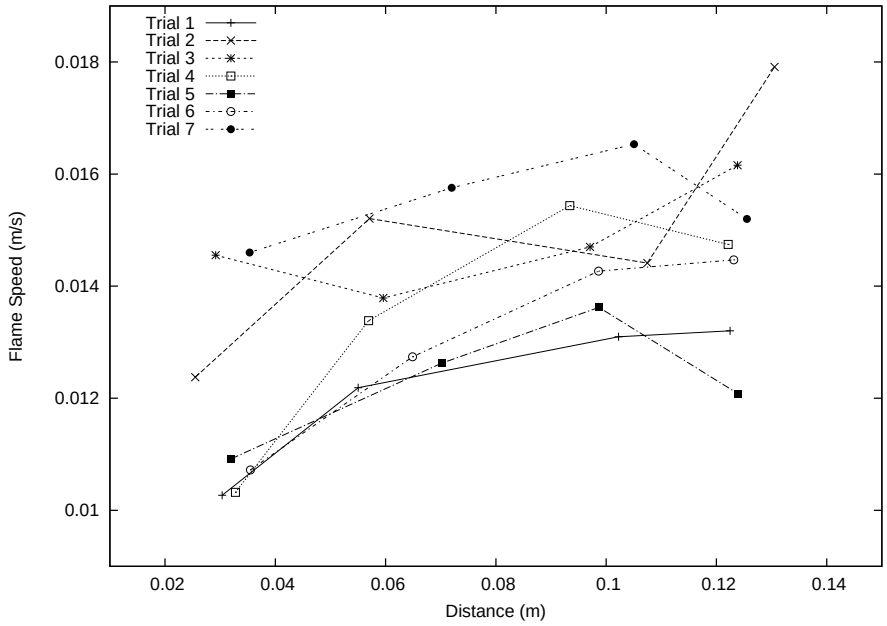


**Figure 5.12:** Non-milled Al-Ni flame speed along the tube length

The flame speed in the tube experiments was based on the location of the bright region on the outer surface of the tube. Due to the finite thermal conductivity of the tube, there exists a delay between when the flame arrival at a certain location and light emission from the outer wall of the tube. This delay is assumed to be almost identical along the tube length. As a result, for calculating the flame speed, where the time difference between different points are needed, this delay effect is eliminated.

Measurements of the flame speed along the tube length are shown in Figure 5.12. The flame speed is initially lower in most cases and reaches a steady state condition 2 cm to 4 cm after the initiation. One possible reason for having a lower initial flame speed is that Ti-Si powders are not fully compressed. Therefore, the energy release of the Ti-Si powders (per unit volume) was less than energy released from compacted Al-Ni mixture. Since the flame speed is proportional to energy released from the mixture, it is expected to have a lower flame speed at the start. The average flame speed reported for the tube experiments was estimated by eliminating the transient observed during the first 3 cm of the tube.

The average flame speeds recorded for different tube sizes are shown in Figure 5.13 for non-milled Al-Ni powders. As expected, the flame speed increases with density ratio. Comparison of the flame speeds for different tube sizes shows that the effect of heat losses for tube sizes larger than $d_{in}$= 0.34 cm is negligible and therefore the adiabatic assumption is acceptable. Successful propagation of flames was however not observed in the tubes with

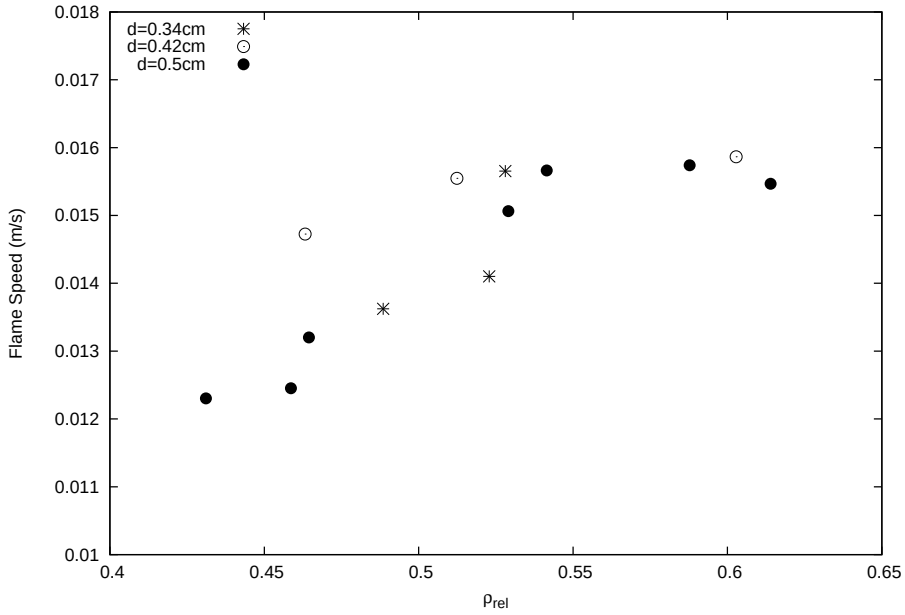


**Figure 5.13:** Non-milled Al-Ni flame speed in tubes

a diameter of 0.27 cm and smaller.

For density ratios larger than approximately 62%, no steady flame was observed in any of the tubes used. This behavior is not clear at present. It is believed that at high compaction, powders would not be able to move in the tubes, and the thermal expansion of the hot product would put a large compressive stress on the unburnt powders ahead of the flame. This explanation remains to be verified.

#### Comparison with the flame speed in channels

Figure 5.14 shows the flame speed in channels and tubes for non-milled powders as a function of density ratio. Both results are in the same range in velocities, where the flame speed in the tubes is lower by an average of 5-15%. Using different compaction techniques for the channels and the tubes could be the source of these differences.

### 5.1.3 Thermal Conductivity Measurements and Predictions at room temperature

#### Experimental results

As explained in Chapter 4, the thermal conductivity measurements in powder compacts was performed using the *steady state divided bar technique*. The technique restricted us

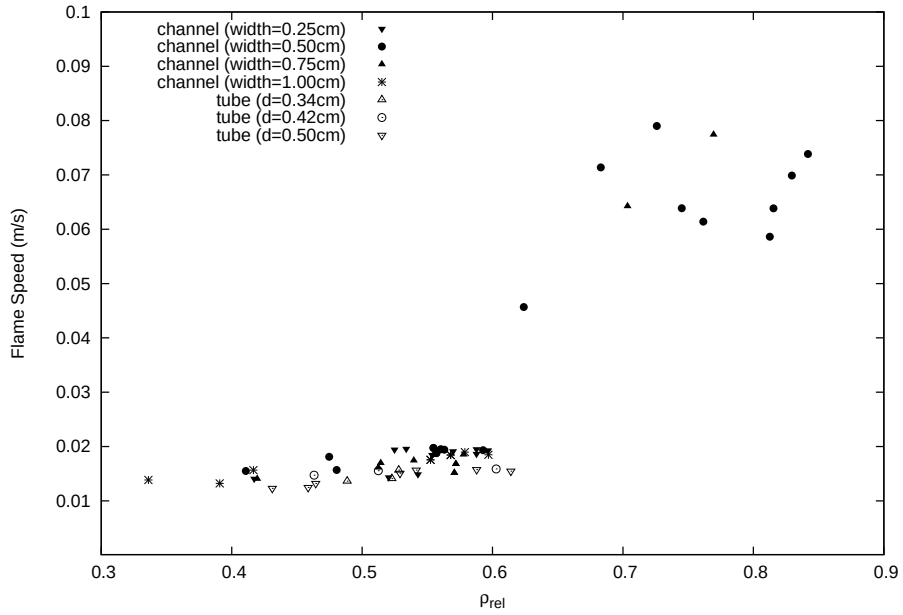


**Figure 5.14:** Comparison of the flame speed in the channels and tubes

to measure only weakly compacted powders in the density range $\rho_{rel} = 0.4$ to 0.65.

Figure 5.15 shows the measured thermal conductivities for the Al-Ni powders. A weak density dependence is observed over the range investigated, in spite of the 10% estimated error in the measurements. These data can now be compared with analytical models and previous experimental measurements.

### Comparison with analytical models

To analytically estimate the thermal conductivity of Al-Ni mixture, both the external and internal porosity techniques are analyzed. Knowing the conductivity of aluminum and nickel, it is first required to determine the conductivity of Al-Ni mixture at 100% density ratio (TMD). For a fully dense Al-Ni mixture, the aluminum powders have a lower Young's Modulus value and are expected to be deformed first. Therefore, compactions and deformations of the powders up to 100% density ratio creates an internal porosity mixture where aluminum is the medium and the nickel particles are the randomly dispersed particles. Based on the analysis discussed in Chapter 3, the Maxwell and EMT models can be used to estimate thermal conductivity of Al-Ni at the maximum density. Based on the 1:1 mole ratio and the molar densities of aluminum and nickel, 40% of volume is occupied by nickel and 60% by aluminum. The results for both models are similar with $K_e = 168$ W/(m·K). This result will be used later for calculating the thermal conductivity

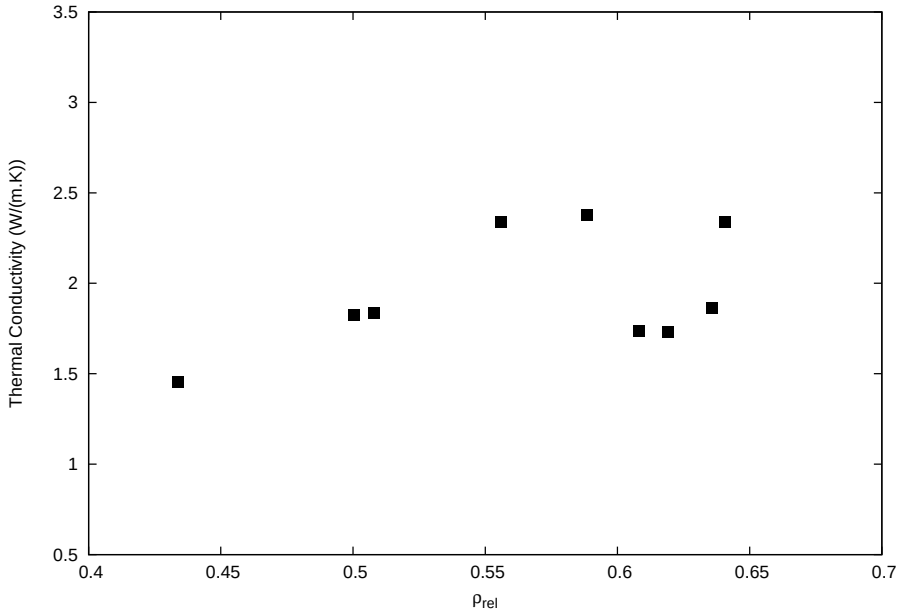


**Figure 5.15:** Thermal conductivity measurement of Al-Ni powders

of Al-Ni powders at different density ratios. It must be noted that if nickel was assumed to be the medium, the mixture conductivity would be reduced to $K_e = 162$ W/(m·K).

Knowing the theoretical maximum density $\rho_{TMD}$, the external and the internal porosity models can be used to estimate the thermal conductivity of powders at different relative densities. By assuming an external porosity mixture, the empirical model by Aivazov *et al.* [29] is used. Based on the results shown in Chapter 3 for the Aivazov empirical model, we have:

$$K = K_0 \frac{1 - v_1}{1 + n v_1^2} \tag{5.1}$$

By curve fitting this equation using the results of powder conductivity measurement (Figure 5.15), it is now possible to solve for the empirical constant in Equation 5.1, giving a value of $n = 198$.

By taking the Al-Ni mixture as an internal porosity material, we can compute the thermal conductivity of the mixture as a function of density ratio using Effective Medium Theory (EMT):

$$K_e = \frac{1}{4}[(3v_2 - 1)K_2 + [3(1 - v_2) - 1]\, K_1 + \sqrt{[(3v_2 - 1)\, K_2 + (3\,(1 - v_2) - 1)\, K_1]^2 + 8K_1K_2}] \tag{5.2}$$

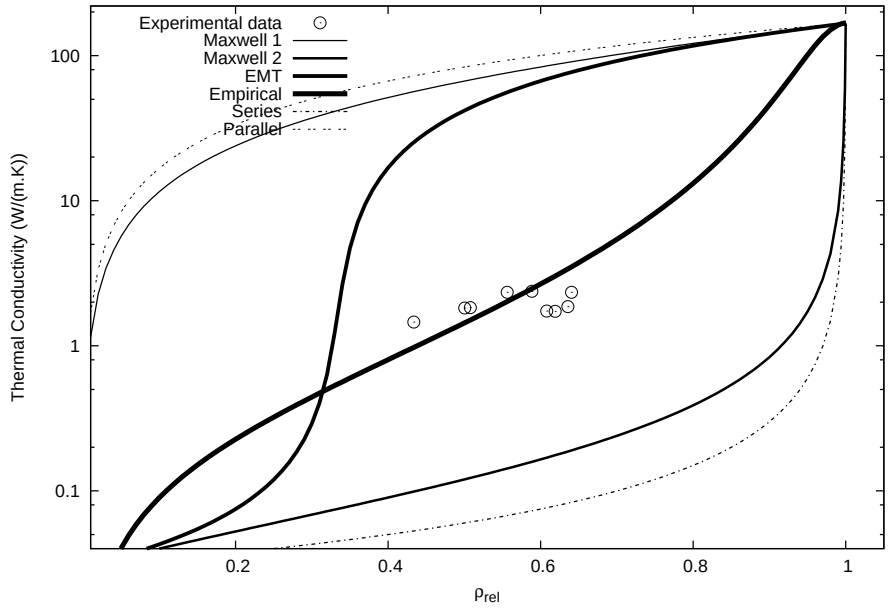


**Figure 5.16:** Thermal conductivity comparison of different models with the experimental results

This model along with experimental results, empirical model, Maxwell model, Parallel model, and Series model are presented in Figure 5.16. The Maxwell model is presented here as an internal porosity material (Maxwell 1) and also as an external porosity material (Maxwell 2). Clearly, only the semi-empirical model provides a good fit to our data. The Effective Medium Theory model captures only the low density results, but fails to capture the overall trend. The results nevertheless indicate that the conductivity in our experiments is consistent with a material that has both internal and external porosities. Interestingly, taking the algebraic mean of the Maxwell model evaluated for both internal and external porosity media yields a very good agreement with our data.

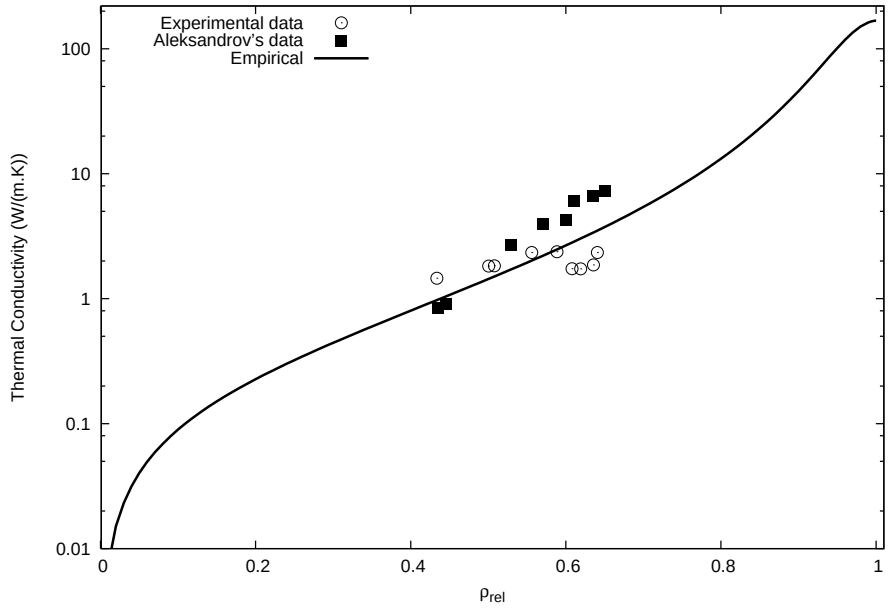


**Figure 5.17:** Comparison of experimental data and the empirical graph between our results and Aleksandrov's data

As explained in Chapter 3, the size and shape of Al-Ni powders are reported to have high influences on the thermal conductivity of powders. As a result, a comparison of exact values between results of different literature is inaccurate if different types of Al-Ni powders are used. However, it is still instructive to compare with previous measured data in the Ni-Al system. Aleksandrov *et. al* measured the thermal conductivity of Al-Ni powders for density ratios ranging between 0.45 to 0.65 [48]. A comparison between our measurements and those of Aleksandrov *et al.* are shown in Figure 5.17 which shows that both results are very close.

## 5.2 Comparison with Makino's predictions

In this section, Makino's model is analyzed to check the dependency of the model on the relative density of the mixture and heat conductivity. Using the heat conductivity trends outlined in the previous section, we then compare the predictions of flame speed with the flame speed measurements.

### 5.2.1 Makino's Model as a Function of Porosity

Using the results from Chapter 2, Makino model predicts an adiabatic flame speed $u_0$ given by

$$u_0 = \frac{D_0\sqrt{3\Lambda\frac{(K/c)}{(\rho_t D)_0}}}{R_0}\sqrt{\frac{\rho_M/\rho_N}{1-Z_0}} \tag{5.3}$$

where the radius of the non-metal powders $R_0$ and the mass diffusivity $D_0$ are properties of the materials, and independent of the porosity of the powders. The stoichiometric mass ratio $f_{st}$ and the mixture ratio $\mu$ (initial molar ratio of non-metal (N) to metal (M) divided by the corresponding stoichiometric molar ratio) are also dependent on the types of powders and ratios of the metal and the non-metal, independent of the porosity.

The degree of dilution $\kappa$, the initial mass fraction of the diluent, is a function of porosity if air is considered as the diluent. However, the mass of air is negligible compared to masses of metals and non-metals. As a result, the initial mass fraction of the air can always be assumed zero for all of the porosity ratios.

The density ratio of metal to non-metal $\rho_M/\rho_N$ is also independent of the relative density. The mass fraction of fluid $Z$ was defined in Chapter 2 (Equation 2.43) to be:

$$Z = \frac{\rho_f}{\rho_f + \rho_s} \tag{5.4}$$

According to equations 2.15 and 2.13, the solid and fluid densities ($\rho_s$ and $\rho_f$) are dependent on the non-metal and metal densities ($\rho_N$ and $\rho_M$), thus, $Z$ is independent of the density ratio.

The mass burning rate $\Lambda$, which is estimated numerically from the conservation equations, is a function of the boundary conditions (Equation 2.74), the stoichiometric mass ratio $f_{st}$, the mixture ratio $\mu$, and the degree of dilution $\kappa$, which are all shown to be independent of the density ratio.

Lewis number $Le_0$ is the ratio of the thermal diffusivity over the mass diffusivity:

$$Le_0 = \frac{(K/c)}{(\rho_t D)_0} \tag{5.5}$$

As mentioned before, the specific heat $c$ and the mass diffusivity $D_0$ are the material properties, independent of the porosity ratios. Total density $\rho_t$ is defined as the relative density of a compacted medium $\rho_{rel}$ multiplied by the theoretical maximum density $\rho_{TMD}$:

$$\rho_t = \rho_{rel}.\rho_{TMD} \tag{5.6}$$

Clearly $\rho_t$ is a function of relative density. The thermal conductivity of the mixture $K$ is also a function of porosity.

In conclusion, we can see that the thermal diffusivity of SHS reactions, which also controls the flame speed, is a function of relative density. Therefore, by only changing the porosity of the mixture, the flame speed is related to the square root of thermal conductivity over the relative density, i.e.,

$$u_0 \propto \sqrt{\frac{K}{\rho_{rel}}} \tag{5.7}$$

or

$$u_0 = A\sqrt{\frac{K}{\rho_{rel}}}, \qquad A = \frac{D_0\sqrt{\frac{3\Lambda}{cD_0}}}{R_0}\sqrt{\frac{\rho_M/\rho_N}{1-Z_0}} \tag{5.8}$$

where $A$ is assumed to be constant.

### 5.2.2 Effect of Powder Compaction

The maximum theoretical relative density for any spherical powders without deformation corresponds to a face centered cubic lattice with $\rho_{rel} = 0.74$. In practice, the maximum relative density is lower depending on the shape and size of powders. For our experiments, the maximum relative density is about 0.6 density ratio.

Compacting the powders with a very high load causes the powders with a lower Young's Modulus (aluminum in our case) to deform from their original shape and fill the gaps. As a result, the mixture suddenly changes from an external porosity material to an internal porosity material. Also, as shown earlier, the internal porosity materials have a much higher thermal conductivity compared to external porosity materials. Consequently, since the thermal conductivity is related to the flame speed, we expect to have a critical range of relative density ($\rho_{rel} \approx 0.60$), where the flame speed suddenly increases.

Mukasyan *et al.* [7] also reported this phenomenon to be true for Al-Ni clad particles in a range of relative density of 0.45 to 0.7, shown in Figure 1.4. The critical density for their experiments was reported to be around 0.65 to 0.67 relative density. To understand this effect better, in order to increase relative density from 0.48 to 0.65, a load of about 100 g/cm$^2$ was applied in Mukasyan's experiment, while to reach a relative density of 0.68, the load was increased to 500 kg/cm$^2$.

Al-Ni powders used in our experiments were compacted with relatively low force up to a relative density of around 0.5. Compacting the powders to higher density ratios required deforming the powders. This deformation changed the porosity type of the mixture from an external porosity to an internal porosity material. Therefore, we used the Aivazov empirical model for low density mixtures and the EMT model for higher density powders.

To conclude the dependency of the adiabatic flame speed on the porosity ratio, two different models are used for high and low relative densities. For both models, the relative density of a compacted medium $\rho_{rel}$ and the thermal conductivity $K$ are functions of porosity ratios and can influence the flame speed. As a result, if all parameters except porosity are kept constant, the flame speed is related to $\rho_{rel}$ and $K$:

$$u_0 \propto \begin{cases} \sqrt{\frac{K_{empirical}}{\rho_{rel}}} & \text{if} \quad \rho_{rel} < 0.6 \\ \sqrt{\frac{K_{EMT}}{\rho_{rel}}} & \text{if} \quad \rho_{rel} > 0.6 \end{cases} \tag{5.9}$$

or

$$u_0 = A \begin{cases} \sqrt{\frac{K_{empirical}}{\rho_{rel}}} & \text{if} \quad \rho_{rel} < 0.6 \\ \sqrt{\frac{K_{EMT}}{\rho_{rel}}} & \text{if} \quad \rho_{rel} > 0.6 \end{cases} \tag{5.10}$$

where A is a constant that includes all other terms that are independent of the porosity ratios (Equation 5.8).

In practice, we expect that the change of model will appear over a range of density ratios rather than a specific value. The critical density ($\rho_{rel} = 0.6$) is set to simplify the scenario and any intermediate mixture (internal/external porosity mixture) is neglected. To show this transition better, flame speed can be presented over a short range of relative density ($0.6 < \rho_{rel} < 0.7$) chosen arbitrarily where the flame speed is a linear relationship connecting both graphs. It must be noticed that this range is only chosen to present a better view of the results and linearly connecting both graphs is not a proven model.

### 5.2.3 Comparison of the model with the experimental results

#### Non-milled powders

Using modified Makino's equation 5.10, we can plot the flame speed as a function of density ratio. As shown in Table 5.1, some of the Al-Ni properties are taken from Makino's publication [5] and other properties are taken from calculated data, the experimental results, and the laboratory environment.

The thermal conductivity and the relative density of the mixture can vary based on the density ratio of the mixture. Using Equation 5.10 and the data from table 5.1, an equation for the flame speed is estimated as a function of density ratio (shown in Figure 5.18 along with the experimental data). The dashed curves represent the Empirical and EMT models. The mix model (the solid line) is the resultant of the two models for lower and higher density ratio mixtures. As shown in Figure 5.18, there is a very good

**Table 5.1:** Properties of Al-Ni mixture

| Property | |
|---|---|
| 1- Activation temperature: $T_d$ | 9010 $^o$K [5] |
| 2- Specific heat: $c$ | 1.18 kJ/kg [5] |
| 3- Heat of combustion: $q^o$ | $2 \times 10^3$ kJ/kg [5] |
| 4- Pre-exponential factor: $D_o$ | $4.8 \times 10^{-6}$ m$^2$/s[5] |
| 5- Density of aluminum: $\rho_{Al} = \rho_m$ | $2.69 \times 10^3$ kg/m$^3$ |
| 6- Density of nickel: $\rho_{Ni} = \rho_n$ | $8.85 \times 10^3$ kg/m$^3$ |
| 7- Theoretical maximum density of Al-Ni: $\rho_{TMD}$ | $5.18 \times 10^3$ kg/m$^3$ |
| 8- Conductivity of Al-Ni at $\rho_{TMD}$ | 168 W/(m.K) |
| 9- Conductivity of air: $T_{air}$ | 0.03 W/(m.K) |
| 10- Melting temperature of aluminum: $T_{m.Al} = T_m$ | 934 $^o$K |
| 11- Initial temperature: $T_o$ | 300 $^o$K |
| 12- Radius of nickel: $R_o$ | $2 \times 10^{-6}$ m |
| 13- Thermal conductivity: $K$ | Varies |
| 14- Relative density: $\rho_{rel}$ | Varies |

agreement between Makino's equation (the mix model) and the experimental results for the non-milled Al-Ni powders.

### Ball-milled powders

One of the difficulties in modeling Makino's modified equation for the milled powders is in determining the sizes of particles. As explained in Chapter 2, the exact sizes of particles ($R_o$) are required for Makino's model in order to complete the equation. However, for milled powders, nickel and aluminum were deformed and particles with random shapes and sizes were created, as shown in Figure 4.5. Therefore, estimating the exact sizes of nickel particles is very ambiguous. We can estimate a size for the milled powders $R_o$ so the flame speed in Makino's model agrees well with experimental results at high density ratios. By estimating $R_o$, it is now possible to verify if the model agrees with the experimental

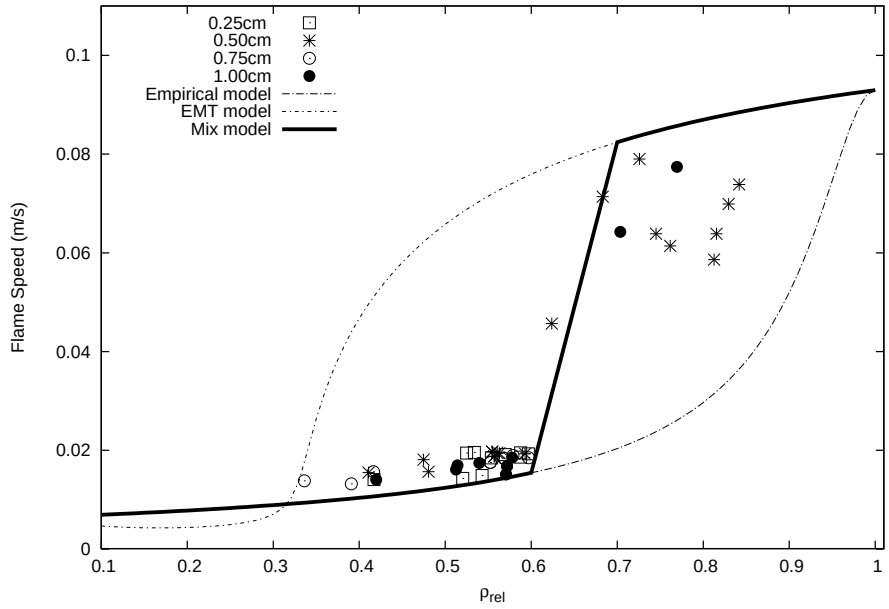


**Figure 5.18:** Experimental flame speed for the non-milled powders and Makino's predicted flame speed model

flame speed at other porosities.

Figure 5.19 shows the experimental result along with Makino's flame speed model using the mix thermal conductivity model. As shown in Figure 5.19, there is a good agreement between the experimental results and the mix model. Comparison of the flame speeds for non-milled and milled models along with experimental data is shown in Figure 5.20. It can be seen that the model works better for the non-milled powders. The model for the milled powders seems to under-predict the flame speed at low density ratio powders (or over-predict the flame speed at very high density ratio mixtures). The cause of this error is still unclear.

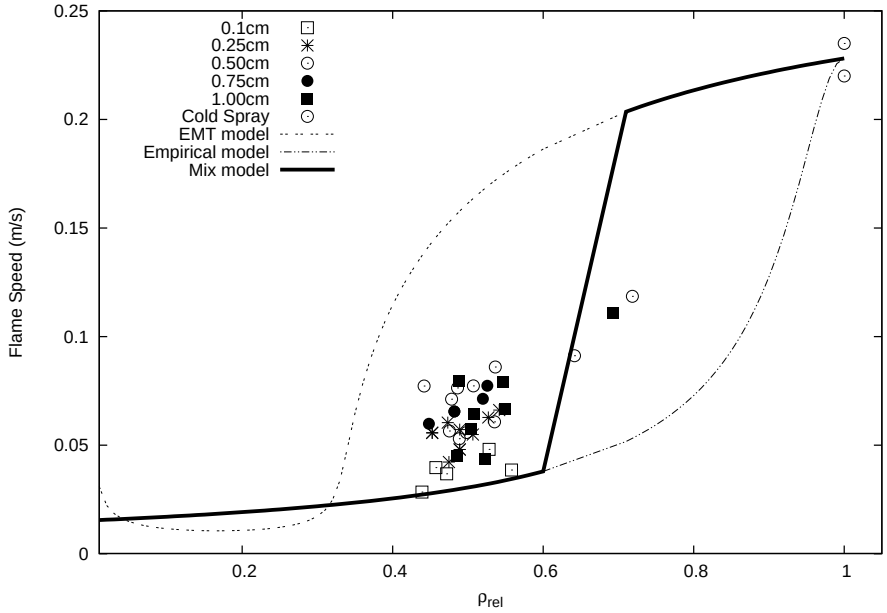


**Figure 5.19:** Experimental flame speed for the milled powders and Makino's corrected model

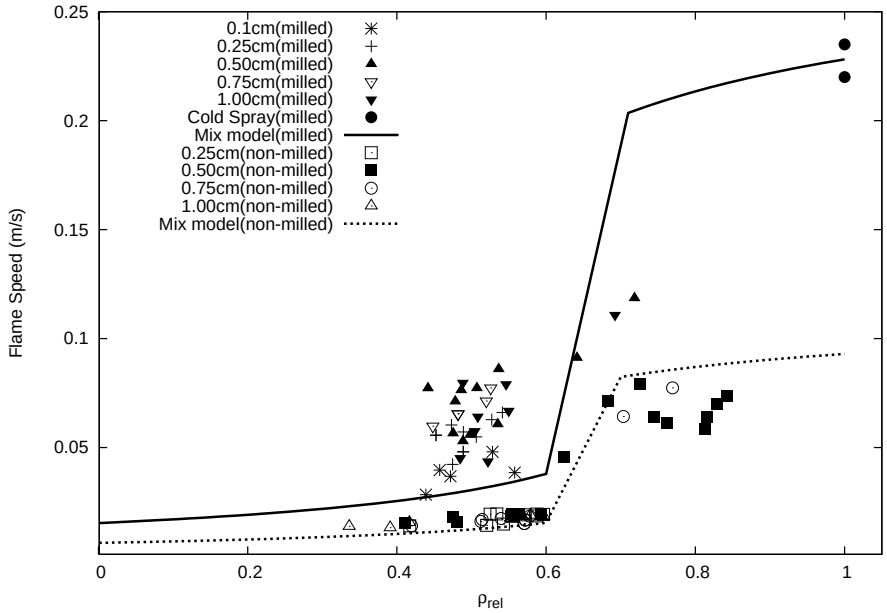


**Figure 5.20:** Experimental flame speed for the milled and non-milled powders and Makino's corrected model

### Size dependency of powders

Studying the relation between the flame speed and the particle size is not the primary focus of this thesis since this subject has been studied well in other literature [5, 49]. However, following Makino's model, it is possible to understand the flame speed variation between milled and non-milled powders. Generally, small particles have larger contact areas per unit mass compared to larger particles and therefore, faster ignition is possible. This can also be explained using Makino's model. According to Makino's adiabatic equation 2.75, the flame speed is inversely proportional to the particle sizes represented by the radius of non-metals $R_0$:

$$u_0 \propto \frac{1}{R_0} \tag{5.11}$$

As it was shown earlier in Figures 4.1 and 4.5, the particle sizes in ball-milled powders are much smaller than the non-milled ones. As a result, it is expected to have higher flame velocities in the ball-milled powder experiments.

# Chapter 6

# Conclusion

The main objective of this thesis was to study the effect of powder porosity on the flame speed in bi-metallic reactive systems. The investigations were based on the analytical model formulated by Makino [5], by controlling how the variables are affected by changes in density. Flame speed measurements were performed in Al-Ni mixtures at different initial densities. The density was varied by pressing the powders inside metallic channels and tubes. Experiments were also performed in ball-milled samples, in order to permit comparison with the experiments performed by Bacciochini *et al.* [9] in these mixtures at nearly maximum densities. The measurements revealed that the flame speed increases with the initial density, with a discontinuous transition occurring at approximately 60% of the theoretical maximum density (TMD). This transition also corresponded to the point where the powders deformed plastically during the compaction process, suggesting that the intimate contact between the particles is responsible for the flame speed increase.

The flame speed dependence on powder density was attributed to the changes in the thermal conductivity of Al-Ni mixtures. Different thermal conductivity models for porous materials were then studied in order to relate the thermal conductivity of Al-Ni mixtures to the density ratio. At high densities, where the powders have plastically deformed, the continuous structure yields conductivities close to the idealized solid matrix (an internal porosity material). For such mixtures, most analytical models predict results in the same range. As a result, Effective Medium Theory (EMT) [18] was chosen to calculate the thermal conductivity of Al-Ni mixtures at high densities. At low densities, since Al-Ni was a mixture of loose powders, analytical models were no longer precise. Thus, the thermal conductivity was experimentally measured and then was fitted using the semi-empirical model suggested by Aivazov [29].

Using the empirical and EMT models, Makino's equation was derived as a function

of density ratio and the new model was then compared with the experimental data. A good agreement between the suggested model and experimental results was observed for both non-milled and milled Al-Ni powders. Therefore, the present thesis suggests that the dependence of flame speed on density is due mainly to the changes to the structure and thermal conductivity of the powders.

In the future, the flame speed and the thermal conductivity of Al-Ni mixtures should be experimentally measured at more intermediate levels in order to validate the model at any density ratio. In addition, to further validate the model, other reactive mixtures should be addressed. Finally, our results indicated that heat loss effects may play a stronger role at high density ratios. These trends should be clarified in the future, with possible corrections to the model due to heat losses.

# Bibliography


[1] A. Merzhanov, V. Shkiro, and I. Borovinskaya, "A method for synthesizing refractory compounds," *USSR Inventors Certificate no. 255221*, 1967.

[2] J. McCauley and J. Puszynski, "Erratum to: Historical perspective and contribution of us researchers into the field of self-propagating high-temperature synthesis (SHS)/combustion synthesis (CS): Personal reflections," *International Journal of Self-Propagating High-Temperature Synthesis*, vol. 17, pp. 156–156, 2008.

[3] I. P. Borovinskaya, "Chemical classes of the SHS processes and materials," *Institute for Structural Macrokinetics, USSR Academy of Sciences*, vol. 64, no. 7, pp. 929–940, 1992.

[4] A. Merzhanov, "History and recent developments in SHS," *Ceramics International*, vol. 21, no. 5, pp. 371–379, 1995.

[5] A. Makino, "Fundamental aspects of the heterogeneous flame in the self-propagating high-temperature synthesis (SHS) process," *Progress in Energy and Combustion Science*, vol. 27, no. 1, pp. 1–74, 2001.

[6] (2012, September) Institute of structural macro-kinetics materials science ras, SHS cast materials. [Online]. Available: http://www.ism.ac.ru/struct/SHS_Cast_Materials/gallery1.php

[7] A. Mukasyan and A. Varma, "Gasless combustion of aluminum particles clad by nickel," *Combustion Science and Technology*, vol. 170, no. 1, pp. 67–85, 2001.

[8] Naiborodenko., Yu.S., and V. Itin, "Gasless combustion of metal powder mixtures: 1. mechanism and details," *Combustion, Explosion, and Shock Waves*, vol. 11, no. 3, pp. 293–300, 1976.

[9] A. Bacciochini, M. Radulescu, Y. Charron-Tousignant, J. V. Dyke, M. Nganbe, M. Yandouzi, J. Lee, and B. Jodoin, "Enhanced reactivity of mechanically-activated nano-scale gasless reactive materials consolidated by cold spray," *Surface and Coatings Technology*, vol. 206, no. 21, pp. 4343 – 4348, 2012.

[10] A. Aldushin, T. Martem'yanova, A. Merzhanov, B. Khaikin, and K. Shkadinskii, "Propagation of the front of an exothermic reaction in condensed mixtures with the interaction of the components through a layer of high-melting product," *Combustion, Explosion, and Shock Waves*, vol. 8, pp. 159–167, 1972.

[11] K. Shkadinskii, B. Khaikin, and A. Merzhanov, "Propagation of a pulsating exothermic reaction front in the condensed phase," *Combustion, Explosion, and Shock Waves*, vol. 7, no. 1, pp. 15–22, 1973.

[12] A. Varma, A. S. Mukasyan, and S. Hwang, "Dynamics of self-propagating reactions in heterogeneous media: experiments and model," *Chemical Engineering Science*, vol. 56, pp. 1459–1466, 2001.

[13] A. Makino and C. Law, "On the correspondence between the homogeneous and heterogeneous theories of SHS," *Combustion and Flame*, vol. 124, no. 1-2, pp. 268–274, 2001.

[14] A. Hardt and P. Phung, "Propagation of gasless reactions in solidsi. analytical study of exothermic intermetallic reaction rates," *Combustion and Flame*, vol. 21, no. 1, pp. 77 – 89, 1973.

[15] S. Hwang, A. Mukasyan, A. Rogachev, and A. Varma, "Combustion wave microstructure in gas-solid systems: Experiments and theory," *Combust. Sci. Tech.*, vol. 123, no. 165, pp. 1459–1466, 1997.

[16] L. Massa, T. Jackson, J. Buckmaster, and M. Campbell, "Three-dimensional heterogeneous propellant combustion," *Proceedings of the Combustion Institute*, vol. 29, no. 2, pp. 2975–2982, 2002.

[17] T. Jackson and J. Buckmaster, "Heterogeneous propellant combustion," *AIAA J*, vol. 40, no. 6, pp. 1122–30, 2002.

[18] J. K. Carson, S. J. Lovatt, D. J. Tanner, and A. C. Cleland, "Thermal conductivity bounds for isotropic, porous materials," *International Journal of Heat and Mass Transfer*, vol. 48, no. 11, pp. 2150 – 2158, 2005.

[19] F. A. Williams, *Combustion Theory*, 2nd ed. Benjamin/Cummings, 1985.

[20] A. Makino and C. Law, "Heterogeneous flame propagation in the self-propagating high-temperature synthesis (SHS) process: theory and experimental comparisons," *In: The 24th Symposium (International) on Combustion. The Combustion Institute, Pittsburgh*, pp. 1883–91, 1992.

[21] A. Makino, "An approximate explicit expression for the combustion rate of a small carbon particle," *Combustion and Flame*, vol. 101, pp. 551–552, 1992.

[22] A. Makino and C. Law, "Burning velocity of the heterogeneous flame propagation in the SHS process expressed in explicit form," *Combustion and Flame*, vol. 101, no. 4, pp. 551–555, 1995.

[23] G. Bart, "Thermal conduction in non-homogeneous and phase change media," *Thesis, Delft University of Technology, Netherlands*, 1994.

[24] J. Maxwell, *A Treatise on Electricity and Magnetism*, 3rd ed. Dover Publications Inc, 1954.

[25] H. T. Davis, L. R. Valencourt, and C. E. Johnson, "Transport processes in composite media," *Journal of the American Ceramic Society*, vol. 58, no. 9-10, pp. 446–452, 1975.

[26] S. Kirkpatrick, "Percolation and conduction," *Rev. Mod. Phys*, vol. 45, pp. 574 – 588, 1973.

[27] R. Landauer, "The electrical resistance of binary metallic mixtures," *Rev. Mod. Phys*, vol. 23, pp. 779 – 784, 1952.

[28] H. W. Russell, "Principle of heat flow in porous insulators," *Journal of the American Ceramic Society*, vol. 18, no. 1-12, pp. 1–5, 1935.

[29] M. I. Aivazov and I. A. Domashnev, "Influence of porosity on the conductivity of hot-pressed titanium-nitride specimens," *Powder Metallurgy and Metal Ceramics*, vol. 7, pp. 708–710, 1968.

[30] I. Sumirat, Y. Ando, and S. Shimamura, "Theoretical consideration of the effect of porosity on thermal conductivity of porous materials," *Journal of Porous Materials*, vol. 13, pp. 439–443, 2006.

[31] J. Kwon, H. J. Choong, J. Haeyong, and S. Tae-Ho, "Effective thermal conductivity of various filling materials for vacuum insulation panels," *International Journal of Heat and Mass Transfer*, vol. 52, no. 23, pp. 5525 – 5532, 2009.

[32] K. Johnson, "Contact mechanics," *Cambridge University Press, Cambridge*, pp. 84–100, 1985.

[33] J. Carsona, S. Lovatta, D. Tannerb, and A. Cleland, "An analysis of the influence of material structure on the effective thermal conductivity of theoretical porous materials using finite element simulations," *International Journal of Refrigeration*, vol. 26, no. 8, pp. 873 – 880, 2003.

[34] A. Mukasyan and A. Rogachev., "Discrete reaction waves: Gasless combustion of solid powder mixtures," *Progress in Energy and Combustion Science*, vol. 34, pp. 377–416, 2008.

[35] R. Kuriger and M. Alam, "Thermal conductivity of thermoplastic composites with sub-micrometer carbon fibers," *Experimental Heat Transfer*, vol. 15, no. 1, pp. 19–30, 2002.

[36] M. Wang and N. Pan, "Modeling and prediction of the effective thermal conductivity of random open-cell porous foams," *International Journal of Heat and Mass Transfer*, vol. 51, no. 56, pp. 1325 – 1331, 2008.

[37] K. Maglic, *Compendium of Thermophysical Properties Measurement Methods*. Plenum Press New York, 1994.

[38] K. Manohar, D. Yarbrough, and B. J.R., "Measurement of apparent thermal conductivity by the thermal probe method," *American Society for Testing and Materials*, 2000.

[39] D. Swift, "The thermal conductivity of spherical metal powders including the effect of an oxide coating," *International Journal of Heat and Mass Transfer*, vol. 9, no. 10, pp. 1061 – 1074, 1966.

[40] F. Albouchi, M. Fetoui, F. Rigollet, M. Sassi, and S. Ben Nasrallah, "Optimal design and measurement of the effective thermal conductivity of a powder using a crenel heating excitation," *International Journal of Thermal Sciences*, vol. 44, no. 11, pp. 1090–1097, 2005.

[41] A. Tam, "Applications of photo-acoustic sensing techniques," *Reviews of Modern Physics*, vol. 58, no. 2, pp. 381–431, 1986.

[42] M. Rohde, "Photo-acoustic characterization of thermal transport properties in thin films and microstructures," *Thin Solid Films*, vol. 238, no. 2, pp. 199 – 206, 1994.

[43] N. C. Fernelius, "Photo-acoustic chopping frequency studies on uncoated zinc selenide," *Appl. Opt.*, no. 3, pp. 481 – 490, 1982.

[44] J. J. Moore and H. Feng, "Combustion synthesis of advanced materials: Part ii. classification, applications and modeling," *Progress in Materials Science*, vol. 39, no. 45, pp. 275 – 316, 1995.

[45] E. Dreizin, "Metal-based reactive nano-materials," *Progress in Energy and Combustion Science*, vol. 35, no. 2, pp. 141–167, 2009.

[46] C. Law, *Combustion physics*. Cambridge University Press, Cambridge, New York, 2006.

[47] B. Barrett, "SHS reactions in aluminum nickel nano-composites and the effect of compaction on flame speed," University of Ottawa, 2010, undergraduate Thesis.

[48] V. V. Aleksandrov, V. A. Gruzdev, and Y. A. Kovalenko, "Thermal conductivity of certain aluminum-based SHS systems," *Combustion, Explosion, and Shock Waves*, vol. 21, pp. 93–99, 1985.

[49] E. Hunt, K. Plantier, and M. Pantoya, "Nano-scale reactants in the self-propagating high-temperature synthesis of nickel aluminide," *Acta Materialia*, vol. 52, no. 11, pp. 3183 – 3191, 2004.

# Appendix A

# Ansys model

The purpose of the Ansys model is to study the effect different parameters, such as the density ratio, particle sizes, and pore alignments, to the thermal conductivity of internal porosity materials.

To do so, a temperature gradient along a series of cubes with spherical holes was created, as shown in Figure A.1. The cube had a known thermal conductivity (100 W/(m·K)) and holes have no thermal conductivity. Based on the input temperate gradient and the calculated heat flux from Ansys, thermal conductivity of the porous cube could be estimated.

The top and bottom temperatures of the series of cubes were set to 273K and 373K respectively and the sides were kept insulated to create the temperature gradient only along the Y-axis (system symmetric along X and Z axis).

In order to have a semi finite porous system, multiple porous cubes were placed along each axis. Since the cubes are identical, there was no heat transfer between the cubes in X and Z axis. Therefore, the solution of a single cube along X and Z axis presents infinite number of cubes in these directions. However, since the heat flow was along the Y axis (bottom to top of the cubes), the boundary condition could vary the results based on the number of stacked cubes. In order to avoid this boundary condition problem, the number of cubes along the Y-axis was varied (shown in Figure A.1) until the resultant thermal conductivity became independent of the number cubes.

In addition, it was shown that the placements of the holes in cubes are important. Therefore, two different models of placements were examined. Model 1 is based on the *body centered cubic lattice* (Figure A.2a) and Model two is based on the *face centered cubic lattice* (Figure A.2b).

Figure A.3 shows the results for the thermal conductivity of these two models with

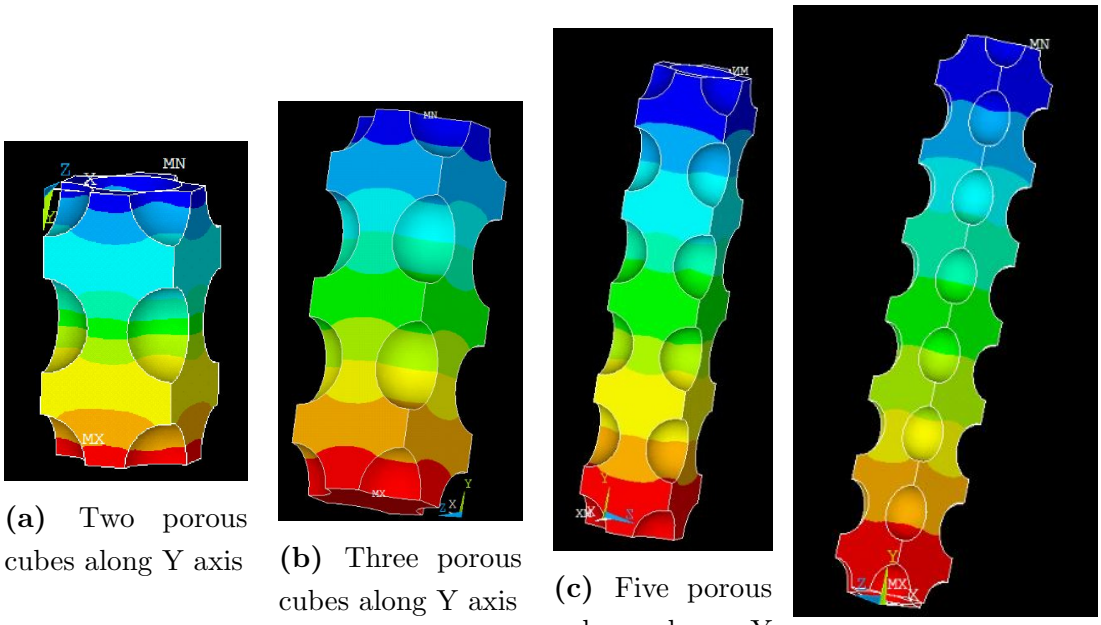

**(a)** Two porous cubes along Y axis

**(b)** Three porous cubes along Y axis

**(c)** Five porous cubes along Y axis

**(d)** Seven porous cubes along Y axis

**Figure A.1:** Ansys porous design with multiple porous cubic materials

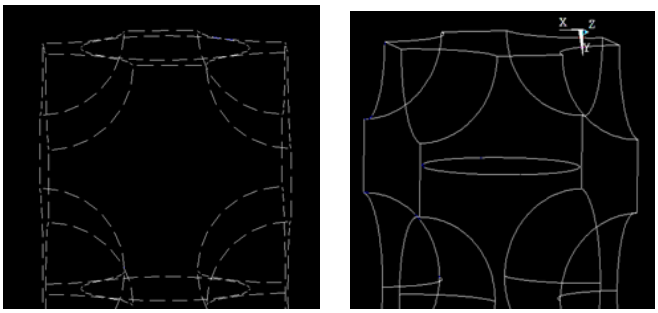

**(a)** Model 1

**(b)** Model 2

**Figure A.2:** Different models of pore placement in Ansys design

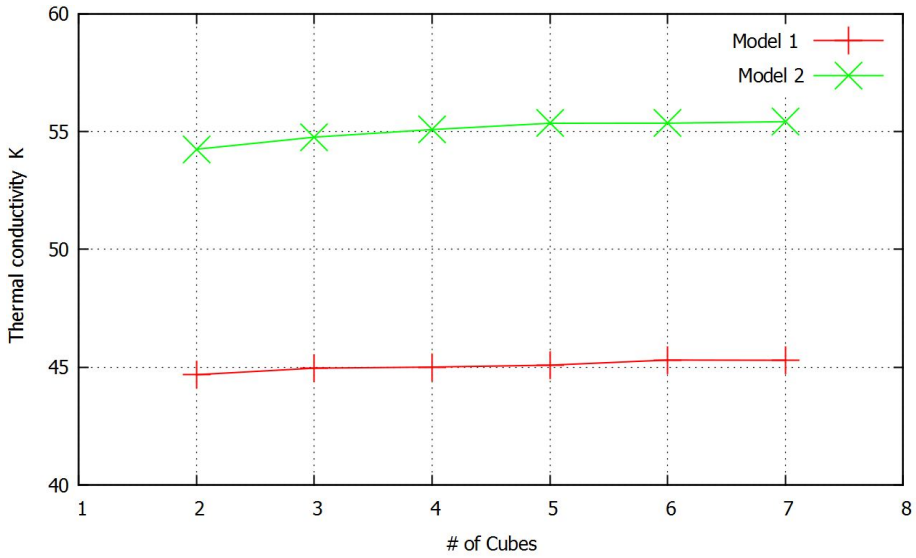


**Figure A.3:** Ansys results for the thermal conductivity of porous cubes as a function of number of cubes in Y direction

varied number of cubes. Based on these results, the values of the thermal conductivity were almost identical for six to seven cubes, so it was estimated that the boundary effects for seven cubes or higher are negligible. Therefore, the results for seven cubes was used as a good assumption for an infinite porous model.

In addition, it was shown that the placements of the holes significantly changed the results. For the face cubic centered structure, the holes were placed in an even distributed such that the porosity at each cross-section of the cube was almost identical. However, for the body centered cubic lattice, there is an uneven distribution of holes which results in a lower thermal conductivity.

Figure A.4 shows the results obtained for the thermal conductivity with varying porosity ratios, comparing the two types of structures. Although the results differ for the different structures, the linear trend is similar for increasing mass fraction.

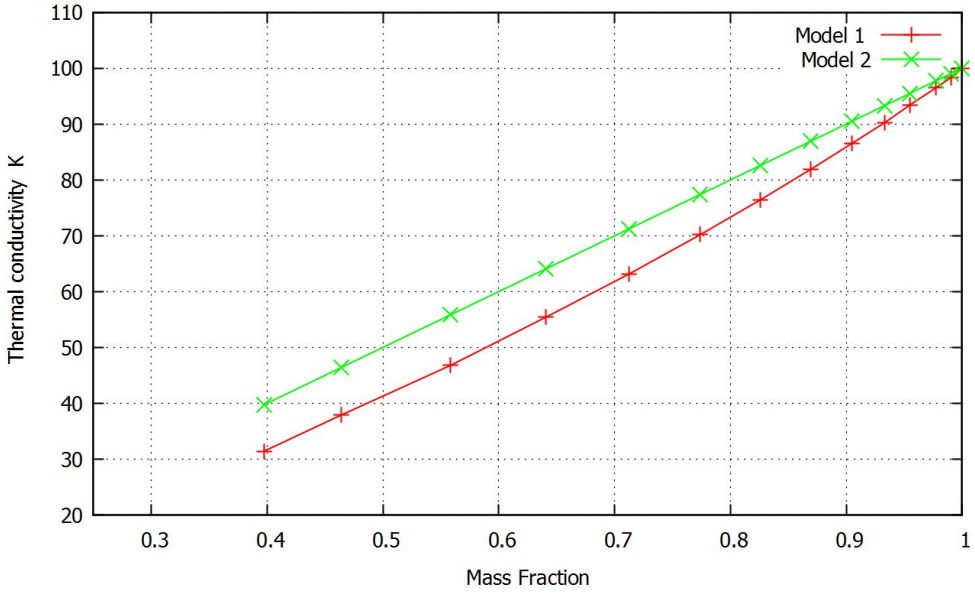


**Figure A.4:** Ansys results for the thermal conductivity of porous cubes as a function of mass fraction